INSTITUTE OF SPACE AND ASTRONAUTICAL SCIENCE
YOSHINODAI,CHUO, SAGAMIHARA, KANAGAWA 252–5210

ISAS RESEARCH NOTE

ISAS RN 861

A Statistical Study of Long-Term X-ray Variabilities of Ultraluminous X-ray Sources and Galactic Black Hole Binaries

Tessei Yoshdia

September 2011

1 : ISAS/JAXA
2 : Department of Physics, Tokyo University of Science

Reproduced from the thesis submitted to
Tokyo University of Science for
the Degree of Doctor of Science (Physics)
January 31, 2011

A Statistical Study of Long-term X-ray Variabilities of Ultraluminous X-ray Sources and Galactic Black Hole Binaries

Tessei Yoshida

Department of Physics, Tokyo University of Science
1-3 Kagurazaka, Shinjuku, Tokyo 162-8601, Japan
yoshida.tessei@ac.jaxa.jp

Abstract

Since 1980's, dozens of variable X-ray point sources with luminosities of $\geq 10^{39-41}$ ergs s^{-1} have been discovered in off-nuclear regions of nearby galaxies. Since their luminosities exceed the Eddington luminosity (canonical upper-limit of the luminosity) of Galactic black holes (BHs) with a typical mass of 10 $M_{\odot}$, they are called "ultraluminous X-ray sources (ULXs)". Two major interpretations have been proposed for the origin of ULXs based on similarities to Galactic BH binaries (BHBs): The first interpretation says that ULXs contain BHs with a mass of 100–1000 $M_{\odot}$ with sub-Eddington luminosities from the standard accretion disk. The second interpretation says that ULXs contain BHs with a mass of <40 $M_{\odot}$ with super-Eddington luminosities from "slim disks", which is considered to appear when an accretion rate is extremely high. Origin of the ULXs is one of the most important astrophysical issues, because evidence of "intermediate-mass BHs" with 100–1000 $M_{\odot}$ is not discovered. However, it is difficult to constrain the origin of ULXs, because relation between the ULX and the Galactic BHB is still unclear primarily due to less sufficient understanding of spectral states of the ULXs in contrast to those of the Galactic BHBs. Obviously, increasing the observational samples of ULXs and conducting systematic studies of their spectral states is a vital step toward understanding the connection between the ULXs and the Galactic BHBs.

Here, we report a statistical X-ray spectral study of 34 energy spectra from seven bright ULXs in the interacting galaxy systems M 51 and NGC 4490/85, using archive data from multiple *Chandra* and *XMM-Newton* observations spanning for a few years. In order to compare with Galactic BHB spectral states, we applied representative spectral models of BHBs; a power-law (PL), a multi-color disk black body (MCD), and a slim disk model to all the ULX spectra. We found a hint of a bimodal structure in the luminosity distribution of the samples, suggesting that ULXs have two states with typical luminosities of $3–6\times10^{39}$ and $1.5–3\times10^{39}$ ergs s^{-1}. Most spectra in the brighter state are explained by the MCD or the slim disk model, whereas those in the fainter state are explained by the PL model. In particular, the slim disk model successfully explains the observed spectral variations of NGC 4490/85 ULX-6 and ULX-8 by changes of the mass accretion rate to BHs of an estimated mass of <40 $M_{\odot}$. From the best-fit model parameters of each state, we speculate that the brighter state in these two ULXs corresponds to the brightest state of Galactic BHBs, which is often called the "apparently standard state". The fainter state of the ULXs has a PL shaped spectrum. In particular, the fainter state of a ULX (M 51 source-82) is similar to the "very high state" of the unique Galactic BHB GRS 1915+105.

ABSTRACT

We conclude that these ULXs can be explained by an interpretation of slightly-massive stellar mass BHs ($<$40 $M_{\odot}$), and their "brighter state" and "fainter state" correspond to the "apparently standard state" and the "very high state" of the Galactic BHBs.

Contents

List of Figures

List of Tables

Chapter 1

Introduction

Astronomy is one of the oldest scientific fields in the long history of mankind, but the X-ray astronomy is a relatively new field, which started about 50 years ago. This is because X-rays cannot reach the ground due to the blocking by the atmosphere. Accordingly, X-ray detectors need to be launched outside of the atmosphere. In the early days, stratospheric balloons and rockets were important tools of the observational X-ray astronomy. The first X-ray satellite *Uhuru* was launched in 1970, and detected ∼400 X-ray sources. At present, several X-ray satellites are operating, such as *RXTE*, *Chandra*, *XMM-Newton*, *Suzaku*, and *MAXI*.

Today, it is known that there are many kinds of X-ray sources in the universe. One of them is Galactic black hole binaries (BHBs) composed of a black hole (BH) and a normal star. Shortly after the birth of the X-ray astronomy, Oda et al. (1971)[119] gave the first observational basis for the BHB Cyg X-1. Afterwards, many BHBs were discovered by several X-ray telescopes, and 40–50 BHBs (including likely candidates) are known so far.

BHBs radiate X-rays from an accretion disk around the BH. The accretion disk is powered by liberating the gravitational energy via mass accretion from the companion star. When an isotropic radiation is assumed, the maximum luminosity of an object with a mass M is calculated as $L_{\rm Edd} = 1.5{\times}10^{38}(M/M_{\odot})$ ergs s^{-1}, which is called the Eddington luminosity. Since the typical mass of Galactic BHs is 10 $M_{\odot}$, the maximum luminosity is about $1.5{\times}10^{39}$ ergs s^{-1}. In fact, most Galactic BHBs do not exceed this limit except for a few cases.

In 1980's, X-ray sources exceeding the BHB luminosity limit ($1.5{\times}10^{39}$ ergs s^{-1}) were

discovered in other galaxies with the *Einstein* satellite (Long & van Speybroeck 1983[85]). These off-nuclear point-like sources detected in the X-ray bandpass with luminosities of $\geq 10^{39-41}$ ergs s^{-1} have been called "Ultraluminous X-ray Sources (ULXs)"; see, e.g., Liu & Bregman (2005)[83], Fabbiano (2006)[39] for a review. Most variable ULXs are considered to be BHBs based on observational characteristics similar to Galactic BHBs, such as short- and long-term variations (e.g., Ptak & Griffiths 1999[133]), thermal disk emission (e.g., Makishima et al. 2000[90]; Feng & Kaaret 2010[43]), and state transitions (e.g., Kubota et al. 2001[75]). The large luminosity of ULXs suggests the BH mass to be much larger than that of Galactic BHs ($\sim$10 $M_\odot$) under the assumption that the radiation is spherically symmetric and the observed luminosity does not exceed the Eddington luminosity.

Three interpretations have been proposed for the origin of ULXs: The first interpretation is that ULXs contain so-called intermediate mass BH with a mass of 100–1000 $M_\odot$ (Miller & Colbert 2004[105]). In fact, an extraordinarily large mass of $\gtrsim$700 $M_\odot$ is suggested for M 82 X-1 based on its large luminosity (Matsumoto et al. 2001[97]; Kaaret et al. 2001[67]). The second interpretation is that ULXs are BHs with a mass comparable to or slightly larger than the stellar mass BHs of $<$40 $M_\odot$ (e.g., Ebisawa et al. 2003[36]; Okajima et al. 2006[121]). In this case, the super-Eddington luminosity is interpreted as a consequence of the ULXs having a *slim disk* (Abramowicz et al. 1988[3]) rather than the standard disk (Shakura & Sunyaev 1973[147]). In the state expressed by the slim disk model, which is a stable solution for very high mass accretion rates of $\gtrsim 8\times10^{18}(M/M_\odot)$ g s^{-1}, the emission is moderately collimated toward the direction normal to the disk so that the luminosity can be super-Eddington (e.g., Ohsuga et al. 2005[120]). The third interpretation is the beaming model with a high collimation (King et al. 2001[73]), although this scenario may have difficulties in explaining extended photoionized nebulae found around several ULXs. For example, Kaaret et al. (2004)[68] studied the Holmberg II ULX within an extended nebula. The nebula emits He II 4686 Å line relatively isotropically, which is considered to be produced by the X-ray photoionization from the central ULX. It is unlikely that the extended nebula be excited by highly collimated radiation.

In order to elucidate the origin of the ULXs, in the present thesis, we focus on similarities of the spectral shapes and the spectral state transitions between Galactic BHBs and ULXs. Galactic BHBs are known to show transition among several states (Esin et al. 1997[38]; Zdziarski & Gierliński 2004[192]). For example, Figure 1.1 shows the two major spectral states: the hard state and the soft state. The former is generally fainter and has a power-law (PL) spectrum in 2–10 keV, while the latter shows a spectrum dominated by thermal

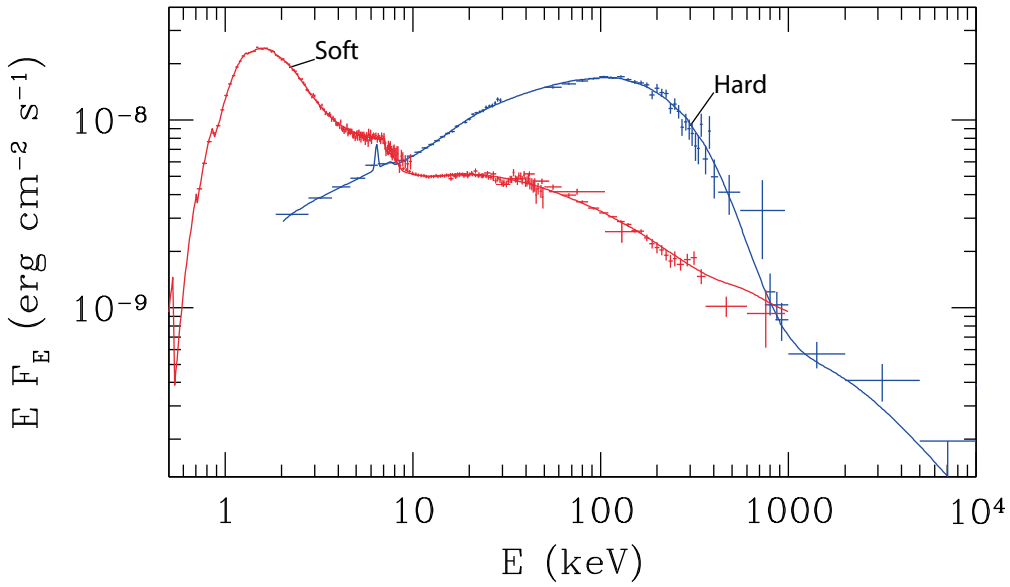

Figure 1.1: Two major spectral states of Cyg X-1 (Gierliński et al. 1999[53]; Done et al. 2007[31]). The indicated spectra of the soft (*red*) state and the hard (*blue*) state are those observed on 1996 and 1991, respectively.

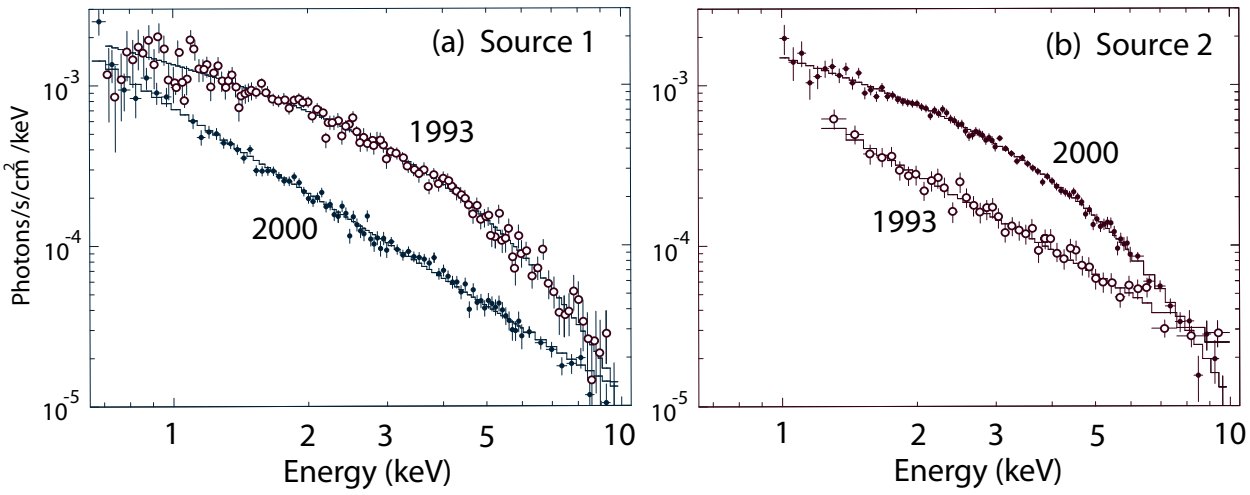

Figure 1.2: Two spectral states of two ULXs: (a) IC 342 source 1 and (b) source 2 (Kubota et al. 2001[75]). The open and filled circles indicate the data taken in 1993 and 2000, respectively. The spectra of the hard state were found in source 1 in 2000 and source 2 in 1993, while those of the soft state were found in source 1 in 1993 and source 2 in 2000.

emission. Similarly to the Galactic BHBs, some ULXs are known to show state transitions in timescales of months to years between two different spectral states. In the case of IC 342 sources 1 and 2, Kubota et al. (2001)[75] dubbed them the "hard" and the "soft" state, which respectively has a spectrum with a PL and a convex shape (Figure 1.2). The latter is brighter than the former by a factor of a few to one order of magnitude. These features look similar between Galactic BHBs and ULXs, but physical mechanism behind the spectral states of ULXs and those of Galactic BHBs is still unclear. This is because ULXs are less frequently monitored than Galactic BHBs, and their time variation is less well understood. Obviously, increasing the samples of ULXs is a key to conduct statistical studies of state transitions, which is the main subject of the present thesis.

This thesis is composed of the following chapters: In Chapter 2, we review basic characteristics of BHs, binary systems containing a BH, theoretical accretion disks, radiation process, and spectral states of Galactic BHBs and ULXs. In Chapter 3, three astronomical facilities used in this thesis are reviewed. In Chapter 4, criteria of the target selection and observation of the selected objects are described. The methods of the data reduction are also given. In Chapter 5, we summarize data analysis and results. In Chapter 6, we develop discussion in three steps. First, we examine the general trend of ULX spectra. Since ULXs causing the state transition are a few in number, we need to confirm the states (hard and soft) from the seven ULXs. Second, we look into the details of individual seven ULXs for determining the states of each ULX and its mass. Finally, we compare the states of the ULXs with those of Galactic BHBs, and investigate the relation between each state. In Chapter 7, we conclude this thesis.

Chapter 2

Review

Contents

2.1 Black Holes

Concept of a BH started from the discovery of the first solution of the Einstein's equation of gravity by Schwarzschild (1916). A BH is a gravitationally collapsed, especially strange object in the framework of the general theory of relativity. Any objects, even photons, cannot escape from its surface. The surface is called the "event horizon", which is at the Schwarzschild radius $R_{\rm g}$ in the case of non-spinning BHs, where $R_{\rm g} = 2M_{\rm BH}G/c^2$. Here, $M_{\rm BH}$, G, and c are the BH mass, the gravitational constant, and the speed of light, respectively. We can rewrite the equation as $R_{\rm g} \sim 2.9(M_{\rm BH}/M_\odot)$ km.

Today, two types of BHs are known, namely stellar mass BHs and super-massive BHs. The former BHs with a typical mass of about 10 $M_\odot$ are often found in galaxies in the Local group. The total number of stellar mass BH candidates is about 50 so far. They are generated from massive stars in the final evolutionary states. The latter BHs with a mass of 10^{6-9} $M_\odot$ are found at the center of many galaxies. The mechanism of generating such massive BHs has not been known yet.

When stars consume nuclear fuels, they collapse into either of three types of compact objects: white dwarfs, neutron stars, and stellar mass BHs. We list the typical mass and radius of these objects in Table 2.1. Since white dwarfs and neutron stars are respectively electron and neutron degenerate objects, they cannot sustain an expected maximum mass, which is $\sim$1.4 $M_\odot$ for white dwarfs (Mazzali et al. 2007[101]) and $\sim$3.2 $M_\odot$ for neutron stars (Rhoades & Ruffini 1974[136]). For the BHs, there is no such mass limit, so all compact objects with a mass larger than 3.2 $M_\odot$ can be regarded as stellar mass BHs.

However, the realistic limit of the BH mass can be considered, because there is a maximum mass for the progenitor star. The limit depends on its metallicity. In the case of our Galaxy with the metallicity $Z/Z_\odot = 1$, the theoretical limit of the BH mass is 15 $M_\odot$ (Belczynski et al. 2010[11]). In fact, the maximum mass among the known stellar mass BHs in our Galaxy is 10–18 $M_\odot$ (GRS 1915+105; McClintock & Remillard 2006[103]). In the case of the IC 10 galaxy in the Local group with a metallicity of $Z/Z_\odot = 0.3$, the limit is calculated as $\sim$30 $M_\odot$ by Belczynski et al. (2010)[11]. In this galaxy, a largest stellar mass BH with a consistent mass of 23–34 $M_\odot$ was found by Prestwich et al. (2007)[130] (IC 10 X-1).

In the extreme case of the very low metallicity $Z/Z_\odot = 0.01$ such as globular clusters, the theoretical limit of the BH mass is expected to be 80 $M_\odot$ by Belczynski et al. (2010)[11]. However, such massive stellar BHs have not been discovered yet.

Table 2.1: Typical mass and radius of compact objects

Object type	Mass ($M_\odot$)	Radius (km)
White dwarf	1	1×10^4
Neutron star	2	10
Stellar mass BH [a]	10	30
Super-massive BH [a]	10^8	3×10^9

[a] The radius is the Schwarzschild radius.

2.2 Binary system containing a BH

As described in § 2.1, photons cannot escape from the surface of a BH, which indicate that we cannot discover a single BH. The only situation, which we can observe a BH, is that the BH and a companion star constitute a binary system. In the system, an accretion disk is formed around the BH, and radiates photons including strong X-rays. The detail of the disk characteristics and the radiation process are explained in § 2.3 and § 2.4, respectively. In this section, we review two distinct groups of binary systems and their mass transfer mechanisms.

2.2.1 LMXB — Low Mass X-ray Binary

A low mass X-ray binary (LMXB) is a close binary system containing a compact object and a low mass companion star ($\lesssim$1 $M_\odot$). The companion star in the LMXB fills the "Roche lobe", which is an equipotentail surface formed by the gravity field of each object. Figure 2.1 shows an example of the gravity potential by both objects. The two gravitational fields have a contract point at the Lagrangian point 1 (L_1). The companion star transfers the materials to the compact object through L_1 (Figure 2.2a). This is called the Roche lobe overflow model.

Most of the known BHBs belong to this group; see Tanaka & Shibazaki (1996)[159], McClintock & Remillard (2006)[103] for a review. All of them are X-ray transient sources (i.e., X-ray novae). An example of the transient light curve of a LMXB is shown in Figure 2.3. They are too faint to observe in the X-ray band for most of the time, but occasionally strong X-ray outbursts are observed. The interval between the outbursts is random from a few

months to tens of years or more.

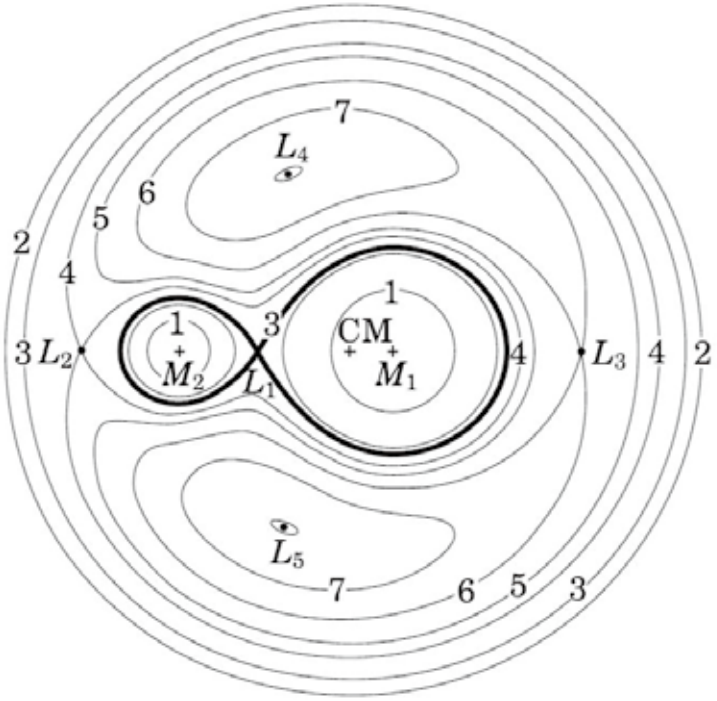

Figure 2.1: Gravitational equipotentail surface formed by two objects (Frank et al. 2002[46]). The thick line shows the Roche lobe. "CM" is the center of mass of the binary system. M_1–M_2 and L_1–L_5 indicate the masses of each object and the Lagrangian points 1–5, respectively. The other numbers show each equipotentail surface. The mass ratio of the two objects is M_1:M_2 = 4:1.

2.2.2 HMXB — High Mass X-ray Binary

A high mass X-ray binary (HMXB) is a close binary system containing a compact object and a high mass companion star (>10 $M_\odot$). The mass transfer mechanism of the HMXB is different from that of the LMXB. Since high mass stars usually blow a strong stellar wind, the materials can be transfered to the compact object without filling the Roche lobe (Figure 2.2b). This is called the wind-fed model.

BHBs belonging this group are only a few (e.g., Cyg X-1, LMC X-1, and X-3; McClintock & Remillard 2006[103]). In contrast to the LMXBs, all of them are X-ray persistent sources (see Figure 2.3 for an example).

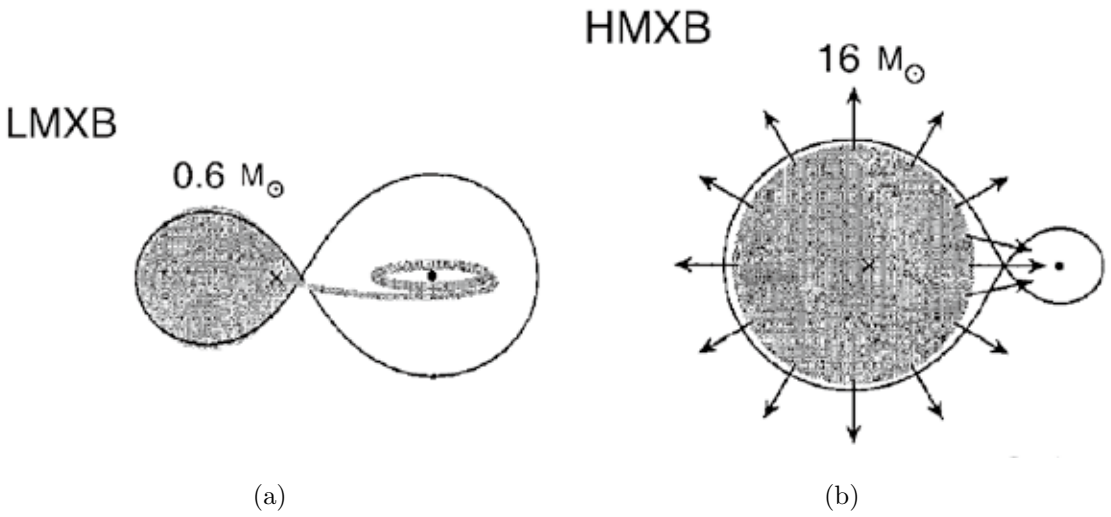

Figure 2.2: Schematic view of (a) LMXB and (b) HMXB (Staubert 2008[155]).

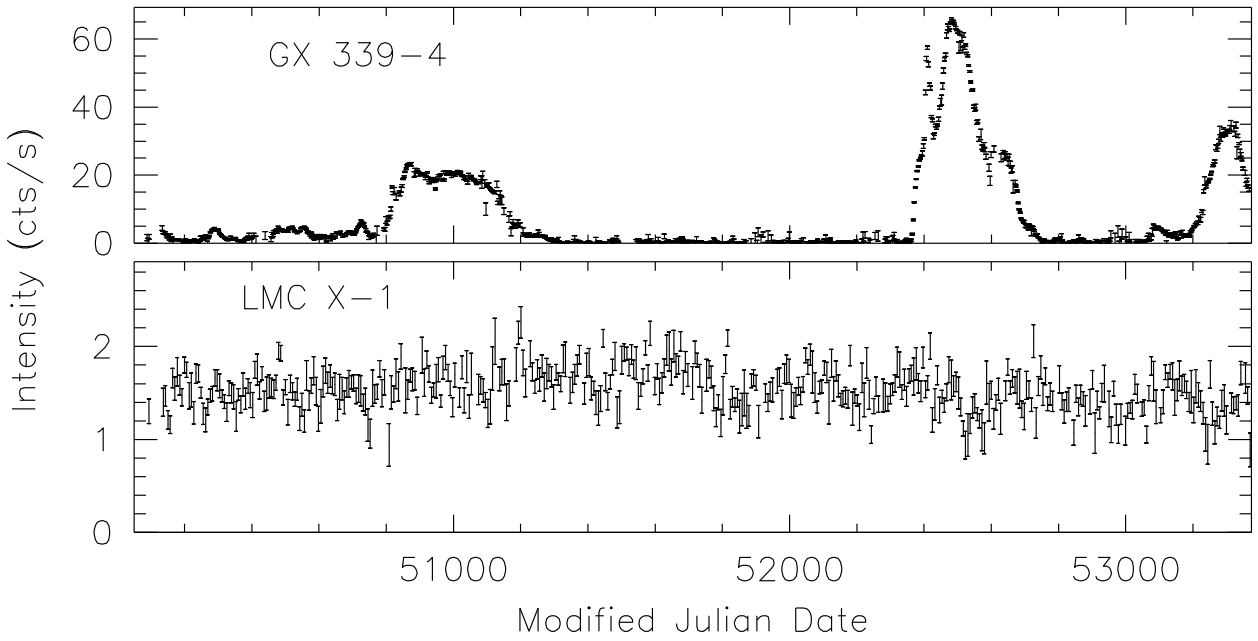

Figure 2.3: Light curves of nine years (from early of 1996 through the end of 2004) in the 1.5–12 keV band by *RXTE*/ASM (The MIT/GSFC ASM Team 2006[165]). The top and bottom panels indicate GX 339−4 as a LMXB and LMC X-1 as a HXMB, respectively.

2.3 Accretion Disk Characteristics of BHBs

BHBs shine by converting the gravitational energy into the radiation, unlike normal stars where the nuclear fusion is the energy source. Here, the *accretion disk* is a key mechanism of the energy conversion (Lynden-Bell 1969[86]). The accretion disk is powered by liberating the gravitational energy via mass accretion. In this section, we briefly explain the formation of the accretion disk and its basic characteristics.

2.3.1 Disk Formation

As described in § 2.2, in close binary systems, materials from a companion star are transfered into a BH. However, the accreting materials with sufficient angular momentum (l) cannot directly head toward the BH due to centrifugal force beyond at the radius $r_{\rm circ} = l^2/GM_{\rm BH}$. Consequently, an accretion disk is formed around the BH. The order of the disk size is the radius of the Sun (10^{8-9} m).

Here, we consider only the matters very close to the plane $z = 0$ in cylindrical coordinate (radius r, azimuth ϕ, height z), namely, a geometrically-thin disk. The angular velocity Ω and the circular velocity v_ϕ of each matter are expressed as the Keplerian value

$$\Omega = \left(\frac{GM_{\rm BH}}{r^3}\right)^{1/2} \tag{2.1}$$

and

$$v_\phi = r\Omega = \left(\frac{GM_{\rm BH}}{r}\right)^{1/2}, \tag{2.2}$$

respectively. By the viscosity in the disk, the angular momentum is transferred from an inner matter rotating at a faster velocity to an outer matter rotating at a slower velocity, so that matters are accreted. The accretion disk is heated up by the thermal energy generated by this viscous process, and begins to radiate photons. The energy efficiency of the process, 5.72% for non-spinning BHs, is much larger than that of the nuclear fusion ($\sim$0.7%).

Two models of the origin of the viscosity are proposed. One is the turbulent viscosity model (Shakura & Sunyaev 1973[147]). The other is the magnetic turbulent viscosity model (Narayan & Yi 1994[116]; Yuan et al. 2003[191]).

2.3.2 Innermost Disk Radius $R_{\rm in}$

In the case of white dwarfs or neutron stars, the innermost edge of the accretion disk may reach the surface of the central objects. The accretion disk of BHBs, however, is truncated at an inner radius, which is called the *innermost disk radius* $R_{\rm in}$. This is because materials cannot steadily rotate around the BH inside the $R_{\rm in}$ due to general relativistic effects. Thus, the orbit with the radius $R_{\rm in}$ is called the innermost stable circular orbit. Since the particle density is almost zero inside the orbit, photons would not be generated from this region.

For non-spinning BHs, the innermost disk radius is expressed as

$$R_{\rm in} = 3R_{\rm g}, \tag{2.3}$$

where $R_{\rm g}$ is the Schwarzschild radius, which is proportional to the BH mass (see § 2.1). Therefore we can estimate the BH mass if $R_{\rm in}$ is measured. Since Makishima et al. (1986)[89], this relation has been utilized to estimate the mass of many BHBs by a lot of authors. We note that this relation is valid only for the standard disk (see the next section in detail).

2.4 Radiation Process of Accretion Disks

At present, several types of theoretical accretion disk models are proposed. Here, we focus on three most widely referred models: the standard disk (Shakura & Sunyaev 1973[147]), the radiatively inefficient accretion flow (RIAF, Yuan et al. 2003[191]), and the slim disk (Abramowicz et al. 1988[3]). In this sections, we first introduce common properties among the three models. We then explain some more details of two models (standard disk and slim disk), which are used in this thesis.

2.4.1 Common Properties of Accretion Disk Models

Characteristics of an accretion disk is mainly determined by the energy balance, which consists of three factors: viscous heating ($Q^{+}_{\rm vis}$), radiative cooling ($Q^{-}_{\rm rad}$), and advective cooling ($Q^{-}_{\rm adv}$). The advective cooling is caused by an advection process, in which the internal (or radiation) energy is inhaled into a BH.

In the early 1970's, by considering $Q^{+}_{\rm vis}$ and $Q^{-}_{\rm rad}$, Shakura & Sunyaev (1973)[147] proposed the fundamental model for an accretion disk for a geometrically-thin ($H/r \ll 1$) and

optically-thick ($\tau \gg 1$) condition, where H and τ are the disk height and the optical depth, respectively. Here, τ is defined as

$$\tau = \kappa\rho H = \frac{\kappa\Sigma}{2}, \tag{2.4}$$

where κ, ρ, and Σ are the opacity, the density, and the surface column density of the disk, respectively. This geometrical thickness indicates that the internal (thermal) energy of the disk is smaller than the gravitational energy. This optical thickness indicates that the disk is a blackbody radiator. The Shakura-Sunyaev model assumes that the viscosity is simply proportional to the gas pressure; i.e.,

$$t_{r\phi} = -\alpha P, \tag{2.5}$$

where $t_{r\phi}$, α, and P indicate the viscous force per unit area (i.e., the shear stress tensor), the viscous parameter (the realistic range of 0–1), and the pressure (including gas and radiation), respectively. Although this model includes many other assumptions (§ 2.4.2), it is referred to as the *standard disk* model, because the model is very simple and can explain the soft component of the observed X-ray energy spectra of Galactic BHBs (see § 2.5.2).

Since accretion disks are powered by liberating the gravitational energy of accretion matters, the *mass accretion rate* ($\dot{M} \equiv dM/dt$) is the most important parameter. When the rate is very low or very high, it is known that the standard disk cannot reproduce observed spectra. For such situations, it is necessary to consider the advective cooling $Q^{-}_{\rm adv}$ to calculate correct disk models. Disk models with a predominant advective cooling effect ($Q^{+}_{\rm vis} = Q^{-}_{\rm adv} \gg Q^{-}_{\rm rad}$) is called the "advection dominant accretion flow" model (ADAF, Ichimaru 1977[65]; Narayan & Yi 1994[116]). The RIAF and the slim disk models are optically-thin and -thick solutions of the ADAF models, respectively.

For the case of the very low rate of accretion, Yuan et al. (2003)[191] proposed the RIAF model with a geometrically-thick and optically-thin condition. This model has been successful to reproduce observed X-ray spectra of Galactic BHBs in the faint state. In this situation, the surface density is low, making the radiation inefficiently produced ($Q^{+}_{\rm vis} \gg Q^{-}_{\rm rad}$). As a result, the disk becomes hot (due to the low radiation cooling) and geometrically-thick (due to the high gas pressure). Finally, most of the energy are inhaled into the BH (advective cooling).

In the case of a very high mass accretion rate, the slim disk model (geometrically-thick and optically-thick) was proposed by Abramowicz et al. (1988)[3]. This model can reproduce

spectra of Galactic BHBs in the brightest state and those of several ULXs. Unlike the RIAF, the surface column density of the slim disk is very high. In this situation, the photon diffusion velocity ($=c/\tau$) becomes unlimitedly small due to a frequent interaction between matter and photons. Thus, photons are trapped in the flow inside a certain radius (the photon trapping radius, Figure 2.4). In other words, almost all photons generated in the disk are inhaled into a BH before they reach the disk surface. This is called the photon trapping process (Katz 1977[70]; Begelman & Meier 1982[10]), which is one of the advective cooling mechanisms. Since many photons are within the disk, the radiation pressure becomes very high. As a result, the disk becomes geometrically-thick. In the radiation pressure dominated disk, the advective cooling satisfies the relation (Abramowicz et al. 1986[2]),

$$Q^{-}_{\rm adv} \gtrsim \left(\frac{H}{r}\right)^2 Q^{+}_{\rm vis}. \tag{2.6}$$

Therefore the slim disk model loses the large energy by the advection (but a lot of high energy photons are also emitted).

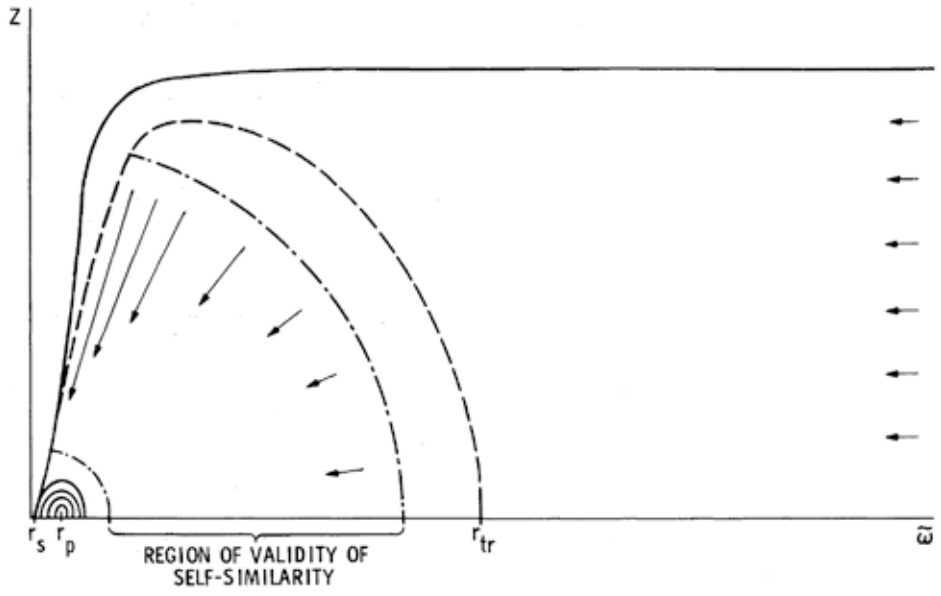

Figure 2.4: Schematic view of the photon trapping by the slim disk (Begelman & Meier 1982[10]). The Schwarzschild radius and the photon trapping radius are expressed as $r_{\rm s}$ and $r_{\rm tr}$, respectively. The solid and dashed lines indicate the disk surface and the photon trapping surface, respectively. The arrows show inflow of the disk matters.

Abramowicz et al. (1995)[4] found that a global view of the whole equilibrium sequences of the above three models (Figure 2.5). Positive slopes ($d\log \dot{M}/d\log \Sigma > 0$) indicate stable solutions. The right S-shaped curve includes the two optically-thick stable solutions: the optically-thick ADAF solution (the upper slope of the S-shape) and the standard disk solution (the lower slope). The left curve shows the optically-thin ADAF solution.

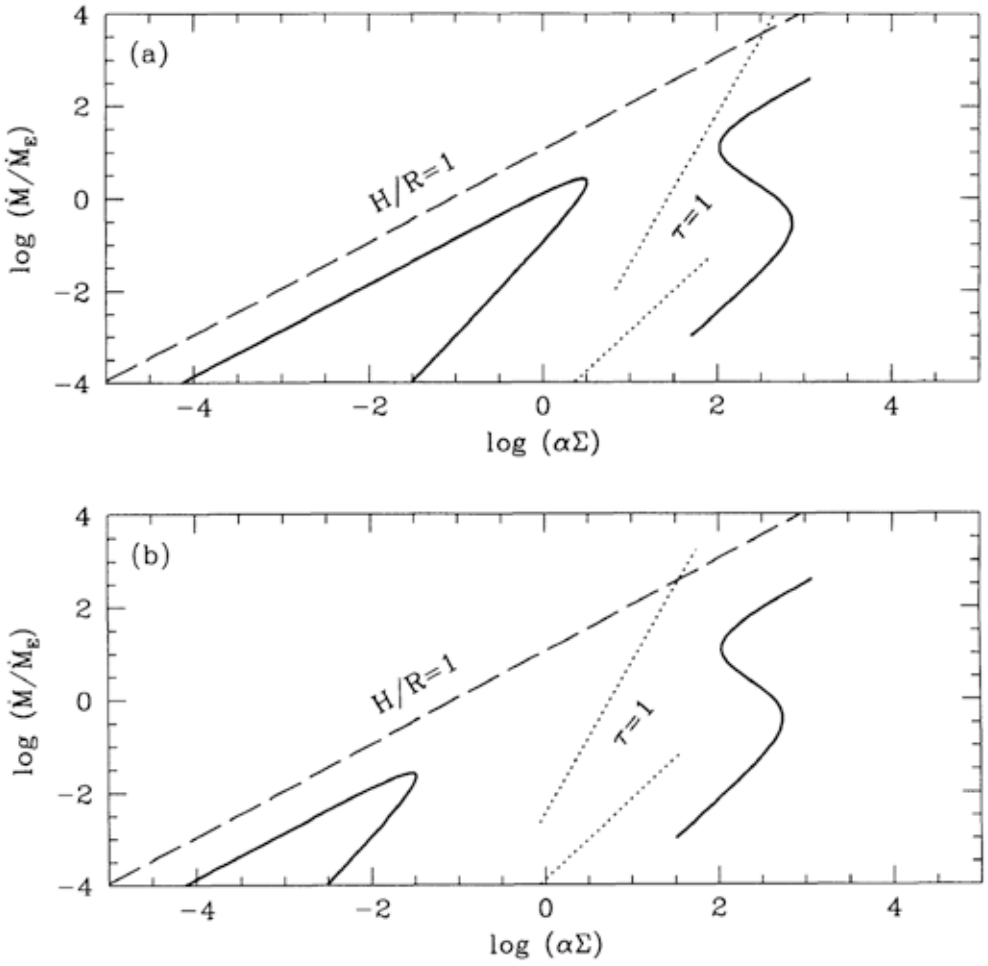

Figure 2.5: Thermal equilibria for accretion disks (Abramowicz et al. 1995[4]). The left and right (S-shaped) solid curves indicate the optically-thin and -thick disk solutions, respectively. The upper or lower dotted line shows $\tau = 1$ calculated by assuming that the radiation or gas pressure is dominant. The right side of the dotted lines is optically-thick, and the left side is the inverse. The mass and the radius are 10 $M_\odot$ and 5 $R_{\rm g}$, respectively. The viscous parameter is (a) $\alpha = 0.1$ or (b) $\alpha = 0.01$.

Finally, we summarize the basic properties of each model in Table 2.2. We show rough mass accretion rates by using the Eddington mass accretion rate $\dot{M}_{\rm Edd}$, which is defined as $\dot{M}_{\rm Edd} = L_{\rm Edd}/\eta c^2$, where η is the energy efficiency. When matters accrete with $\dot{M}_{\rm Edd}$, its luminosity would reach the Eddington luminosity.

Table 2.2: Basic properties of accretion disk models

Properties	Model name		
	Standard disk	RIAF	Slim disk
Mass accretion rate	$<\dot{M}_{\rm Edd}$	$\ll\dot{M}_{\rm Edd}$	$>\dot{M}_{\rm Edd}$
Luminosity	$L \propto \dot{M}$	$L \propto \dot{M}^2$	$L \propto \ln(\dot{M})$
Geometrical thickness	thin ($H/r \ll 1$)	thick ($H/r \lesssim 1$)	thick ($H/r \lesssim 1$)
Optical thickness	thick ($\tau \gg 1$)	thin ($\tau < 1$)	thick ($\tau \gg 1$)
Energy balance	$Q^+_{\rm vis} = Q^-_{\rm rad} \gg Q^-_{\rm adv}$	$Q^+_{\rm vis} = Q^-_{\rm adv} \gg Q^-_{\rm rad}$	$Q^+_{\rm vis} = Q^-_{\rm adv} \gg Q^-_{\rm rad}$
Spectral shape (2–10 keV)	convex	PL	convex

2.4.2 Standard Disk

Assumptions

The standard disk model has several assumptions, so that the disk structure is analytically solved.

(i) The central BH has a majority of the total mass of the system, thus the mass of the disk can be ignored.

(ii) The disk is steady ($\dot{M}$ = Const.).

(iii) The disk is axisymmetric.

(iv) The disk is geometrically-thin ($H/r \ll 1$).

(v) The circular velocity v_ϕ of matter is large enough compared to the drift velocity v_r in the radial direction; $v_\phi \gg v_r$.

(vi) The hydrostatic balance holds in the vertical direction.

(vii) The disk is optically-thick ($\tau = \kappa\rho H \gg 1$).

(viii) Viscosity is proportional to the gas pressure ($t_{r\phi} = -\alpha P$).

Under these assumptions, we can obtain analytical solutions of the radial profile of all the physical quantities (v_r, v_ϕ, H, ρ, P, effective temperature of the disk surface $T_{\rm eff}$, etc.) by using the following eight equations: mass conservation, momentum conservation, angular-momentum conservation, hydrostatic balance, energy balance, equation of state, opacity, and viscosity prescriptions. In the following, we focus on the radial profile of the effective temperature, which determines the observed accretion disk spectra. Refer to Fukue et al. (2008)[49] for the details of other physical quantities.

Radial Profile of the Effective Temperature $T_{\rm eff}$

Radial profile of the effective temperature of the disk surface can be obtained from the relation of the energy balance between the viscous heating and the radiative cooling ($Q^+_{\rm vis} = Q^-_{\rm rad}$). For the viscous heating, by using the definition of the shear stress tensor ($t_{r\phi} = \rho\nu r\, d\Omega/dr$), we can derive the viscous dissipative function (Lynden-Bell & Pringle 1974 [87]),

$$\Phi = t_{r\phi}\left(\frac{\partial v_\phi}{\partial r} - \frac{v_\phi}{r}\right) = \rho\nu\left(r\frac{d\Omega}{dr}\right)^2, \tag{2.7}$$

where ν is the kinematic viscosity. Therefore the vertically integrated heating rate per unit surface area is

$$Q^+_{\rm vis} = \int_{-\infty}^{+\infty}\Phi\, dz = \int_{-\infty}^{+\infty}\rho\nu\left(r\frac{d\Omega}{dr}\right)^2 dz = \frac{9}{4}\nu\Sigma\Omega^2 = -\frac{3}{2}t_{r\phi}(2H)\Omega. \tag{2.8}$$

We also consider the angular-momentum conservation. When $\dot{M}$ is constant, the conservation is written as

$$\dot{M}l + 2\pi r \times r t_{r\phi} \times 2H = J\ (=\text{Const.}), \tag{2.9}$$

where l ($=r^2\Omega$) is the angular momentum per unit mass. Since the particle density is almost zero inside $R_{\rm in}$ (§ 2.3.2), we can set the boundary condition $t_{r\phi} = 0$ at $r = R_{\rm in}$, so that the equation (2.9) becomes

$$\dot{M}{R_{\rm in}}^2\Omega = J. \tag{2.10}$$

Using the equations (2.9) and (2.10), the shear stress tensor $t_{r\phi}$ is expressed as

$$t_{r\phi} = -\frac{\Omega\dot{M}}{4\pi H}\left(1 - \sqrt{\frac{R_{\rm in}}{r}}\right). \tag{2.11}$$

When Ω and $t_{r\phi}$ are substituted using the equations (2.1) and (2.11), we finally obtain the following expression of the vertically integrated heating rate per unit surface,

$$Q^{+}_{\rm vis} = \frac{3GM_{\rm BH}\dot{M}}{4\pi r^3}\left(1-\sqrt{\frac{R_{\rm in}}{r}}\right). \tag{2.12}$$

Since the disk is optically-thick, the disk surface emits a blackbody spectrum with $T_{\rm eff}$. According to the Stefan-Boltzmann law, the total flux (ergs cm^{-2} s^{-1} in unit) emitted by the blackbody is proportional to ${T_{\rm eff}}^4$. Consequently, the radiative cooling rate per unit surface of the disk is

$$Q^{-}_{\rm rad} = 2\sigma {T_{\rm eff}}^4, \tag{2.13}$$

where σ is the Stefan-Boltzmann constant, and the factor 2 represents the two sides of the disk.

Finally, from the relation of the energy balance of the standard disk ($Q^{+}_{\rm vis} = Q^{-}_{\rm rad}$), the equations (2.12) and (2.13), we find the radial profile of the effective temperature,

$$T_{\rm eff}(r) = \left[\frac{3GM_{\rm BH}\dot{M}}{8\pi\sigma r^3}\left(1-\sqrt{\frac{R_{\rm in}}{r}}\right)\right]^{1/4}. \tag{2.14}$$

We illustrated the equation (2.14) for the case of a non-spinning BH with 10 $M_\odot$ and 0.1 $\dot{M}_{\rm Edd}$ in Figure 2.6. The maximum temperature ($T^{\rm max}_{\rm eff}$) at $r = (7/6)^2 R_{\rm in}$ is

$$T^{\rm max}_{\rm eff} = \left(\frac{3GM_{\rm BH}\dot{M}}{8\pi\sigma R^3_{\rm in}}\right)^{1/4} \cdot 6^{3/2} \cdot 7^{-7/4}. \tag{2.15}$$

In the case of Figure 2.6, the value is calculated as $T^{\rm max}_{\rm eff} = 1.18 \times 10^7$ K, so that the hottest part of the disk radiates a blackbody spectrum with about 1 keV (soft X-ray), which basically agrees with observations.

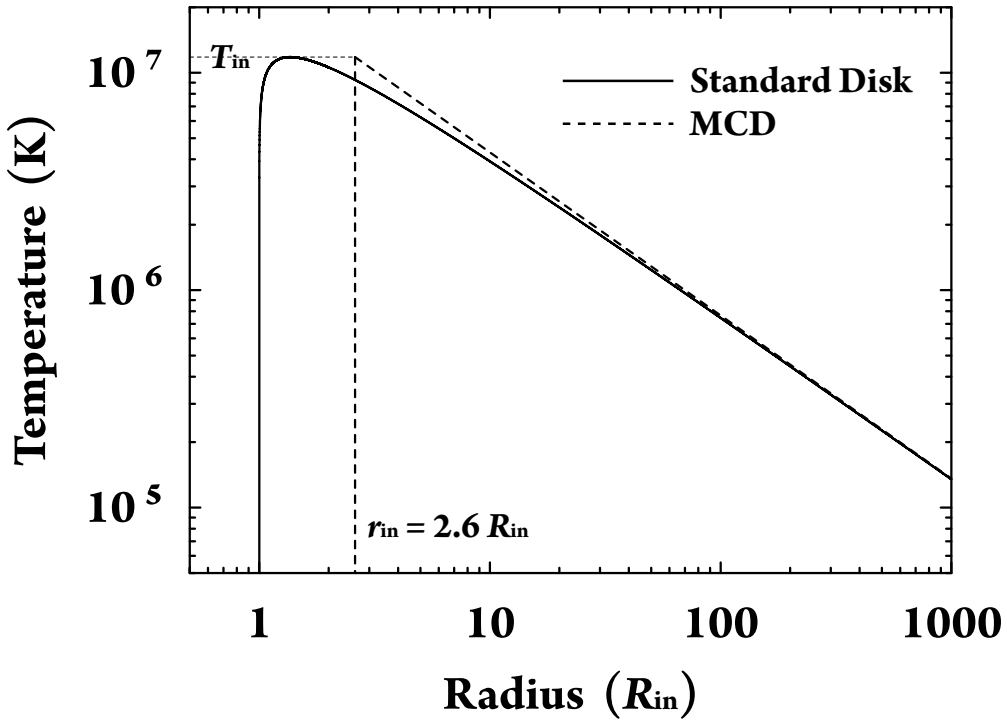

Figure 2.6: Radial profiles of the effective temperature of the standard disk (*solid*, equation 2.14) and the MCD model (*dashed*, equation 2.16). The parameters are $M_{\rm BH} = 10\ M_\odot$ and $0.1\ \dot{M}_{\rm Edd}$ for a non-spinning BH.

Disk Spectrum

As shown in Figure 2.6 and the equation (2.14), the temperature varies with the disk radius. Thus, the integrated spectrum and luminosity are a superposition of many blackbody radiation of different temperatures up to $T_{\rm eff}^{\rm max}$. We introduce a simple mathematical approximation model of the standard disk for spectral analysis, so-called the multi-color disk blackbody (MCD) model (Pringle 1981[131]; Mitsuda et al. 1984[107]).

The MCD model ignores the innermost region ($r \sim R_{\rm in}$), in other words, we do not consider a term $(1-\sqrt{R_{\rm in}/r})$ of the equation (2.14). It should be treated for a strict analysis, but this approximation is known to give reasonable results. Without the innermost region, the equation (2.14) is approximated as

$$T_{\rm eff}^{\rm MCD}(r) = \left[\frac{3GM_{\rm BH}\dot{M}}{8\pi\sigma r^3}\right]^{1/4} = T_{\rm in,eff}\left(\frac{r}{r_{\rm in}}\right)^{-3/4}, \tag{2.16}$$

where $T_{\rm in,eff} \equiv T_{\rm eff}^{\rm max}$ and $r_{\rm in} \equiv (7/6)^2 \cdot 7^{1/3}\ R_{\rm in} \sim 2.6\ R_{\rm in}$, which are called the innermost disk temperature and the apparent inner radius, respectively (Figure 2.6).

In general, when the radial profile of the surface effective temperature is expressed as $T_{\rm eff} \propto r^{-p}$, the observed flux S_ν of the disk is written as

$$S_\nu \ \propto \ \nu^{3-(2/p)}, \tag{2.17}$$

where ν is the frequency. Since the value p of the MCD model is 3/4, the spectrum becomes $S_\nu \propto \nu^{1/3}$ (see Fukue et al. 2008[49] in detail). An example of MCD spectra is shown in Figure 2.7. The middle part of the spectrum is proportional to $\nu^{1/3}$ with the Wien cut-off at the high frequency end and the Rayleigh-Jeans tail in the low frequency end.

Disk Luminosity

Using the temperature distribution of the standard disk (equation 2.14), the total integrated bolometric luminosity is easily calculated as

$$L_{\rm disk} = \int_{R_{\rm in}}^{R_{\rm out}} Q_{\rm rad}^{-} 2\pi r\, dr = \int_{R_{\rm in}}^{R_{\rm out}} \frac{3GM_{\rm BH}\dot{M}}{2r^2}\left(1-\sqrt{\frac{R_{\rm in}}{r}}\right) dr = \frac{1}{2}\frac{GM_{\rm BH}\dot{M}}{{R_{\rm in}}^2}, \tag{2.18}$$

where $R_{\rm out}$ is a radius at the outer edge of the disk, which is assumed as $R_{\rm out} \gg R_{\rm in}$. This luminosity is equal to a half of the total liberated gravitational energy from the infinity to the innermost disk radius.

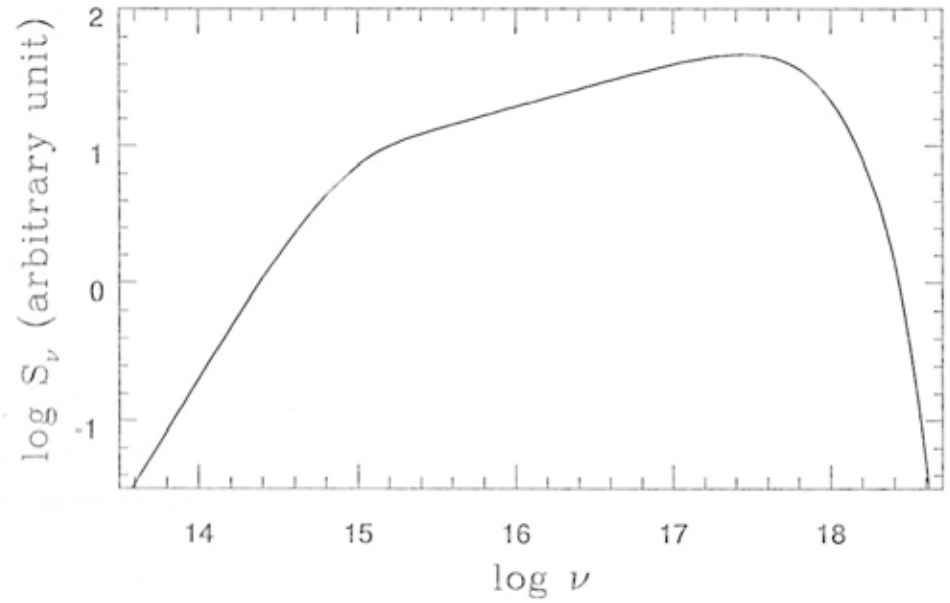

Figure 2.7: Multi-color blackbody spectrum (in an arbitrary unit) of the standard disk for a non-spinning BH with $M_{\rm BH} = 10\ M_\odot$ and $\dot{M} = 10^{18}$ g s^{-1} (Fukue et al. 2008[49]).

On the other hand, under the MCD formalism (equation 2.16), the disk luminosity is given by

$$L_{\rm disk}^{\rm MCD} = \int_{r_{\rm in}}^{R_{\rm out}} Q_{\rm rad}^{-} 2\pi r\, dr = \int_{r_{\rm in}}^{R_{\rm out}} \frac{4\pi {r_{\rm in}}^3 \sigma {T_{\rm in,eff}}^4}{r^2}\, dr = 4\pi {r_{\rm in}}^2 \sigma {T_{\rm in,eff}}^4. \tag{2.19}$$

If the MCD luminosity is equal to the expected disk bolometric luminosity of $\frac{1}{2}\frac{GM_{\rm BH}\dot{M}}{{R_{\rm in}}^2}$, we obtain

$$R_{\rm in} = \left(\frac{3}{7}\right)^{1/2} \left(\frac{6}{7}\right)^{3} r_{\rm in} \ \sim\ 0.412\, r_{\rm in}. \tag{2.20}$$

Here, we used the relation $T_{\rm in,eff} \equiv T_{\rm eff}^{\rm max}$ and the equation (2.15). Kubota et al. (1998)[74] defined this value as $\xi = 0.412$, which is called the correction factor for the inner boundary condition.

When we estimate the disk temperature, we always need to take into account that a measured *color* temperature $T_{\rm col}$ is higher than an effective temperature $T_{\rm eff}$ due to effects of the electron scattering in the disk vertical direction. The ratio (so-called the spectral hardening factor) is defined as $\kappa = T_{\rm col}/T_{\rm eff}$, which is always larger than 1. For BHBs with

the luminosity of 0.1 $L_{\rm Edd}$, Shimura & Takahara (1995)[148] found that the spectrum from the inner region can be approximated by a diluted blackbody with $\kappa \sim 1.7$. We need to correct the measured temperature by assuming this value. Considering this effect and the correction factor for the inner boundary condition ξ, the true inner radius $R_{\rm in}$ can be calculated as

$$R_{\rm in} = \kappa^2 \cdot \xi \cdot r_{\rm in}. \tag{2.21}$$

Finally, using ξ and κ, we can rewrite $L_{\rm disk}^{\rm MCD} = 4\pi {r_{\rm in}}^2 \sigma {T_{\rm in,eff}}^4$ to

$$L_{\rm bol} \equiv L_{\rm disk}^{\rm MCD} = 4\pi \left(\frac{R_{\rm in}}{\xi}\right)^2 \sigma \left(\frac{T_{\rm in,col}}{\kappa}\right)^4, \tag{2.22}$$

where $L_{\rm bol}$ is the disk bolometric luminosity. Since $R_{\rm in}$ is constant, the luminosity is proportional to only the innermost disk temperature to the power of four.

2.4.3 Slim Disk

As explained in § 2.4.1, the slim disk model is considered for the situation with a high mass accretion rate. Since the advective cooling by the photon trapping is significantly larger than the radiative cooling ($Q_{\rm adv}^- \gg Q_{\rm rad}^-$), the disk properties are different from those of the standard disk. In this subsection, in order to compare with the standard disk, we mention only the height profile, temperature profile, spectrum, and luminosity of the slim disk.

Watarai & Fukue (1999)[183] investigated the slim disk properties by using the method of self-similar solutions of Narayan & Yi (1994)[116]. In this method, the energy balance is defined as

$$Q_{\rm adv}^- = Q_{\rm vis}^+ - Q_{\rm rad}^- = f Q_{\rm vis}^+, \tag{2.23}$$

where f is the advection parameter, which is defined as $Q_{\rm rad}^- = (1-f)Q_{\rm vis}^+$. When the mass accretion rate increases, the value of f becomes large.

From some self-similar solutions, Watarai & Fukue (1999)[183] obtained the height profile

$$H(r) = \sqrt{c_3} r, \tag{2.24}$$

and the temperature profile

$$T_{\rm eff}(r) = \left[\frac{3\sqrt{c_3} L_{\rm Edd}}{16\pi}\right]^{1/4} r^{-1/2}. \tag{2.25}$$

Here, $\sqrt{c_3}$ is a parameter of the order of unity, and depends on three parameters: the viscous parameter α, ratio of specific heats γ, and advection parameter f (Figure 2.8). We note that the temperature profile of the slim disk is proportional to $r^{-1/2}$, although that of the standard disk is $r^{-3/4}$. The two profiles with different mass accretion rates are shown in Figures 2.9 and 2.10. Here, we define $\dot{m} \equiv \dot{M}/\dot{M_{\rm Edd}} = \dot{M}c^2/L_{\rm Edd}$. As the accretion rate increases, the disk becomes geometrically-thick (Figure 2.9), and advection-dominated parts ($T_{\rm eff} \propto r^{-1/2}$) expand from the innermost region (beyond $R_{\rm in}$, Figure 2.10).

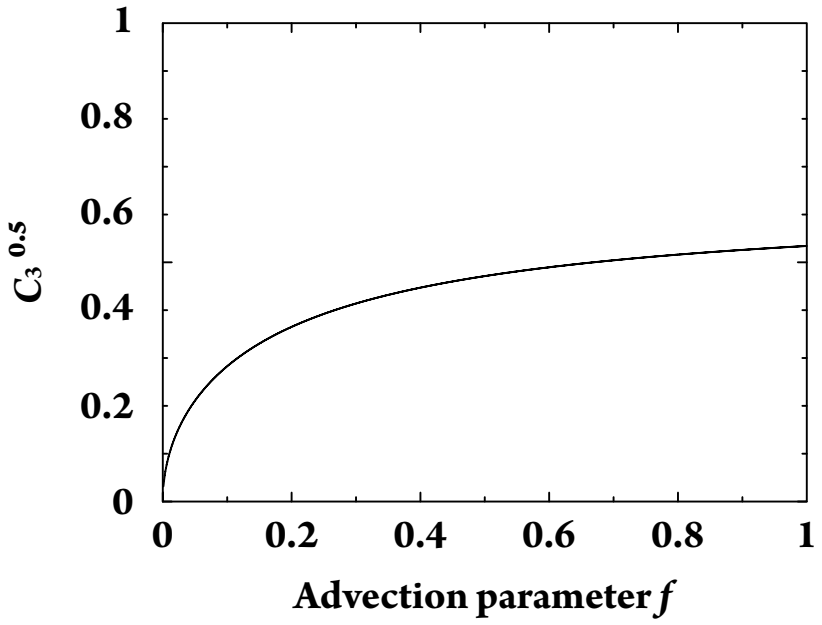

Figure 2.8: Parameter dependence of $\sqrt{c_3}$. The viscous parameter $\alpha = 0.1$ and the ratio of specific heats $\gamma = 4/3$ are fixed.

In the case of $T_{\rm eff}(r) \propto r^{-p}$ with $p = 1/2$, we obtain the disk spectrum $S_\nu \propto \nu^{-1}$ by using the relation $S_\nu \propto \nu^{3-(2/p)}$ (equation 2.17). The spectral energy distribution ($\nu S_\nu \propto \nu^0$) is shown in Figure 2.11. When the mass accretion rate is low, the spectrum is relatively steep. On the other hand, when the rate is high, the spectrum becomes flatter from the higher energy part due to the innermost region with a flatter temperature profile ($\propto r^{-1/2}$, see Figure 2.10).

From the temperature profile (equation 2.27), Watarai & Fukue (1999)[183] found the slim disk luminosity of

$$L_{\rm disk} \sim \frac{3}{4}\sqrt{c_3} L_{\rm Edd} \ln\left(\frac{R_{\rm out}}{r'_{\rm in}}\right), \tag{2.26}$$

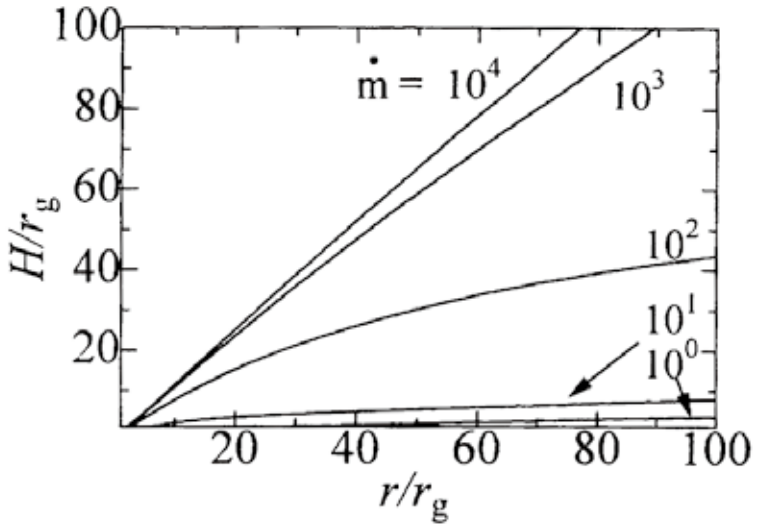

Figure 2.9: Disk height profile with different mass accretion rate: $\dot{m} = 10^0$, 10^1, 10^2, 10^3, and 10^4 from bottom to top (Watarai et al. 2000[184]). r_g indicates the Schwarzschild radius R_g for this figure. The BH mass is fixed as 10 $M_\odot$.

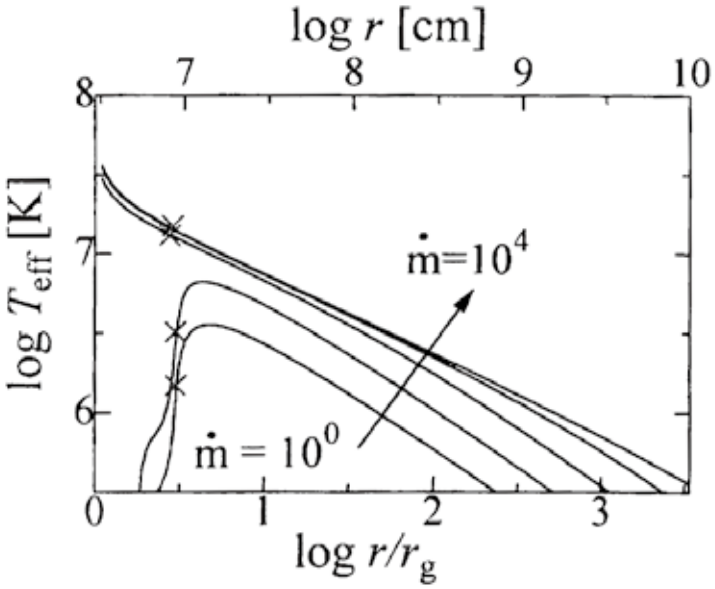

Figure 2.10: Same as Figure 2.9, but for the disk temperature profile (Watarai et al. 2000[184]). The crosses represent the sonic points.

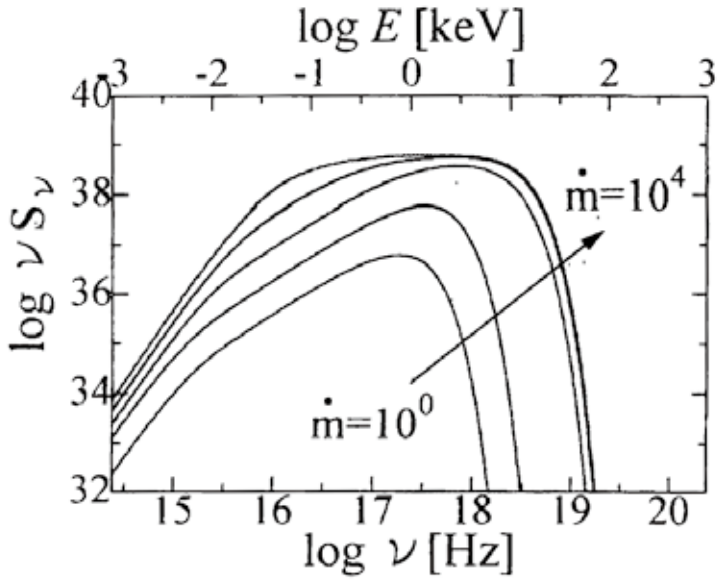

Figure 2.11: Spectral energy distribution of the slim disk for a non-spinning BH with $M_{\rm BH} = 10\ M_\odot$ and different mass accretion rate (same as Figure 2.9).

where $r'_{\rm in}$ is the innermost radius of the slim disk ($<R_{\rm in}$). $R_{\rm out}$ is the boundary radius between the inner slim disk region and the outer standard disk region, and is roughly proportional to $2\dot{m}R_{\rm g}$. In other words, the luminosity of the slim disk is proportional to $\ln \dot{m}$ (while $L_{\rm disk} \propto \dot{m}$ for the standard disk). Mineshige et al. (2000)[117] calculated the disk luminosity variation as a function of $\dot{m}$ considering both disks, and derived the following relation,

$$L(\dot{m})/L_{\rm Edd} \sim \left\{ \begin{array}{ll} 2\,[1+\ln{(\dot{m}/50)}] & \text{for } \dot{m} \geq 50 \\ \dot{m}/25 & \text{for } \dot{m} < 50 \end{array} \right\}, \tag{2.27}$$

which is shown in Figure 2.12. This result indicates two possibilities: (i) At least, in a very high accretion rate $\dot{m} \sim 50$ or more, the slim disk feature ($L_{\rm disk} \propto \ln \dot{m}$) appears significantly. This accretion rate corresponds to $\gtrsim 8\times10^{18}(M/M_\odot)$ g s^{-1}. (ii) The luminosity hardly changes even if the accretion rate is remarkably high ($\dot{m} = 10^{2-4}$) with a luminosity approaching to $\sim$10 $L_{\rm Edd}$.

Since many photons close in the gas of the slim disk (§ 2.4.1), the gas inside $R_{\rm in}$ can radiate before it is inhaled into a BH. Thus, the "apparent" inner radius $r_{\rm in}$ seems to change (Figure 2.10). Watarai et al. (2000)[184] examined the relation between $r_{\rm in}$ and $T_{\rm in}$ by fitting the MCD model to simulated slim disk spectra. As a result, they obtained the simple relation

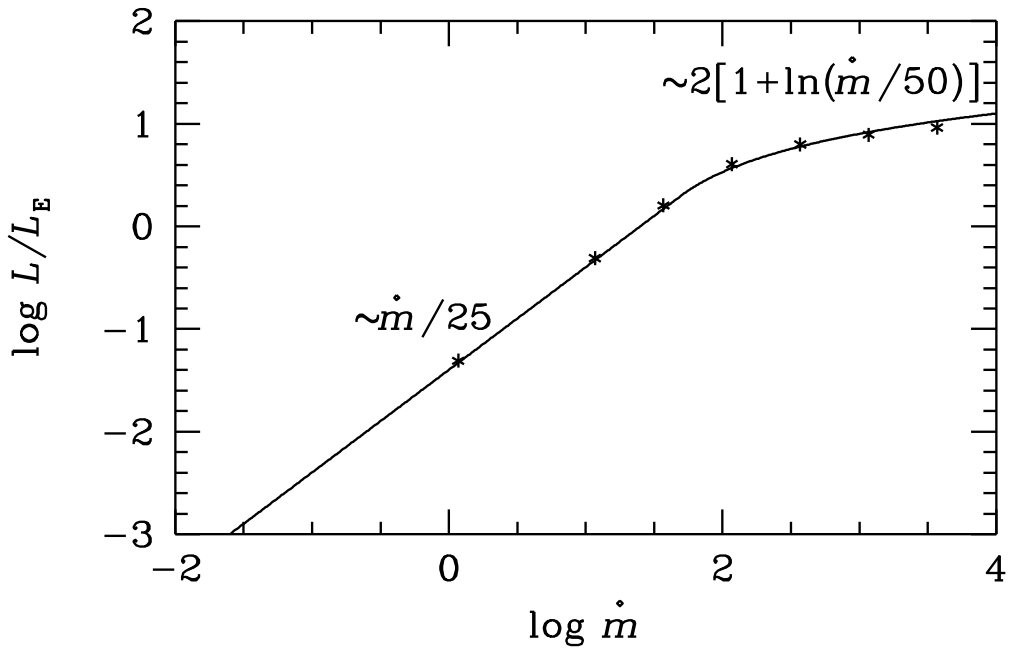

Figure 2.12: Disk luminosity as a function of $\dot{m}$ (Mineshige et al. 2000[117]). The calculated luminosities and the fitting formula (equation 2.27) are shown as the asterisks and the solid line.

$r_{\rm in} \propto {T_{\rm in}}^{-1}$, i.e.,

$$L_{\rm bol} \propto {T_{\rm in}}^2, \tag{2.28}$$

by using the equation (2.19) — $L \propto {r_{\rm in}}^2 \cdot {T_{\rm in}}^4$.

2.5 Spectral States of Galactic BHBs

In this section, we review the spectral states of Galactic BHBs. First of all, we introduce the brief history of the discovery of the states, and then explain each state in details in following subsections.

Existence of different spectral states in BHBs was already noticed in the early 1970's (e.g., Tananbaum et al. 1972[160] for Cyg X-1; Markert et al. 1973[92] for GX 339−4). Conventionally, it is believed that there are at least three distinct states: the quiescent state, the low-hard state (LHS), and the high-soft state (HSS). LMXBs spend most of their life time in the quiescent state, which is the faintest state at a very low luminosity below $\sim 10^{33}$ ergs s^{-1}. The flux level of BHBs in this state is too faint to observe by contemporary all-sky X-ray monitors. The remaining two states are brighter than the quiescent state.

In 1990's, a new state was observed in a few BHBs by the *Ginga* satellite (e.g., Miyamoto et al. 1991[108] for GX 339−4; Miyamoto et al. 1993[109] for GRS 1124−68). This state is brighter than the aforementioned three states, and is thus called the very high state (VHS). After the advent of the all-sky X-ray monitor *RXTE*, many BHBs showing the VHS were discovered (see Done et al. 2007[31] for a review). At present, these four states are widely recognized. Figure 2.13 shows examples of the X-ray spectra of some BHBs in the LHS, HSS, and VHS.

In addition to these well-established states, yet another state — the apparently standard state (ApSS) — was proposed by Kubota & Makishima (2004)[76]. The spectral shape of this state is similar to that of the HSS, but there are some differences from the HSS (see § 2.5.4). At least two Galactic BHBs are reported to show this state: XTE J1550–564 (Kubota & Makishima 2004[76]) and 4U 1630–47 (Abe et al. 2005[1]). Figure 2.14 shows a behavior on the disk luminosity versus innermost disk temperature plot of a BHB in three different states.

2.5.1 LHS — Low-Hard State

In general, the LHS is the faintest state (0.01–0.04 $L_{\rm Edd}$, Maccarone 2003[88]), which shows a PL spectrum with a photon index $\Gamma = 1.5$–1.9 in 2–10 keV (Esin et al. 1997[38]; see Figure 2.13a).

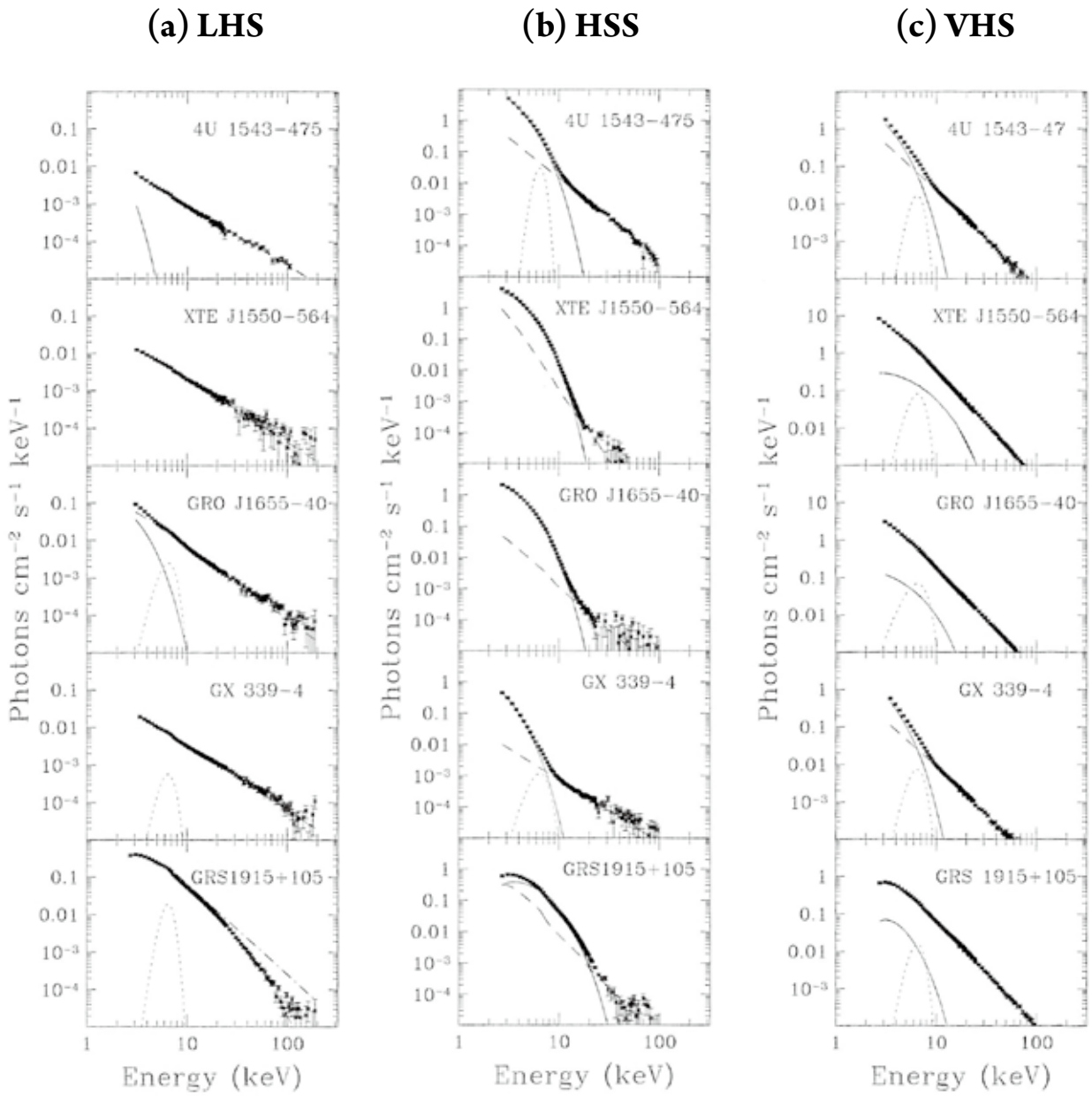

Figure 2.13: Examples of the X-ray spectra of five Galactic BHBs in the (a) LHS, (b) HSS, and (c) VHS (McClintock & Remillard 2006[103]). The solid, dashed, and dotted lines represent the accretion disk, PL, and Fe line components, respectively.

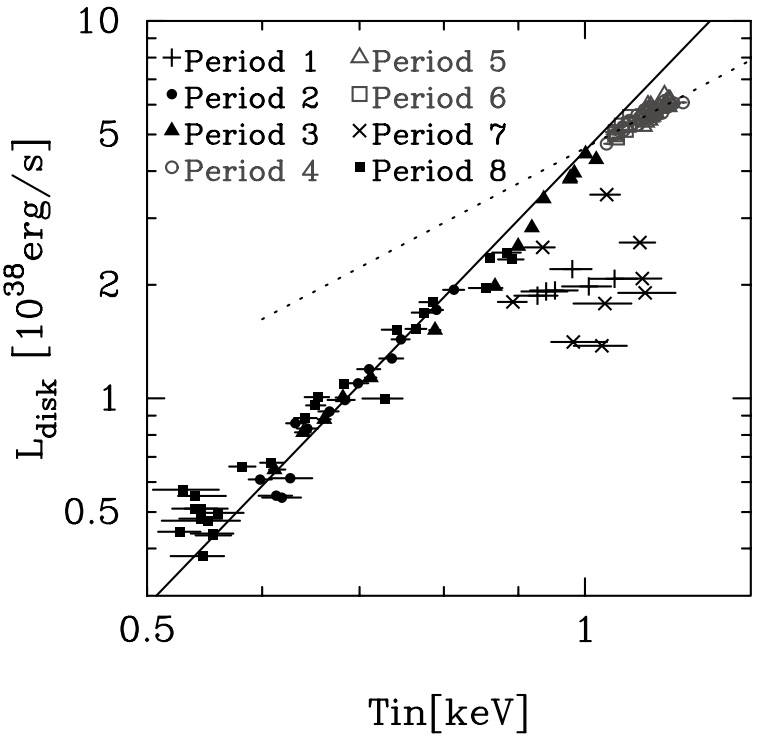

Figure 2.14: Plot of the disk luminosity against the observed $T_{\rm in}$ in a case of XTE J1550−564 (Kubota & Makishima 2004[76]). The solid and dashed lines show the $L_{\rm X,MCD} \propto {T_{\rm in}}^4$ and $\propto {T_{\rm in}}^2$ relations. The HSS is expressed as the periods 2, 3, and 8. The VHS is the periods 1, 7, and the ApSS is the periods 4, 5, 6.

2.5.2 HSS — High-Soft State

The HSS is generally brighter than the LHS, and is a thermal state with a convex-shaped spectrum. The spectrum can be fitted by an MCD model (Pringle 1981[131]), which is an approximation for the standard disk spectra, besides the variable hard-tail component, which is dominant above ∼10 keV (Figure 2.13b).

2.5.3 VHS — Very High State

The VHS usually shows an X-ray luminosity comparable to or higher than that of the HSS and a steep PL-like spectrum (typically $\Gamma \sim 2.5$, Esin et al. 1997[38]; see Figure 2.13c). The spectrum is considered to be a mixture of a weak disk component and a strong Comptonized component.

2.5.4 ApSS — Apparently Standard State

The ApSS is a thermal state, which is brighter ($L_{\rm X} \gtrsim 0.3\ L_{\rm Edd}$) than the other states. At least two Galactic BHBs are reported to show this state: XTE J1550–564 (Kubota & Makishima 2004[76]) and 4U 1630–47 (Abe et al. 2005[1]). The spectral shape in the ApSS is better represented by a slim disk model than the MCD model. If the spectra in this state are fitted with the MCD model, the following three anomalies appear (Kubota & Makishima 2004[76]; Abe et al. 2005[1]): (i) Excess emission is found below 5 keV and above 10 keV (Figure 2.15). (ii) The innermost disk temperature is higher than that in the HSS. (iii) The innermost disk radius tends to decrease with the increasing the disk temperature (Figure 2.16).

In the HSS, in contrast, the innermost disk temperature is rather constant (e.g., Ebisawa et al. 1993[35]). Some of these anomalies can be solved either by using the slim-disk model instead of the MCD model (Kubota & Makishima 2004[76]; Abe et al. 2005[1]), or by introducing spectral hardening to the MCD model as a function of the accretion rate (Davis et al. 2006[25]; McClintock et al. 2007[104]). Although it is yet unclear if the ApSS should be considered to be an independent state or an extension of the HSS, we treat the four states (LHS, HSS, VHS, and ApSS) as different states in this thesis.

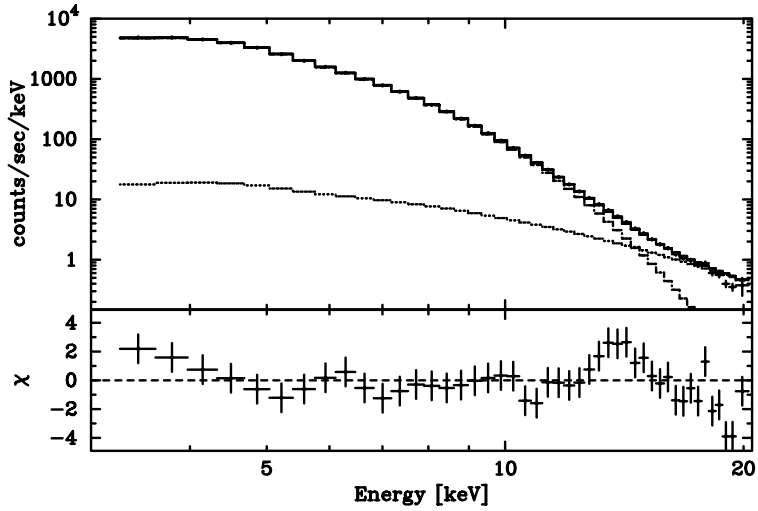

Figure 2.15: Typical spectrum of XTE J1550−564 in the ApSS by *RXTE*/ASM (Kubota & Makishima 2004[76]). The top panel shows the spectrum (*pluses*) and the best-fit model (PL plus MCD). The bottom panel shows the residual from the best-fit model.

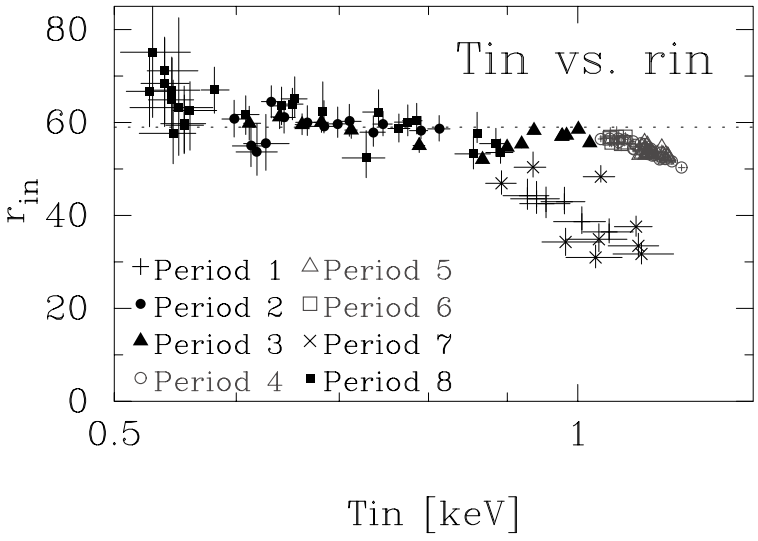

Figure 2.16: Same as Figure 2.14, but for innermost disk radius $r_{\rm in}$ as a function of $T_{\rm in}$ (Kubota & Makishima 2004[76]).

2.6 Spectral States of ULXs

It is known that most ULXs are variable sources, but the flux variable range of ULXs is much smaller than that of Galactic BHBs. When $f_{\rm max}$ and $f_{\rm min}$ are respectively defined as the observed maximum and minimum flux, $f_{\rm max}/f_{\rm min}$ of transient BHBs is 10^{5-8} (§ 2.5). On the other hand, $f_{\rm max}/f_{\rm min}$ of each ULX is only 2–10 (e.g., La Parola et al. 2001[80]; Feng & Kaaret 2006[42]; Zezas et al. 2006[194]). According to a statistical study of ULXs by Liu (2008)[84], the average luminosities of ∼84% of all the observed ULXs are within the range of 10^{39-40} ergs s^{-1}. As a result, in the most cases, the luminosity of ULXs is observed as 10^{39-41} ergs s^{-1}. Figure 2.17 shows an example of the long-term light curve of a ULX derived by several satellites.

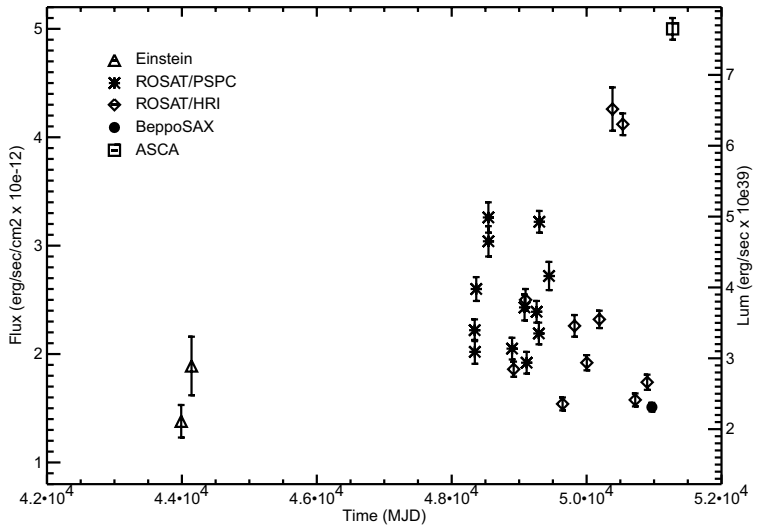

Figure 2.17: Light curve of 20 years (from 1979 through 1999) in the 0.5–2.4 keV band (M 81 X-9; La Parola et al. 2001[80]). The results of different satellites are shown in different symbols. The luminosities are calculated by assuming a distance of 3.4 Mpc.

After the advent of X-ray satellites equipped with X-ray CCD cameras (e.g., *ASCA*, *Chandra*, *XMM-Newton*, *Swift*, and *Suzaku*), at least two different spectral states in ULXs have been discovered. The spectrum in each state has the PL shape and the convex shape (e.g., Makishima et al. 2000[90]; Mizuno et al. 2007[112]; Soria et al. 2009[154]; Feng & Kaaret 2010[43]). The convex shape can be reproduced by a single MCD model (e.g., Makishima et al. 2000[90]). In particular, several ULXs show a state transition between the two in the range of $\lesssim 10^{40}$ ergs s^{-1} (La Parola et al. 2001[80] for M 81 X-9; Kubota et al. 2001[75]

for IC 342 sources 1 and 2; Isobe et al. 2009[66] for NGC 2403 source 3). For the four ULXs at least, the convex state is brighter than the PL state by from a factor of a few to one order of magnitude. Figure 2.18 shows an example of X-ray spectra in each state of a ULX.

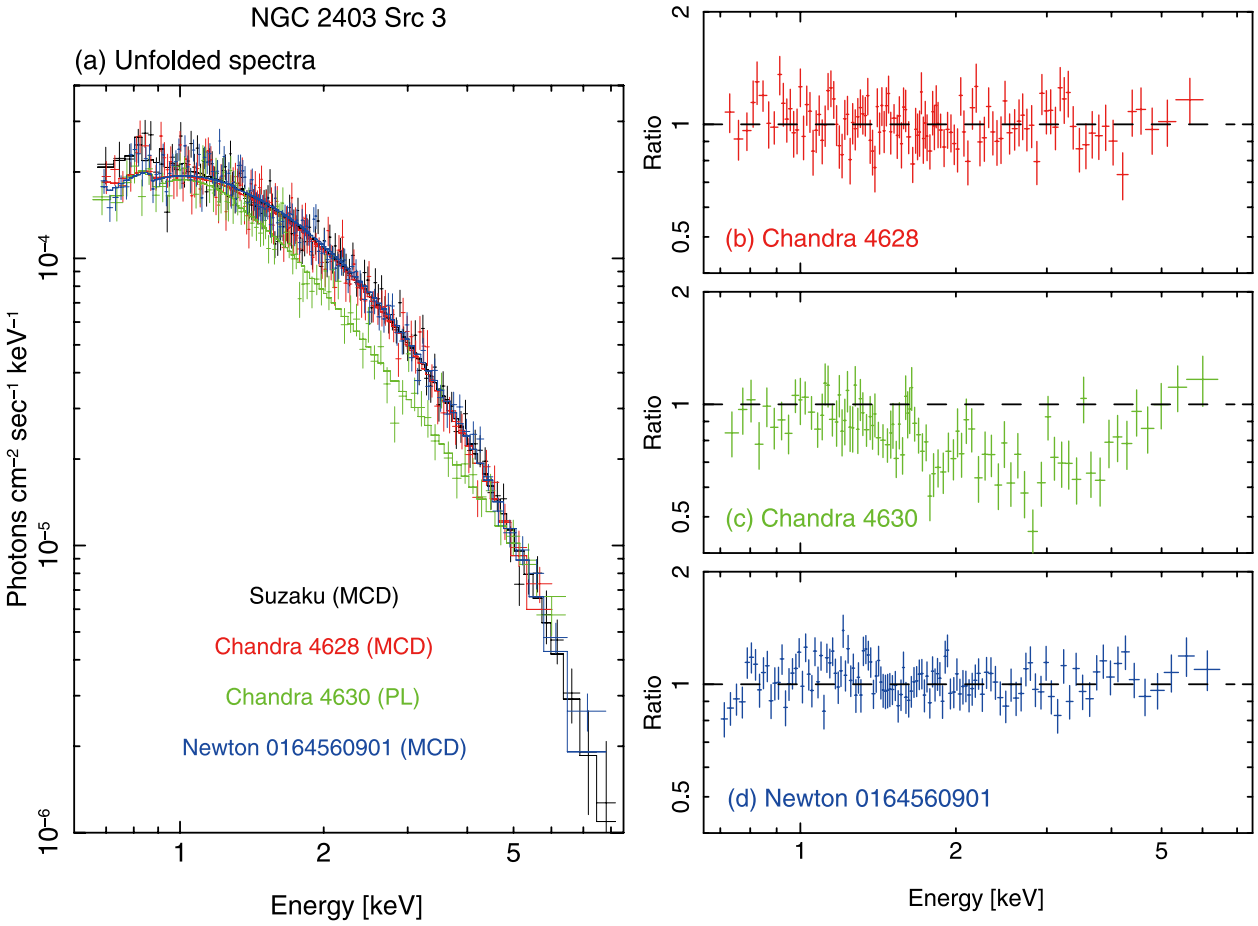

Figure 2.18: Examples of the spectra in the two states (PL and convex) of the ULX NGC 2403 source 3 (Isobe et al. 2009[66]). The spectra (*pluses*) and the best-fit model (*solid histogram*) of different observations are shown in different colors. (a) The unfolded spectra. (b)–(d) The residuals from the best-fit by the MCD model.

In the early 2000's, Kubota et al. 2001[75] and Mizuno et al. 2001[111] proposed that the convex and the PL shape states of ULXs correspond to the slim disk state (called the ApSS in this thesis) and the VHS of Galactic BHBs, respectively. For the convex state, the main reason is that the derived innermost disk radius is inverse proportion to the innermost disk temperature ($r_{\rm in} \propto {T_{\rm in}}^{-1}$; Figure 2.19a). Consequently, the luminosity is proportional to ${T_{\rm in}}^2$, which is an expected property of the slim disk and not of the standard disk (see

§ 2.4.3). In fact, three ULXs move along the constant BH mass lines in the slim disk model (Figure 2.19b). This was considered as a strong evidence that ULXs in the convex state have a slim disk. On the other hand, the PL state shows some evidence for the disk Comptonization. For example, IC 342 source 1 shows a different power in the PL fitting in different energy bands; $\Gamma \sim 1.54$ in the low energy band (0.7–4 keV) and $\Gamma \sim 2.4$ in the high energy band (5–10 keV). This is opposite with BHBs in the LHS; 5–10 keV spectrum is harder than 0.7–4 keV spectrum. This characteristic can be explained by the VHS picture (a combination of a faint disk plus a Comptonized tail).

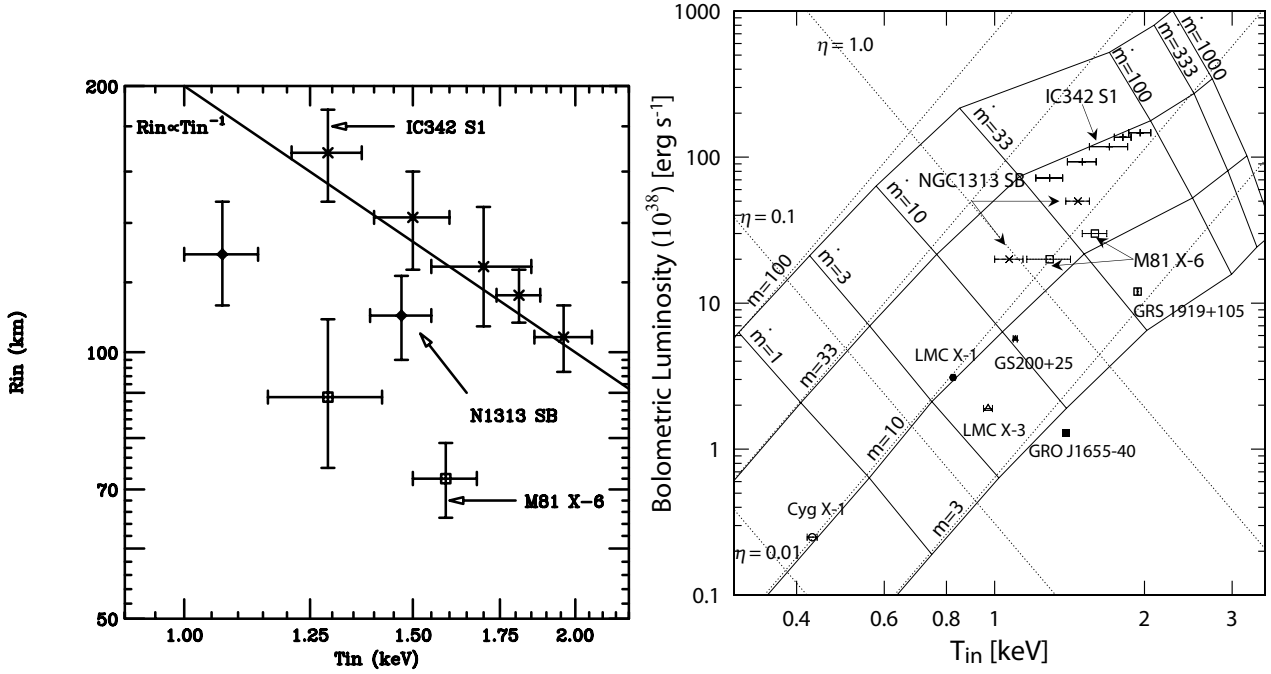

(a) (b)

Figure 2.19: (a) Innermost disk radius (Mizuno et al. 2001[111]) and (b) disk luminosity (Watarai et al. 2001[185]) as a function of $T_{\rm in}$. IC 342 S1 (source 1), N1313 SB (NGC 1313 X-2), and M 81 X-6 are ULXs, while the others are Galactic BHBs. m, $\dot{m}$, and η indicate the BH mass ($M_\odot$), the mass accretion rate ($\dot{M}c^2/L_{\rm Edd}$), and the normalized luminosity ($L/L_{\rm Edd}$). The solid and dashed lines are simulated according to the slim disk and the standard disk model, respectively.

However, recent studies found observational evidence that may contradict to this picture, especially in a high luminosity range ($>10^{40}$ ergs s^{-1}). First, Feng & Kaaret (2010)[43] found a ULX (in M 82) having convex spectra with luminosity varying to the fourth power of the $T_{\rm in}$ (Figure 2.20). This behavior clearly indicates the standard disk picture and not the slim

disk. Second, by a statistical study, Berghea et al. (2008)[13] found that the most luminous ULXs tend to be harder. The observed luminosity is larger than that commonly seen in convex shape state, and can be reproduced by a single PL without a thermal accretion disk. The state may be different from the two aforementioned states (the VHS and the ApSS). In fact, they estimated that this state is new and dubbed the ultraluminous state (Roberts 2007[140]; Gladstone et al. 2009[56]), which is expected in stellar mass BHBs in the highest state (Kawashima et al. 2009[72]).

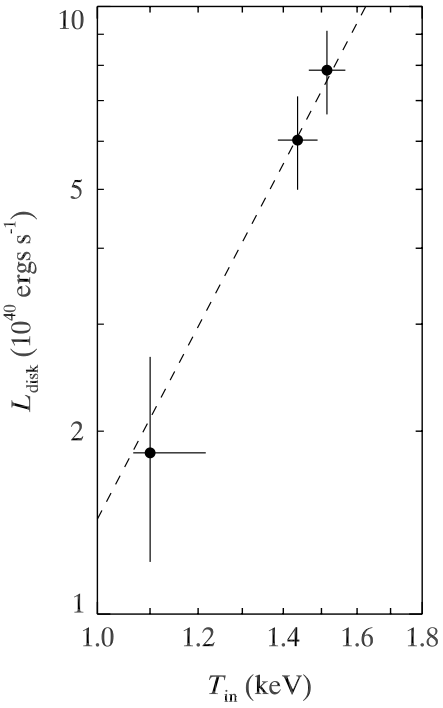

Figure 2.20: Bolometric luminosity $L_{\rm disk}$ against the innermost disk temperature $T_{\rm in}$ of a ULX in M 82 with *Chandra* (Feng & Kaaret 2010[43]). The dashed line represents $L_{\rm disk} \propto {T_{\rm in}}^4$.

Chapter 3

Observing Facilities

In this chapter, we review three X-ray satellites: *Chandra* (§ 3.1), *XMM-Newton* (§ 3.2), and *MAXI* (§ 3.3). We present the overview, telescopes and equipped instruments of these satellites.

Contents

3.1 *Chandra*

3.1.1 Overview

The *Chandra* X-ray Observatory (Weisskopf et al. 2002[186]) is the third in the series of the Great Observatories, and was launched on the Space Shuttle Columbia (STS-93) on 1999 July 23 by the National Aeronautics and Space Administration (NASA). The satellite was putted into a highly elliptical orbit with the perigee and the apogee altitude of ∼10,000 and ∼140,000 km, respectively. Unlike satellites in the near-Earth orbit interrupted frequently by Earth occultation of observing targets, the *Chandra*'s orbit allows for uninterrupted observing intervals of more than 170 ks due to its orbital period of about 64 hours.

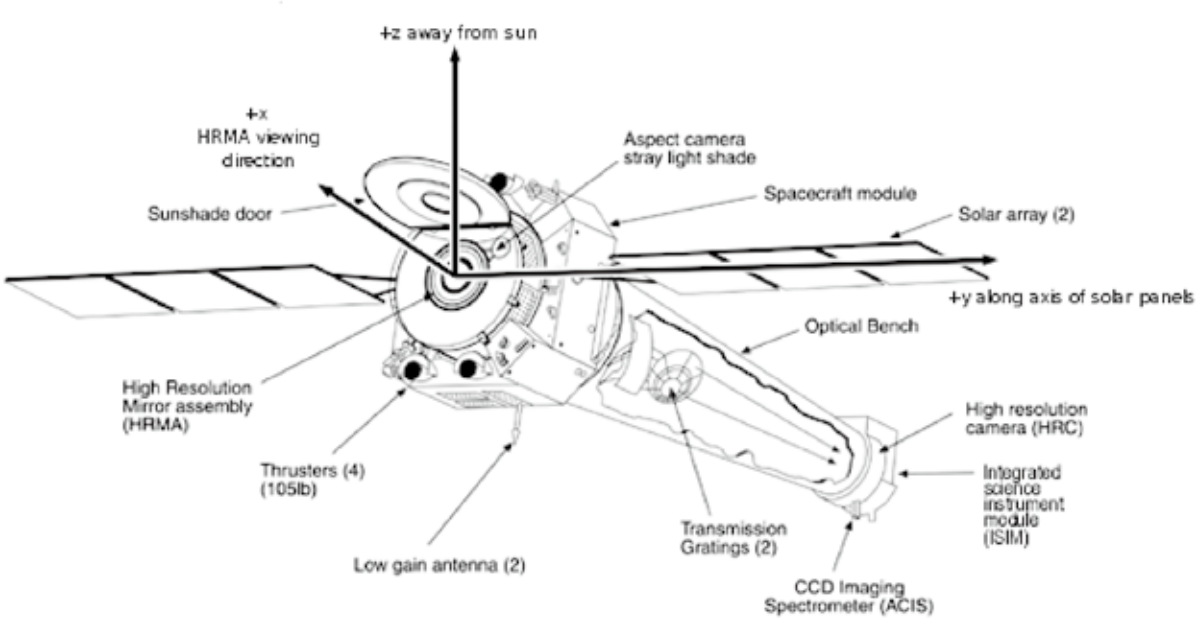

Figure 3.1: Schematic view of the *Chandra* satellite (*Chandra* Proposers' Observatory Guide 2009[21]).

An outline of *Chandra* is shown in Figure 3.1. *Chandra* has an X-ray telescope (High Resolution Mirror Assembly; HRMA), and two focal plane instruments: X-ray CCD arrays (Advanced CCD Imaging Spectrometer; ACIS-I and ACIS-S) and micro-channel plate arrays (High Resolution Camera; HRC-I and HRC-S). The satellite also has two grating systems (High/Low Energy Transmission Grating; HETG and LETG). The details can be found in

the *Chandra* Proposers' Observatory Guide (2009)[21].

Chandra was designed to provide an order-of-magnitude advance over previous X-ray astronomy missions in spatial resolution. At the optical on-axis, *Chandra* has an unprecedented spatial resolution of $\sim 0''.5$. The satellite attitude is controlled and determined by the Pointing Control and Aspect Determination (PCAD) system at a higher accuracy than the spatial resolution.

3.1.2 HRMA — High Resolution Mirror Assembly

Configuration

The X-ray telescope HRMA of *Chandra* consists of four pairs of grazing-incidence mirrors called the Wolter-I type geometry (Figure 3.2). The first stage mirror of each pair is a paraboloid and the second stage is a hyperboloid. The X-ray optics is reviewed by Aschenbach (1985)[6]. The mirror pair diameter range is 0.65–1.23 m, and the focal length is about 10 m. The HRMA has very thick cylinders (1.5 cm) for an X-ray telescope (that of *XMM-Newton* is 0.47–1.07 mm).

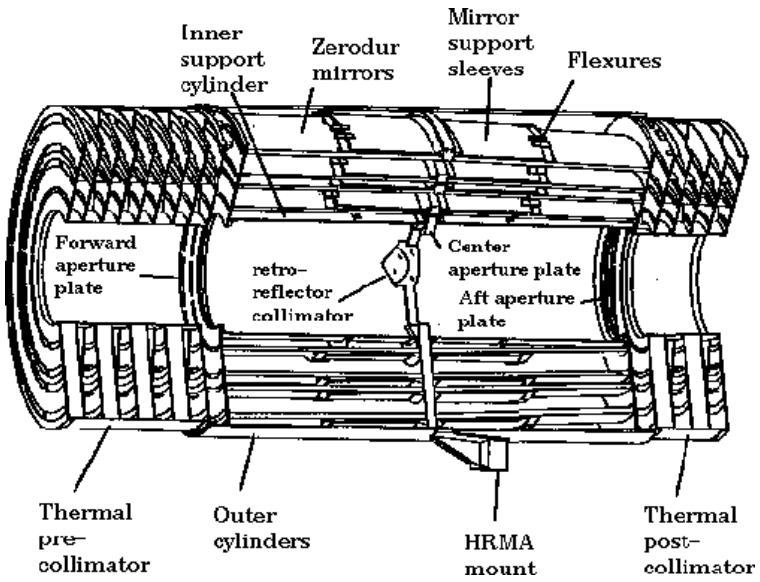

Figure 3.2: Schematic view of the HRMA (*Chandra* Proposers' Observatory Guide 2009[21]).

Effective Area

The effective area of an X-ray telescope depends on both the incident X-ray energy and off-axis angle (distance from the optical axis). The on-axis effective area is about 800 cm^2 at 0.25 keV, and declines to 400 cm^2 at 5.0 keV, and 100 cm^2 at 8.0 keV (Figure 3.3a). The effective area decreases as the increasing off-axis angle depending on the energy (Figure 3.3b). The effects of both the energy variation and the off-axis vignetting are strongly coupled.

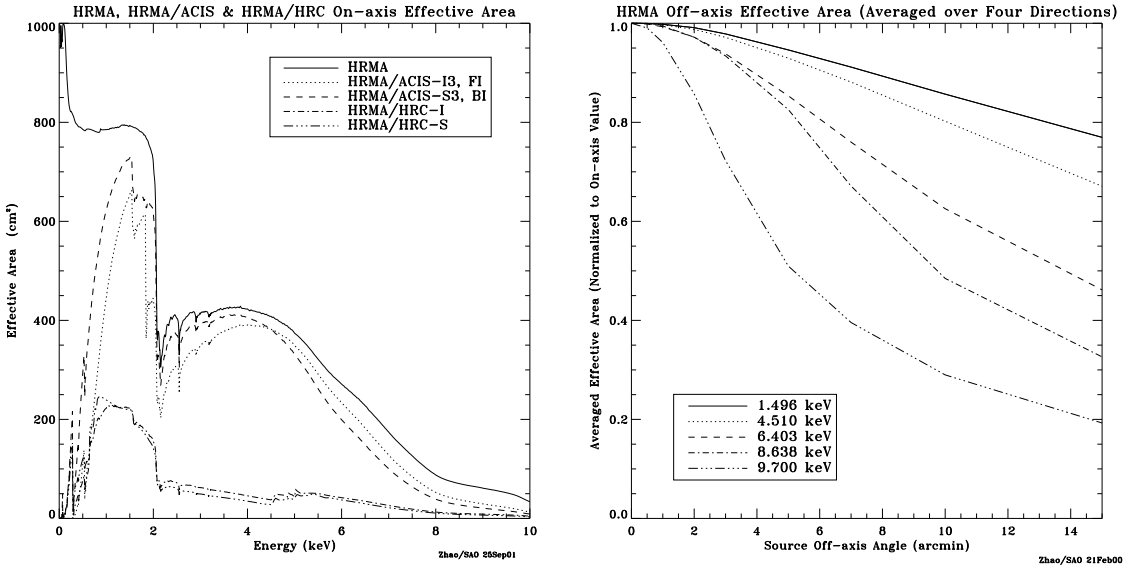

(a) (b)

Figure 3.3: Dependence of the effective area on the incident X-ray energy and off-axis angle (*Chandra* Proposers' Observatory Guide 2009[21]). (a) HRMA effective area versus X-ray energy. The solid line shows the total effective area, and the other lines show the expected effective area convolved with the detector quantum efficiency: dotted (front-illuminated ACIS), dashed (back-illuminated ACIS), dashed-and-dotted (HRC-I), and dashed-and-triplicated-doted (HRC-S) curves. (b) HRMA effective area versus off-axis angle. The curves show the off-axis behavior at five selected energies, with the values being normalized to the on-axis value at that energy.

Point Spread Function

The point spread function (PSF) is a spatial distribution function over the detector surface for a point-like X-ray source at infinity. Similarly to the effective area, the PSF depends on the energy and off-axis angle. The on-axis PSF of the HRMA is very sharp, and most of

X-ray photons are collected within 1″-radius region (Figure 3.4). Figure 3.5 gives the on-axis encircled energy fraction, approximating the Gaussian shape. For example, at 4.510 keV, 50% photons are included in about 0.″35-radius, which is called the half-power radius. Figure 3.6 shows the dependence of PSFs on the off-axis angle at 1.49 and 6.40 keV.

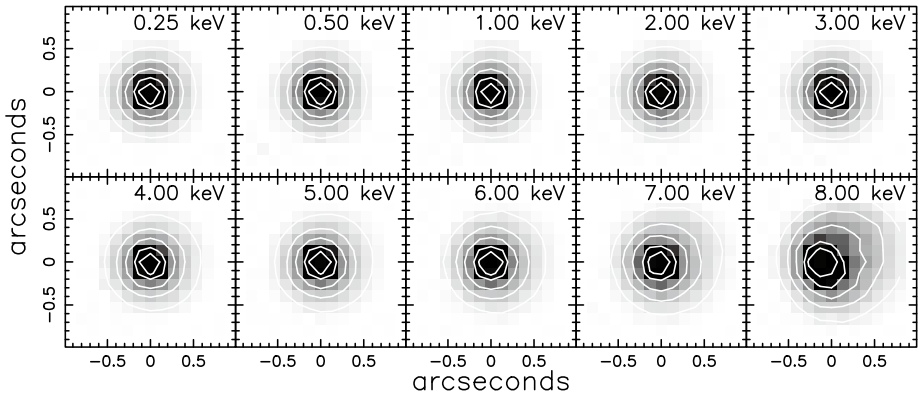

Figure 3.4: Simulated on-axis images of on-axis mono-energetic point sources with aspect blurring (*Chandra* Proposers' Observatory Guide 2009[21]). The gray scale is a linear stretch; surface brightness contours are at 90%, 80%, 60%, 40%, and 20% of the peak brightness.

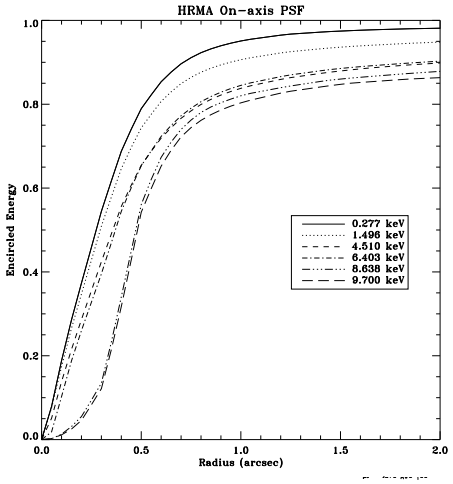

Figure 3.5: Encircled energy fraction as a function of radius from the PSF center at the optical axis (*Chandra* Proposers' Observatory Guide 2009[21]). The curves show the behavior at several energies.

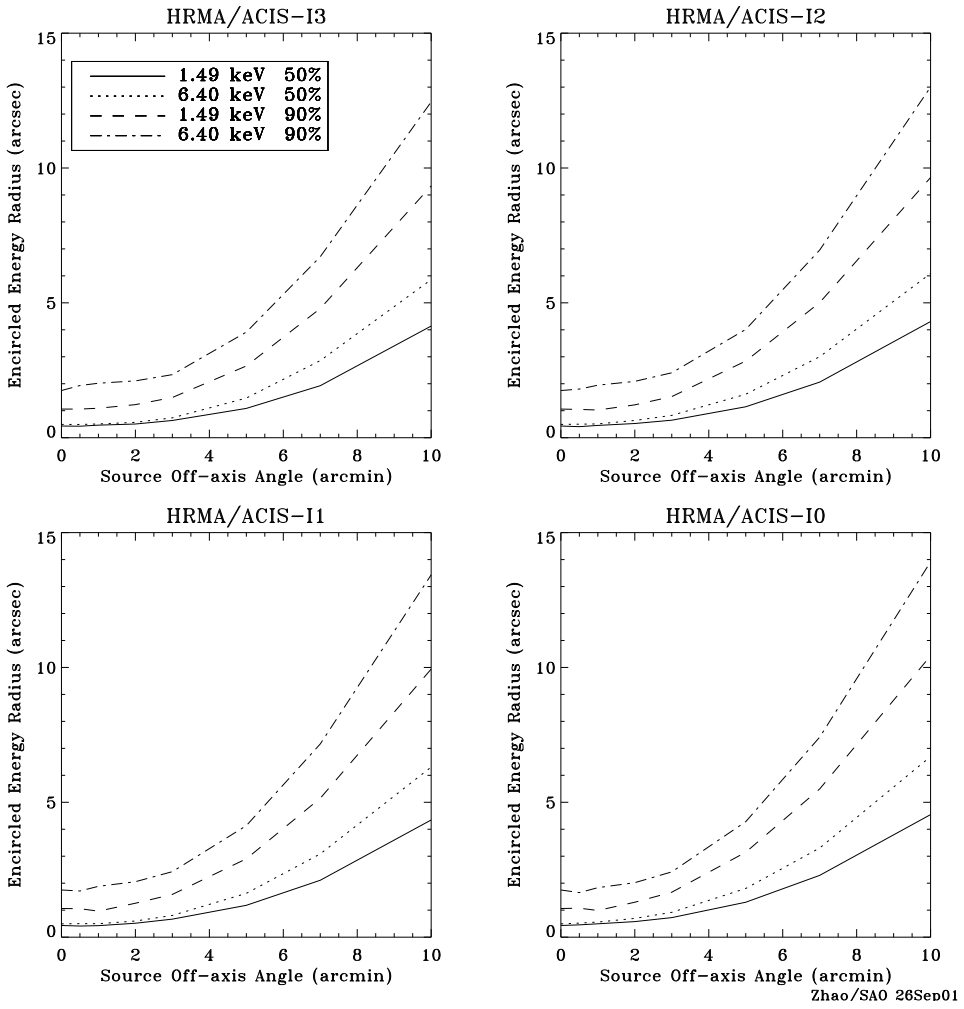

Figure 3.6: HRMA/ACIS-I encircled energy radii for circles enclosing 50% and 90% of the power at 1.49 and 6.40 keV as a function of off-axis angle (*Chandra* Proposers' Observatory Guide 2009[21]).

3.1.3 ACIS — Advanced CCD Imaging Spectrometer

Configuration

The ACIS (Garmire et al. 2003[51]) contains 10 chips, which are 1024×1024 pixel CCDs a the pixel scale of 0.492″ pixel^{-1} (Figure 3.7). The field of view (FOV) of a chip is ∼500″×500″. The ACIS-I and ACIS-S are a 2×2 and a 1×6 arrays, respectively. The former array is mainly used for imaging, while the latter is used either for imaging or grating spectroscopy. Two chips (ACIS-S1 and S3) are back-illuminated (BI) CCDs, and the others are front-illuminated (FI). Any combination of up to six CCDs can be operated simultaneously.

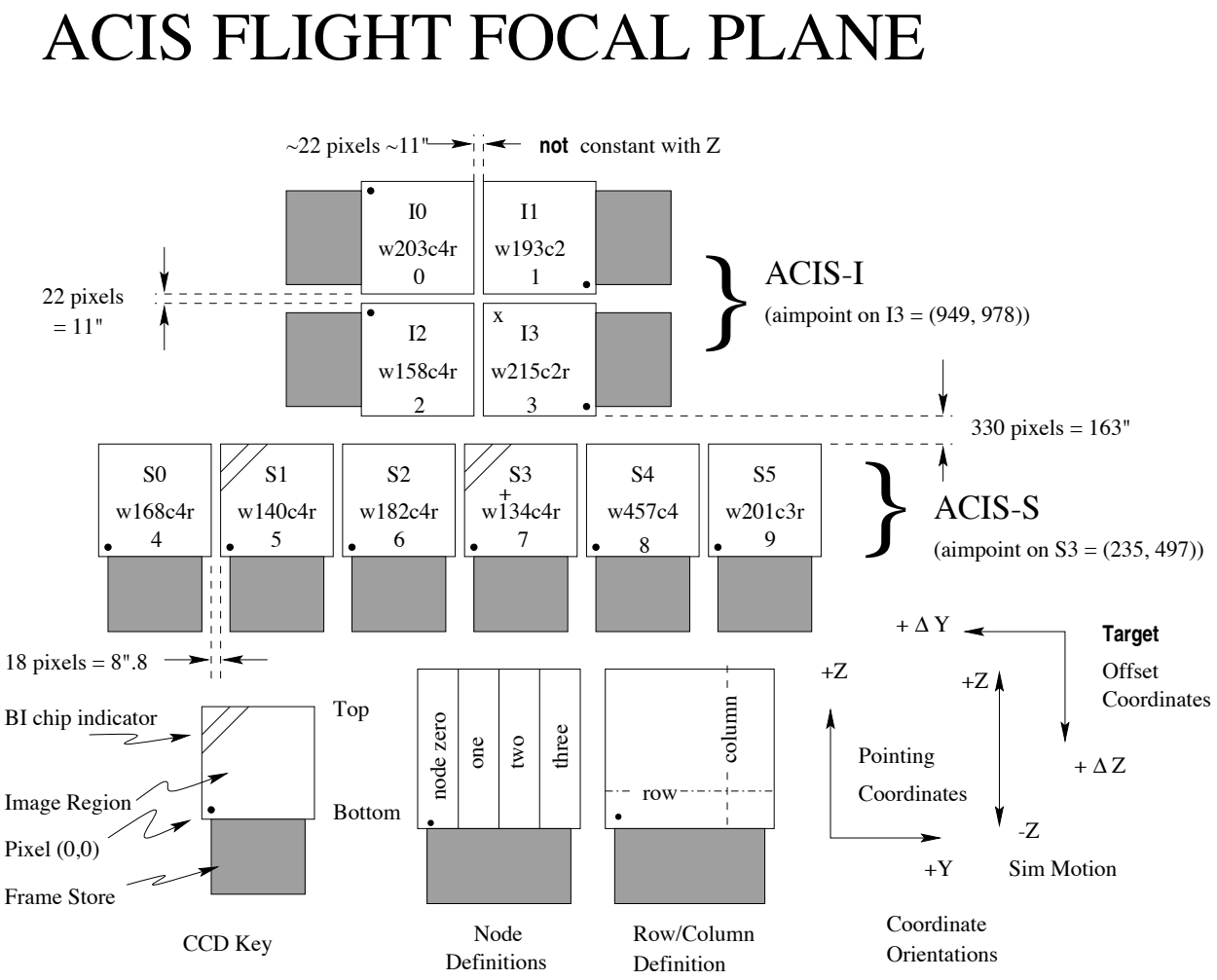

Figure 3.7: Schematic view of the ACIS focal plane (*Chandra* Proposers' Observatory Guide 2009[21]). Top: The ACIS-I and the ACIS-S arrays. Bottom: Geometry of one chip.

Detection Efficiency

The combined HRMA/ACIS effective area is shown in Figure 3.8. The edge at 1.838 keV is caused by the Si K-edge absorption. Low energy X-rays are mainly absorbed by two factors: Optical Blocking Filter (OBF) and the gate structure of the CCD chips. Although the OBF is necessary because the X-ray CCDs react on optical photons, it absorbs low energy X-rays too. The filters are placed just over the CCDs between the chips and the HRMA. In the case of ACIS-S, they are composed of aluminum (1000 Å), polyimide (a polycarbonate plastic; 2000 Å), and aluminum (300 Å), while in the ACIS-I, 1200 Å, 2000 Å, and 400 Å. Since the gate structures of the BI chips are mounted in the direction opposite to the HRMA, the quantum efficiency of the BI is larger than those of the FI in the low energy band. In contrast, at higher energies, the FI chips are sensitive because its depletion region is thicker than that of the BI.

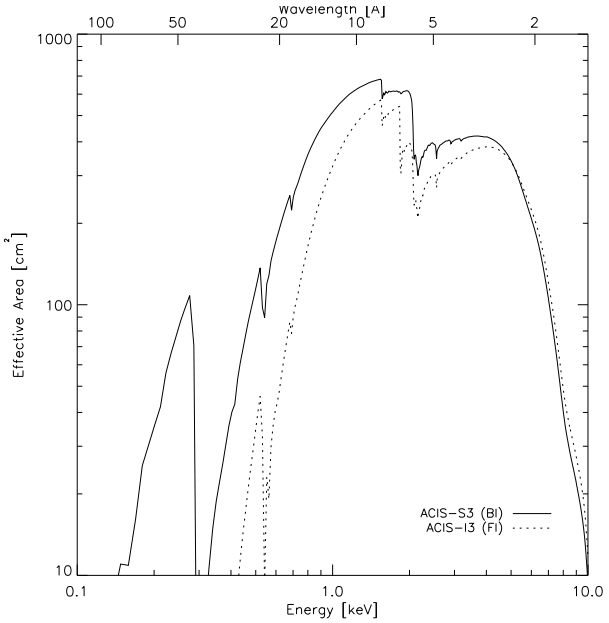

Figure 3.8: Effective area as a function of energy of the HRMA/ACIS (*Chandra* Proposers' Observatory Guide 2009[21]). The dashed line is for the FI CCD ACIS-I3, and the solid line is for the BI CCD ACIS-S3.

Energy Resolution

Figure 3.9 shows the pre-launch energy resolution (Full Width at Half Maximum; FWHM) as a function of energy. The resolution is characterized by three factors: statistical fluctuation in the number of electrons, the pre-amplifier readout noise, and the thermal noise. At the ACIS operating temperature of −120 °C, the thermal noise is negligible.

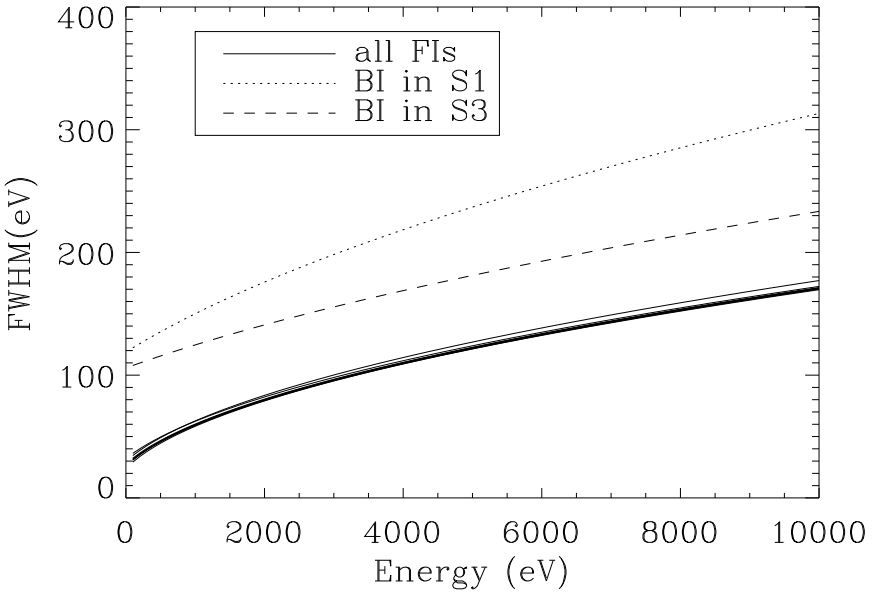

Figure 3.9: Pre-launch energy resolution as a function of energy (*Chandra* Proposers' Observatory Guide 2009[21]). These data were taken at −120 °C.

3.2 *XMM-Newton*

3.2.1 Overview

The *XMM-Newton* observatory (Jansen et al. 2001[79]) is the second cornerstone of the Horizon 2000 Programme, and was launched on the Ariane-V rocket on 1999 December 10 by the European Space Agency (ESA). Like *Chandra*, the satellite was put into a highly eccentric orbit with a perigee and an apogee altitude of ∼6,000 and ∼115,000 km, respectively. The orbital inclination is 33°. The orbital period is about 48 hours, and the time available for scientific data analysis is about 140 ks per orbit.

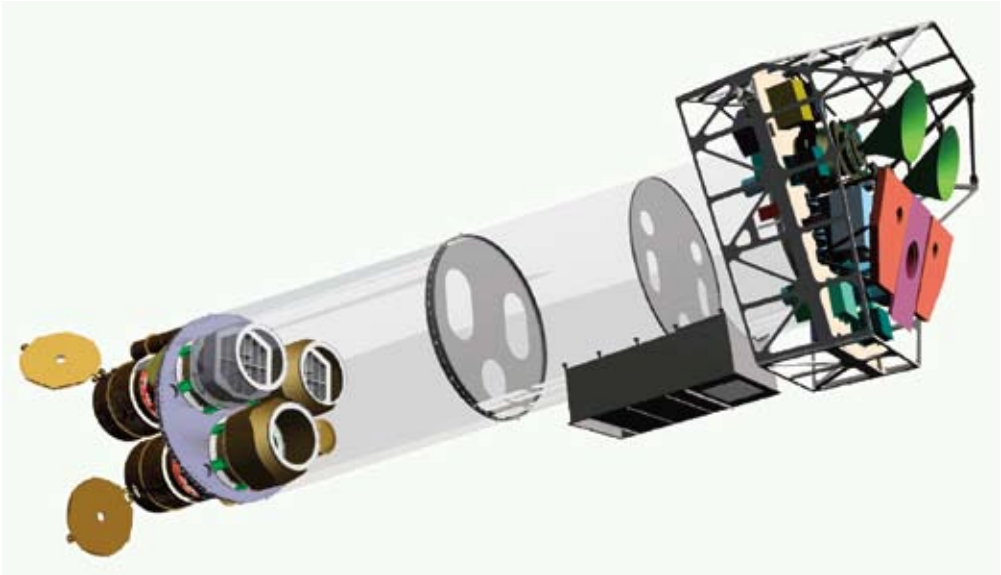

Figure 3.10: Schematic view of the *XMM-Newton* satellite (*XMM-Newton* Users Handbook 2010[188]).

An outline of *XMM-Newton* is shown in Figure 3.10. *XMM-Newton* has three X-ray telescopes with different X-ray detectors at their foci, and a 30 cm aperture optical/ultraviolet (UV) telescope. The satellite also has three types of science instruments: CCD arrays (European Photon Imaging Camera; EPIC), a grating system (Reflection Grating Spectrometer; RGS), and an optical/UV detector (Optical Monitor; OM). The EPIC is composed of three CCD cameras: MOS-1, 2, and pn. The details can be found in *XMM-Newton* Users Handbook (2010)[188].

3.2.2 X-ray Telescope

Configuration

Each of the three X-ray telescopes consists of 58 nested Wolter-I type mirrors (Figure 3.11). The focal length is about 7.5 m.

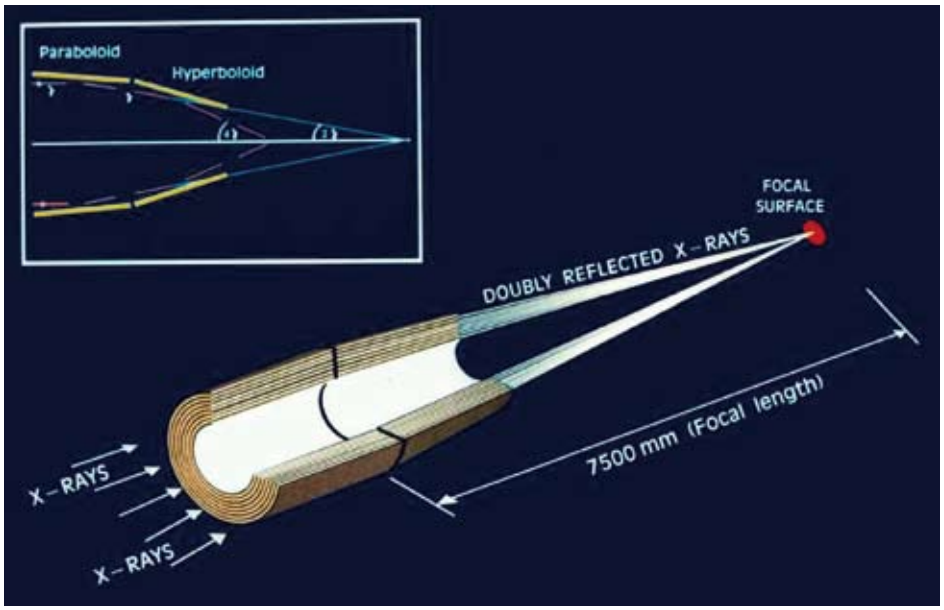

Figure 3.11: Schematic view of the X-ray telescope with the pn camera in focus (*XMM-Newton* Users Handbook 2010[188]).

Effective Area

The effective area of the X-ray telescopes is larger than that of *Chandra*. The on-axis effective area (at 1.5 keV) of each telescope is about 1,550 cm^2, i.e., the total is 4,650 cm^2 (Figure 3.12a). The effective area decreases as the increasing off-axis angles depending on the energy (Figure 3.12b).

Point Spread Function

The imaging quality of an X-ray telescope is represented by the size of PSF. The size of PSF of *XMM-Newton* is larger than that of *Chandra* by at least a factor of 10. The on-axis

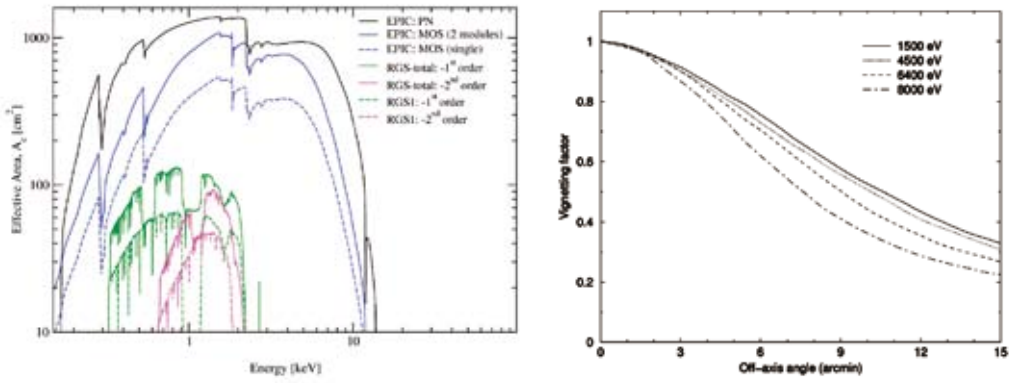

(a) (b)

Figure 3.12: Dependence of the effective area on the X-ray energy and source off-axis angle (*XMM-Newton* Users Handbook 2010[188]). (a) On-axis effective area convolved with detector quantum efficiency versus X-ray energy. (b) Vignetting factor as a function of off-axis angle for the pn camera. The curves show the off-axis behavior at four selected energies.

PSFs for a point source at infinity obtained by each detector are shown in Figure 3.13. The radial substructures are caused by the spiders holding the mirror shells. Figure 3.14 gives the on-axis encircled energy fractions of the X-ray telescopes for MOS-1 and pn. At any energies of any detectors, the 50% photons are included in about 6–8″-radius. Figure 3.15 shows the dependence of PSFs on the off-axis angle at 1.5, 5, and 9 keV.

Figure 3.13: On-axis images of the MOS-1 (*left*), MOS-2 (*center*), and pn (*right*) X-ray telescopes (*XMM-Newton* Users Handbook 2010[188]). These images are 110″ in width, and a square root intensity scale has been used to visualize the wings of the PSF.

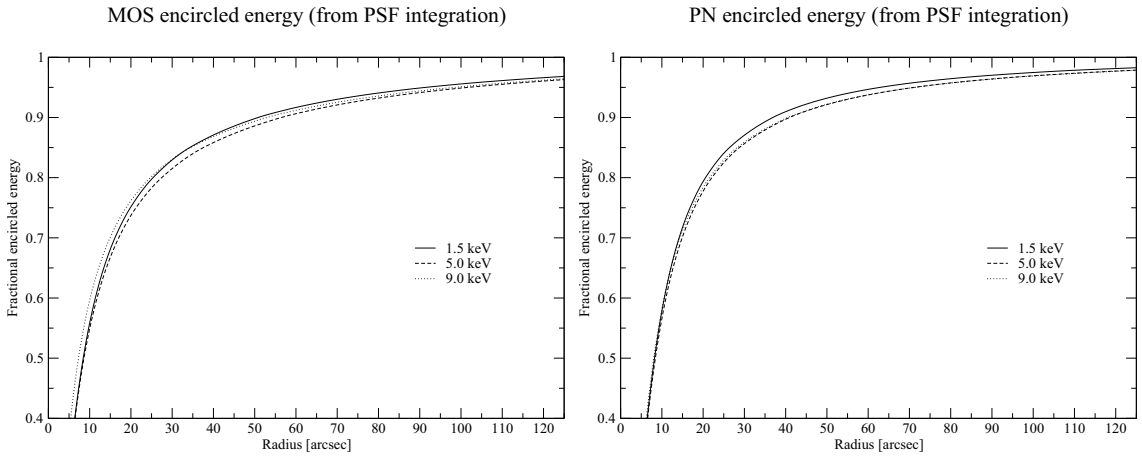

(a) (b)

Figure 3.14: Encircled energy fractions as a function of radius from the image center of (a) MOS-1 and (b) pn (*XMM-Newton* Users Handbook 2010[188]). The curves show the behavior at three selected energies.

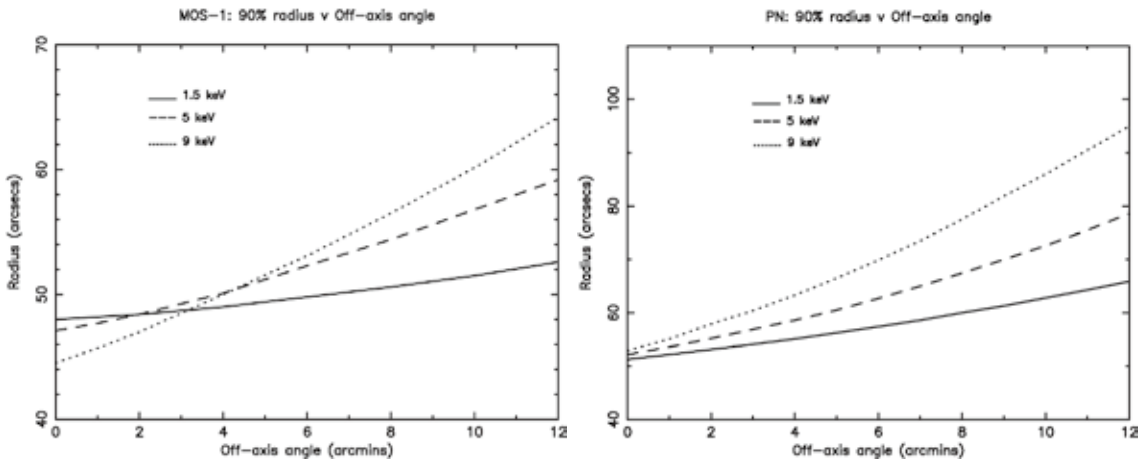

(a) (b)

Figure 3.15: 90% encircled energy radii at 1.5, 5, and 9 keV as a function of off-axis angle with (a) MOS and (b) pn (*XMM-Newton* Users Handbook 2010[188]).

3.2.3 EPIC — European Photon Imaging Camera

Configuration

Each MOS chips (Turner et al. 2001[171]) contains seven square chips, which are 600×600 pixel CCDs with a pixel scale of 1.1″ pixel^{-1} (40 μm pixel^{-1}) and has sensitivity in the 0.15–12 keV band. The two MOS cameras are rotated by 90° with respect to each other. On the other hand, the pn array (Strüder et al. 2001[156]) contains 12 rectangular chips, which are 64×200 pixel CCDs with a pixel scale of 4.1″ pixel^{-1} (150 μm pixel^{-1}) and has sensitivity in the 0.15–15 keV band. Both instruments have an FOV with a radius of ∼30′. Figure 3.16 shows the detector layout and the FOV of both types of EPIC cameras.

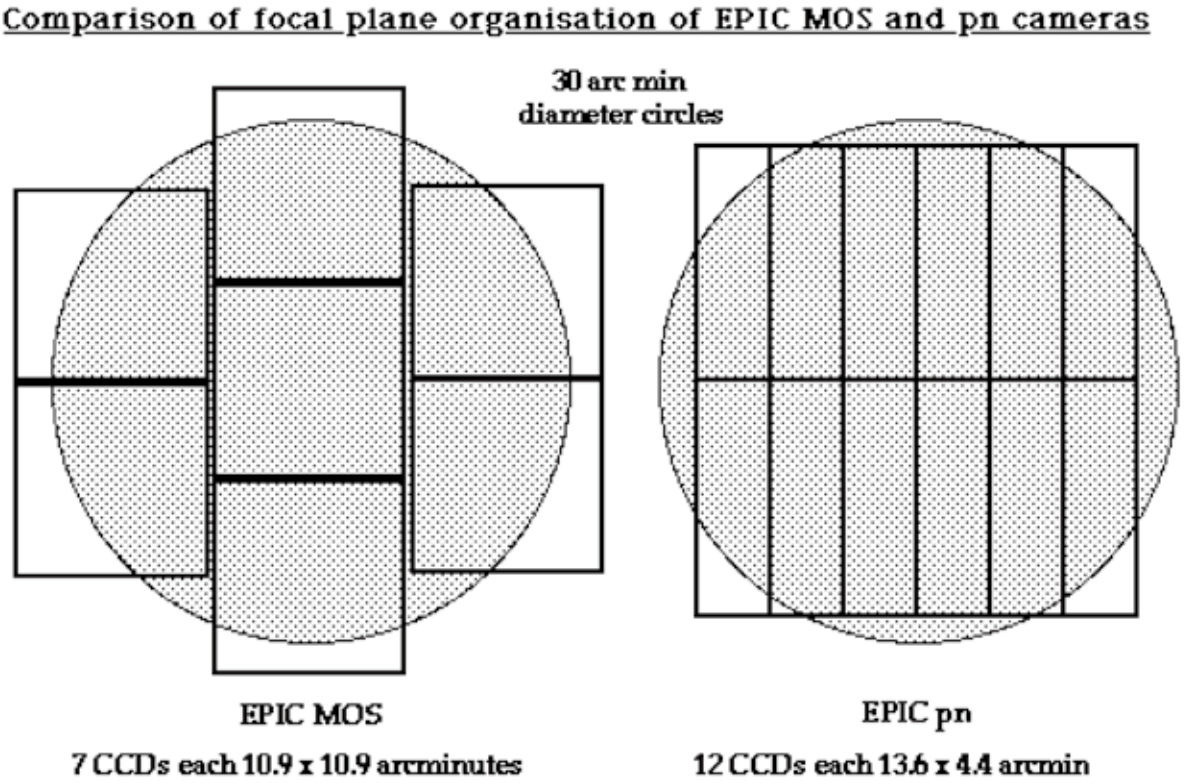

Figure 3.16: Schematic view of the FOV of EPIC MOS (*left*) and pn (*right*) by *XMM-Newton* Users Handbook (2010)[188].

There are two major differences between the MOS and pn arrays: (i) The MOS array consists of FI chips, and the pn consists of BI. (ii) The readout time of the pn arrays (73.4 ms)

is much faster than those of the MOS (2.6 s), because each column of the pn has its own readout node.

Detection Efficiency

The EPIC quantum efficiency is shown in Figure 3.17. The low energy efficiency is reduced by the OBFs and the gate structure of CCDs. Since the EPIC CCDs detect not only X-rays but also infrared, optical, and UVs, *XMM-Newton* equips the OBFs. For the EPIC CCDs, the satellite has a filter wheel with three types of the OBFs: thick, medium, and thin. The thick filter should be used for an object with the v-band magnitude m_v of 1 to 4 mag (MOS) or -2 to 1 mag (pn), while the medium and thin for m_v of 6 to 9 mag and $\sim$12 mag, respectively. Observers can select one among the three filters (or no filter) according to the brightness of the object in the optical band.

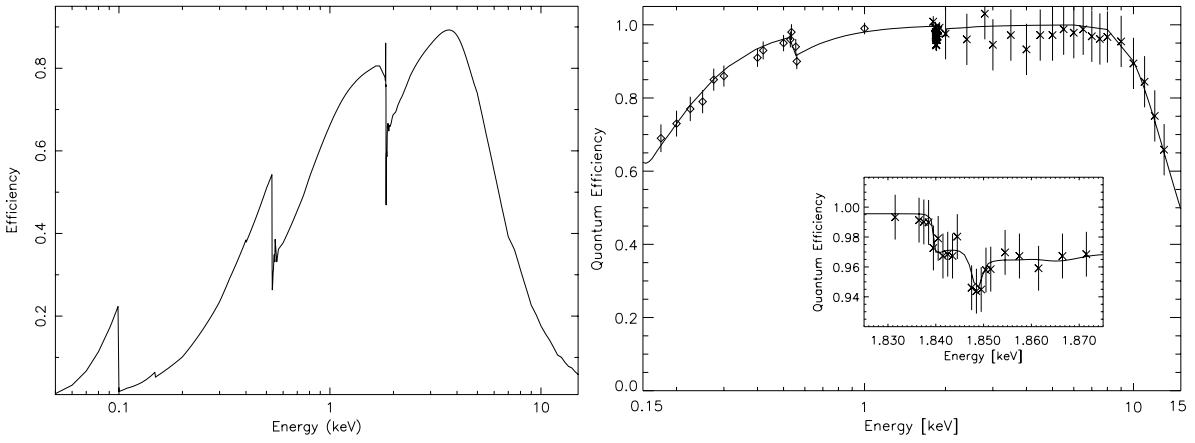

(a) (b)

Figure 3.17: Quantum efficiency of the EPIC cameras as a function of photon energy. (a) The MOS array (Turner et al. 2001[171]). (b) The pn array (Strüder et al. 2001[156]).

Energy Resolution

Figure 3.18 shows the pre-launch energy resolution (FWHM) as a function of energy. The resolution of MOS has decreased by $\sim$10% in early mission, but the problem was solved by decreasing the operational temperature between 2002 November and December. For pn, such a degradation of the FWHM has not been found.

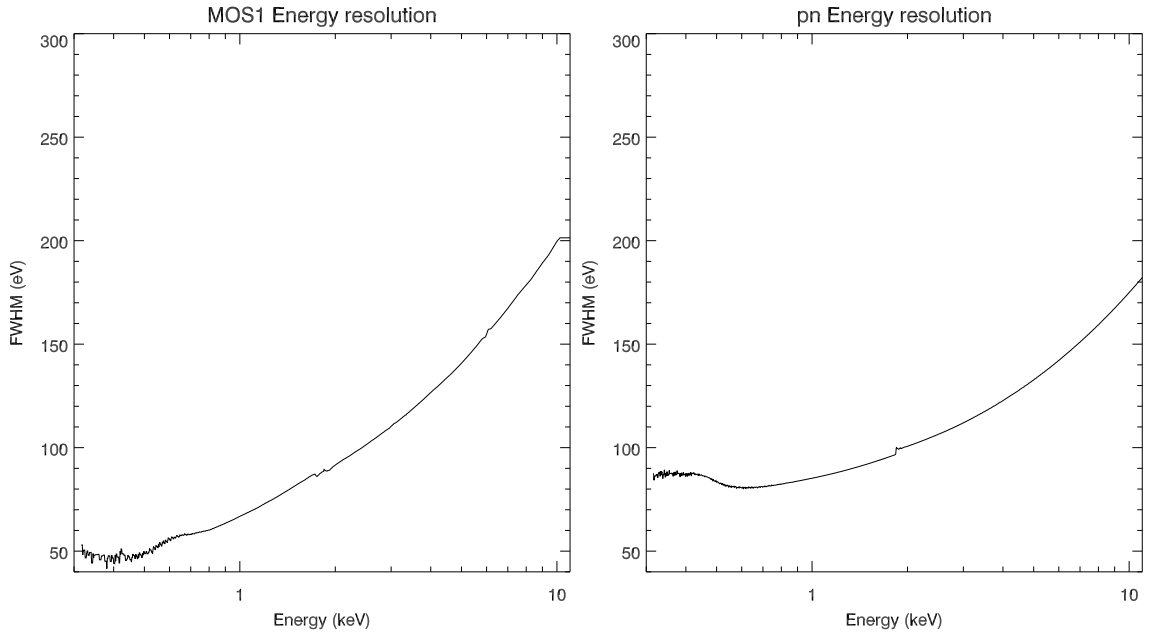

(a) (b)

Figure 3.18: Pre-launch energy resolution as a function of energy (*XMM-Newton* Users Handbook 2010[188]). (a) The MOS-1 energy resolution. (b) The pn energy resolution.

3.3 *MAXI*

3.3.1 Overview

The Monitor of All-sky X-ray Image (*MAXI*; Matsuoka et al. 2009[99]; 2010[100]) is the first mission of the all sky monitor for X-rays in Japan. The monitor was launched by the Space Shuttle Endeavor (STS-127) on 2009 July 16, and installed in the Japanese Experiment Module in the International Space Station (ISS). The ISS has a low circular orbit (the perigee of 336 km, the apogee of 346 km), and an orbital inclination of 52°, corresponding to the orbital period of about 92 minutes.

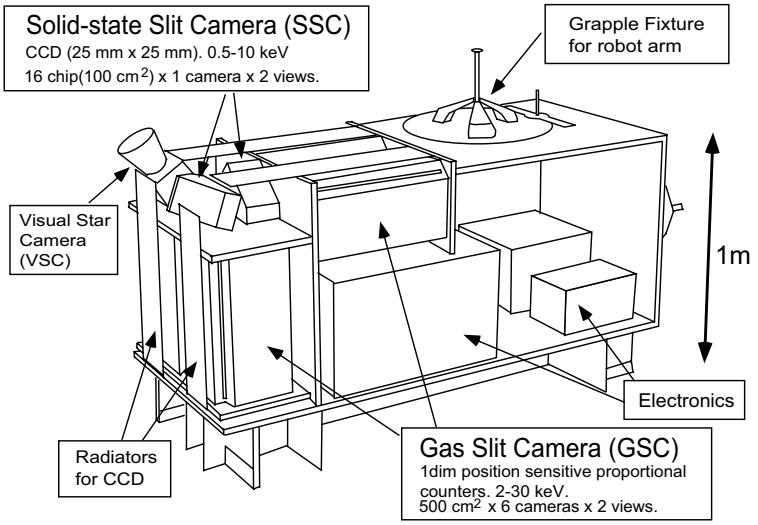

Figure 3.19: Schematic view of *MAXI* (Matsuoka et al. 1999[98]).

An outline of *MAXI* is shown in Figure 3.19. There are two types of X-ray cameras in *MAXI*: The Gas Slit Camera (GSC) and the Solid-state Slit Camera (SSC). The former camera is a gas proportional counter covering an energy range of 2–30 keV with an energy resolution of 18% at 5.9 keV. It is capable of detecting a 25 mCrab and 8 mCrab source at an exposure of one orbit and one day ($\sim$15 orbits), respectively. This sensitivity is higher than that of previous monitors by a factor of 10. While the latter is an X-ray CCD covering 0.5–12 keV with an energy resolution of $\lesssim$150 eV at 5.9 keV, and its main mission is to make all-sky X-ray maps for extended sources with a better energy resolution. In this thesis, we only use GSC because SSC is not calibrated well as of writing.

3.3.2 GSC — Gas Slit Camera

Configuration

The GSC contains six units of a conventional slit camera. Each unit consists of two one-dimensional proportional counters and slit & slat collimations (Figure 3.20a). Six counters of them are placed in the horizontal direction, thus are called GSC-H, while the others in the zenith direction, called GSC-Z. For each unit, the FOVs of the ISS scanning direction (θ) and the slit direction (ϕ) are 1.5° and 80°, respectively (Figure 3.20b). Therefore two units of both of the GSC-H and GSC-Z cover a very wide angular range of 160° for the slit direction. The FOV of the remaining central unit overlaps with each half of the FOV of both side units (Figure 3.21). The 12 counters have a detection area of 5350 cm^2 and the FOV of $\sim$1.5°$\times$160° in total.

The GSC can scan about 76% and 96% of the all sky for one orbit and one day observation, respectively. The remaining regions are inaccessible mainly for two reasons: the two polar regions (10°) and the solar vicinity ($\pm$4°). Thus, the GSC does not always monitor all X-ray sources.

The gas counters in the GSC consist of two layers to distinguish the X-ray events from the cosmic-ray events. X-ray events are detected in one layer, while cosmic-ray events are detected in both layers simultaneously (so-called the anti-coincidence counting method). Exceptionally, events detected at the counter edge ($\phi \sim \pm 40°$) cannot be distinguished, because cosmic-rays that cause such events interact only with the upper layer.

Exposure (Effective Area $\times$ Exposure Time)

The effective area of a collimator greatly depends on the arrival direction (θ) of X-rays (Figure 3.22), while the exposure time per orbit depends on the direction (ϕ) of a source by a factor of $(\cos\phi)^{-1}$. Thus, it is important to consider the product of the effective area and the exposure time during one orbit scan. We hereafter call the product value the "exposure" (cm^2 s in unit). Figure 3.23 shows the total exposure in one orbit for a point source. This value is common between GSC-H and GSC-Z.

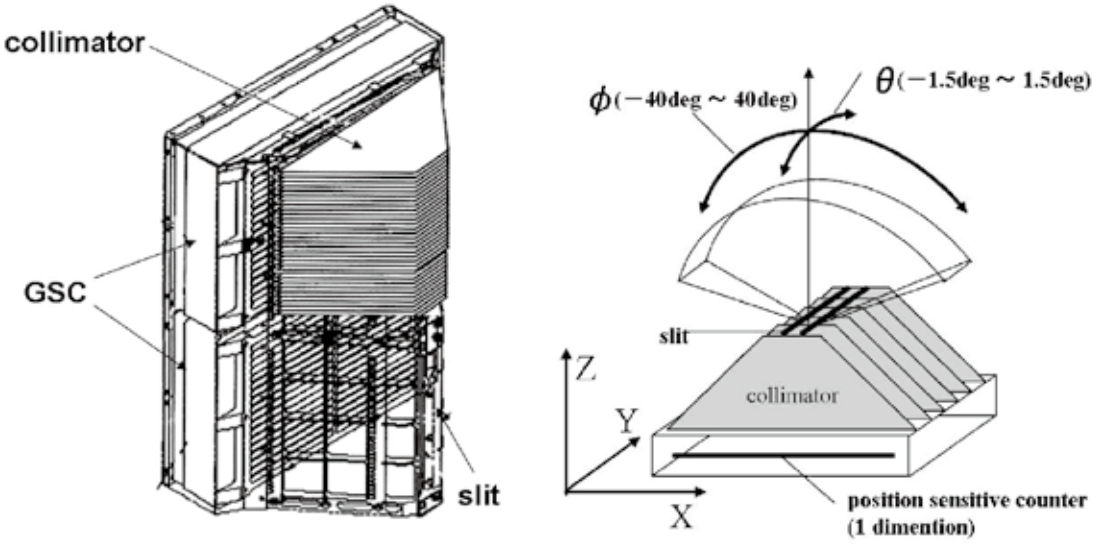

(a) (b)

Figure 3.20: Schematic view of the GSC unit and the gas proportional counter (Tsuchiya et al. 2005[168]). (a) Two counter are setted in a unit. (b) Definition of the angles θ and ϕ.

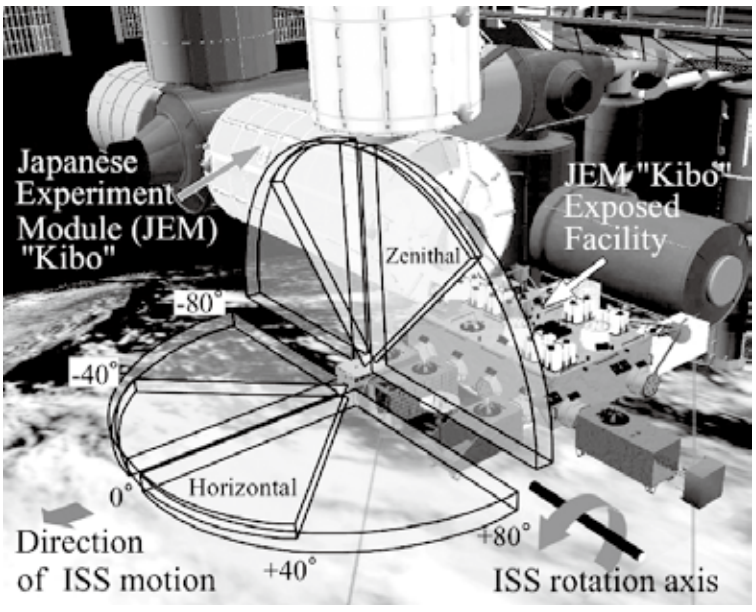

Figure 3.21: FOVs of two sets of the GSC onboard *MAXI* (Ueno et al 2009[173]).

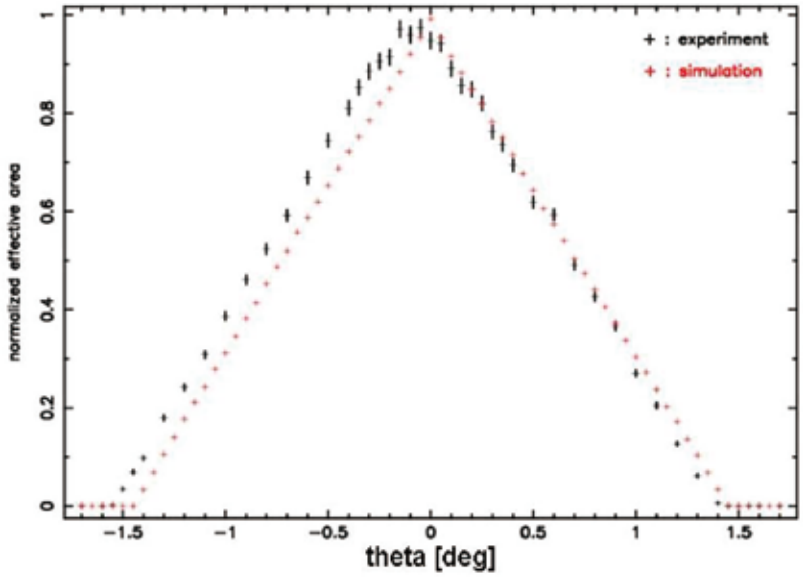

Figure 3.22: Dependence of the normalized effective area (by the value at $\theta = 0°$) in the angular response of the GSC at $\phi = 5°$ (Tsuchiya et al. 2005[168]). The black and red pluses indicate the experiment and simulation values, respectively.

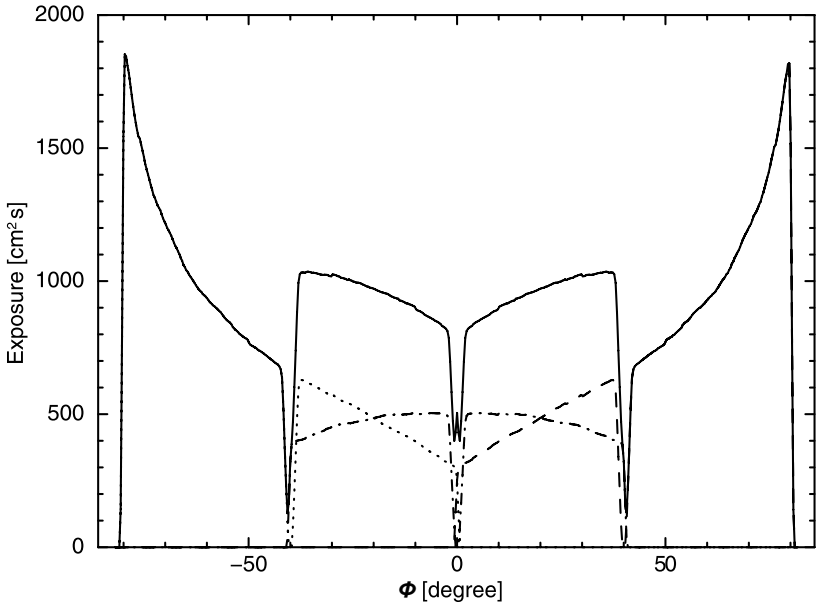

Figure 3.23: Product of the effective area and the exposure time integrated over one orbit scan for a point source for the angle ϕ (Matsuoka et al. 2009[99]). ϕ is the angle based on the central GSC unit. The solid line shows the total exposure. The dashed-dotted, dashed, and dotted lines indicate the contribution of the central, right side, and left side GSC unit only, respectively.

Point Spread Function

Although the proportional counters are one-dimensional (the slit direction) cameras, we can see a two-dimensional image, which is obtained with the triangular response of a slat collimator according to the ISS movement. An intersection of the slit image and the triangular response image corresponds to a source location in the sky as a PSF (Figure 3.24). Typical spatial resolution is about 1°.

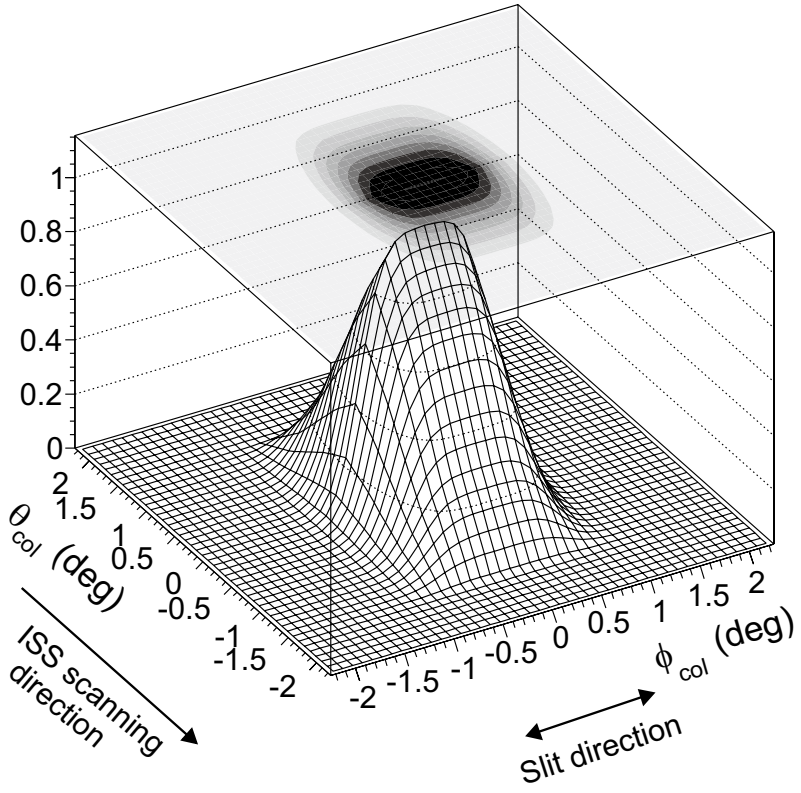

Figure 3.24: Sample of the GSC PSF (Matsuoka et al. 2009[99]). The ISS scanning direction shows a triangular response, while the slit direction shows a trapezoidal response.

Detection Efficiency

The proportional counters are filled with Xe and 1% CO_2 at 1.4 atm, and its quantum efficiiency is shown in Figure 3.25. In the 2–30 keV band, the efficiency for X-rays is above

10%. The edge at 34.6 keV is caused by Xe K-edge absorption. The counters detect incident X-ray photons from vertical to the ±40° slant direction.

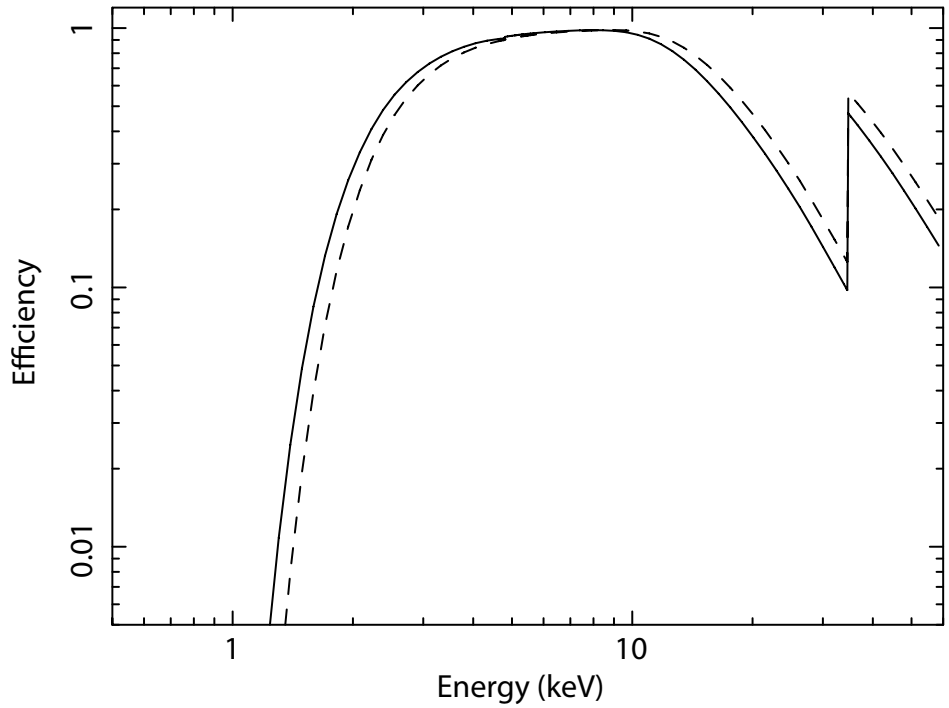

Figure 3.25: X-ray detection efficiency as a function of energy of the MAXI proportional counter (Matsuoka et al. 2009[99]). The solid line indicates the efficiency for normal-incident X-rays, while the dash line for 40° slant incident X-rays.

Chapter 4

Target Selection and Observations

In this chapter, we present the target selection of ULXs and Galactic BHBs for our study, and describe their observations and data reduction of each facility.

Contents

4.1 ULXs

4.1.1 Galaxy Selection

In order to achieve our purpose of investigating the detailed state transitions of ULXs, at least several hundred X-ray counts from a ULX are needed. Although a lot of galaxies ($\sim$200) hosting a ULX have been discovered within 40 Mpc (Liu 2008[84]), about 90% of them are too distant (>10 Mpc) to collect such X-ray counts from a ULX. We therefore focus on only galaxies within 10 Mpc in this thesis.

Among these galaxies, nearby (<5 Mpc) galaxies and interacting galaxy systems at a moderate distance (5–10 Mpc) are two suitable laboratories for our purpose. ULXs in nearby galaxies are bright in flux and can be examined in detail. About 15 ULXs were studied within 5 Mpc, which includes NGC 1313 X-1 and 2 (Mizuno et al. 2007[112]), IC 342 sources 1 and 2 (Kubota et al. 2001[75]), Holmberg II X-1 (Goad et al. 2006[57]), M 81 X-9 (Tsunoda et al. 2006[169]; Vierdayanti et al. 2010a[179]), M 82 X-1 (Miyawaki et al. 2009[110]), NGC 5204 X-1 (Roberts et al. 2006[139]), and NGC 5408 X-1 (Soria et al. 2004[153]).

In this thesis, we focus on the other laboratory; ULXs in interacting galaxy systems. They are more distant and fainter in flux than those in nearby galaxies. However, the average number of ULX per galaxy is much larger, enabling us to monitor a large number of samples at the same distance simultaneously. The number of ULXs in nine interacting systems at 20–100 Mpc (Brassington et al. 2007[16]) averages to be >6 ULXs system^{-1}.

We selected two interacting systems, namely the M 51 system and the NGC 4490 and NGC 4485 system (hereafter called NGC 4490/85), because they host the largest number of ULXs within 10 Mpc. The former at $\sim$8.4 Mpc (Feldmeier et al. 1997[40]) hosts nine, while the latter at $\sim$8 Mpc (de Vaucouleurs et al. 1976[26]) hosts eight. We listed the names and positions of the 17 ULXs in Table 4.1. Both systems have been observed several times in X-rays and thus are suitable to study long-term variations of multiple ULXs at a time. The X-ray data from these two systems had not been uniformly analyzed prior to this work (Yoshida et al. 2010[190]).

Table 4.1: ULX positions for M 51 and NGC 4490/85

M 51 [a]			NGC 4490/85 [b]		
Name	Coordinate (J2000.0)		Name	Coordinate (J2000.0)	
	R.A.	Decl.		R.A.	Decl.
Source-5	13 29 39.6	+47 12 41	ULX-1	12 30 29.5	+41 39 28
Source-9	13 29 43.4	+47 11 34	ULX-2	12 30 30.5	+41 41 42
Source-26	13 29 50.7	+47 11 53	ULX-3	12 30 30.7	+41 39 12
Source-37	13 29 53.3	+47 10 40	ULX-4	12 30 32.2	+41 39 18
Source-41	13 29 53.8	+47 14 33	ULX-5	12 30 35.2	+41 38 47
Source-63	13 29 57.6	+47 10 47	ULX-6	12 30 36.2	+41 38 38
Source-69	13 30 01.1	+47 13 41	ULX-7	12 30 38.4	+41 38 32
Source-82	13 30 07.4	+47 11 04	ULX-8	12 30 43.2	+41 38 19
Source-12	13 30 06.1	+47 15 40			

[a] The nomenclatures and positions follow Terashima & Wilson (2004)[163] and Dewangan et al. (2005)[28], respectively.
[b] The nomenclatures and positions follow Fridriksson et al. (2008)[47].

M 51

M 51 is one of the closest interacting galaxy systems, which is composed of two spiral galaxies, NGC 5194 and NGC 5195. The sizes of NGC 5194 and NGC 5195 are 27 and 14 kpc from the isophotal diameters of 11′.2 and 5′.8 (de Vaucouleurs et al. 1991[27]), respectively. The total mass of the M 51 system is $\sim 1.5 \times 10^{11}$ $M_{\odot}$ (Kuno & Nakai 1997[78]), and the mass of NGC 5194 is larger than that of NGC 5195 by a factor of a few (Schweizer 1977[143]).

Radio observations identified many H II regions (van der Hulst et al. 1988[174]), indicating that the system has an on-going star forming activity at a star formation rate of ~ 4 $M_{\odot}$ yr^{-1} (Scoville et al. 2001[145]). Two (and possibly another) core-collapse supernovae (SNe) recently occurred in the galaxy[1].

M 51 has been observed many times in X-rays by the *Einstein* (Palumbo et al. 1985[127]), *ROSAT* (Marston et al. 1995 [95]; Ehle et al. 1995[37]), *ASCA* (Terashima et al. 1998[162]; Ptak et al. 1999[132]), *BeppoSAX* (Fukazawa et al. 2001[48]), *XMM-Newton* (Dewangan et al. 2005[28]), and *Chandra* (Liu et al. 2002[82]; Terashima & Wilson 2004[163]) observato-

[1] See http://web.oapd.inaf.it/supern/cat/ for detail.

ries. The number of X-ray sources increased from three by *Einstein* (Palumbo et al. 1985[127]) to 113 by *Chandra* (Terashima & Wilson 2004[163]), which includes nine ULXs (Dewangan et al. 2005[28]). We follow the nomenclature by Terashima & Wilson (2004)[163]. Figure 4.1 (a) shows positions of the ULXs on the optical image by the Sloan Digital Sky Survey (SDSS) data. All ULXs are distributed along galactic arms. Terashima et al. (2006)[164] reported using the *Hubble Space Telescope* data that four ULXs (sources-9, 37, 69, and 82) are located near the center or at the rim of star clusters. They also identified one or more optical counterparts to six ULXs.

NGC 4490/85

NGC 4490 and NGC 4485, the former being a spiral and the latter being an irregular galaxy, are interacting with each other. NGC 4490/85 is one of the closest interacting galaxies as well as M 51, belonging to the CVn II group of galaxies (de Vaucouleurs et al. 1976[26]; Viallefond et al. 1980[177]; Clemens et al. 1998[22]; Clemens et al. 1999[23]; Fridriksson et al. 2008[47]). The size and the mass of NGC 4490 are $\sim$15 kpc (Clemens & Alexander 2002[24]) and $\sim 1.6\times10^{10}\ M_\odot$ (Viallefond et al. 1980[177]), respectively, while those of NGC 4485 are $\sim$5.6 kpc (Clemens & Alexander 2002[24]) and $\sim 2\times10^{9}\ M_\odot$ (Clemens et al. 1999[23]), respectively.

Radio observations identified many H II regions in NGC 4490, indicating an on-going star forming activity at a star formation rate of $\sim$4.7 $M_\odot$ yr^{-1} (Clemens et al. 1999[23]; Clemens & Alexander 2002[24]). Two core-collapse SNe recently occurred in the galaxy[2].

NGC 4490/85 was observed several times with the *ROSAT* (Read et al. 1997[134]; Roberts & Warwick 2000[137]), *XMM-Newton*, and *Chandra* observatories (Roberts et al. 2002[138]; Fridriksson et al. 2008[47]). The number of known X-ray sources increased from five by *ROSAT* (Roberts & Warwick 2000[137]) to 38 by *Chandra* (Fridriksson et al. 2008[47]), which include eight ULXs (ULX-1 to ULX-8). We follow the nomenclature by Fridriksson et al. (2008)[47]. Figure 4.2 (a) shows positions of the ULXs on the SDSS image. ULX-2 belongs to NGC 4485, while the others to NGC 4490. ULX-6 is close to but offset from the dynamical center of the galaxy (Roberts et al. 2002[138]), and the other ULXs in NGC 4490 are distributed along galactic arms. Six of them were observed by the *Spitzer Space Telescope*. Five sources (ULX-2, 3, 4, 6, and 8) are likely to be an accreting X-ray source based on the detection of some characteristic features of highly ionized species in the mid-infrared

[2]See http://web.oapd.inaf.it/supern/cat/ for detail.

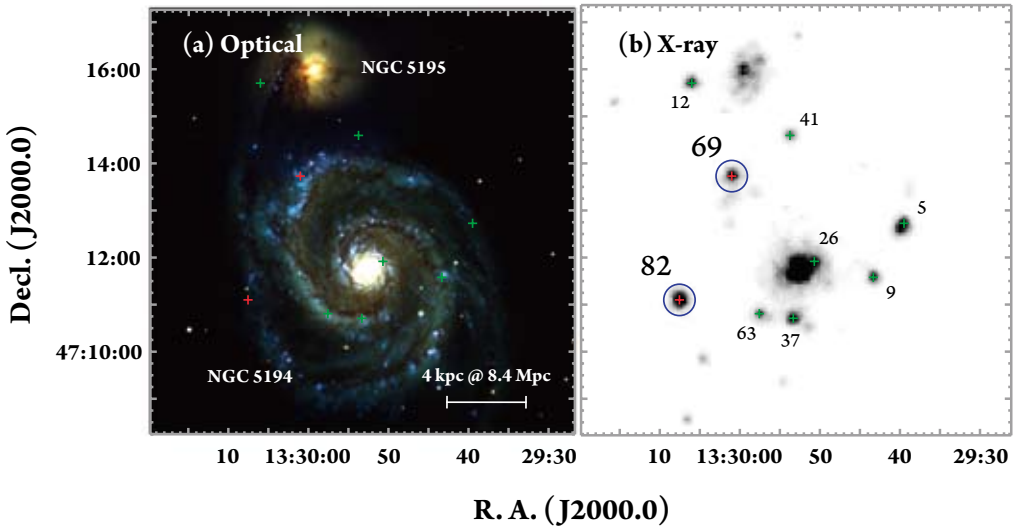

Figure 4.1: Optical and X-ray images of M 51. (a) SDSS three color image. Red, green, and blue respectively represents the *r*-, *g*-, and *u*-band intensity. Pluses show positions of the nine ULXs in Dewangan et al. (2005)[28]; the two brightest sources, focused in this study, are shown in red and the remainders are in green. (b) Smoothed *XMM-Newton* MOS-1 image in the 0.5–8.0 keV band. Solid blue circles indicate the source extraction region.

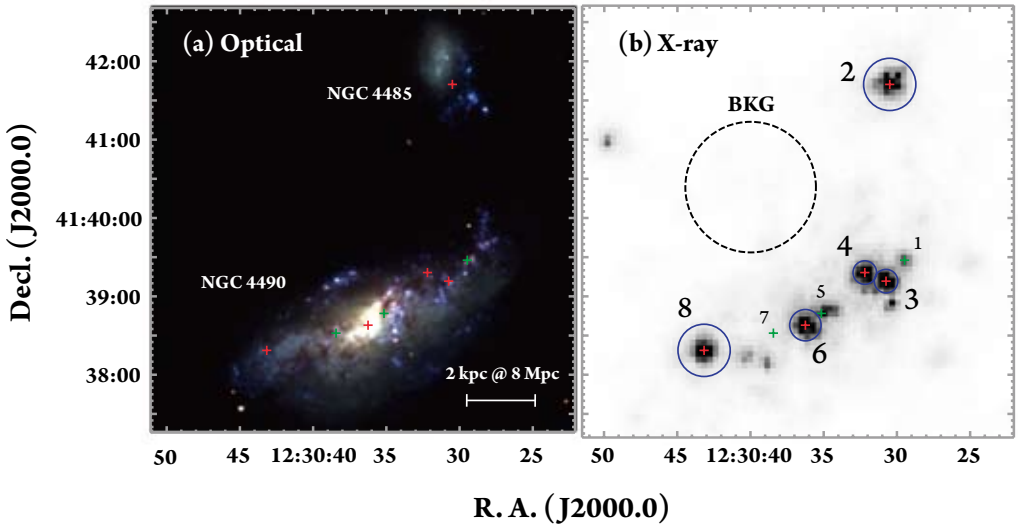

Figure 4.2: Same with Figure 4.1, but for NGC 4490/85. Pluses show positions of the eight ULXs in Fridriksson et al. (2008)[47]. The dashed circle in (b) indicates the common background region.

spectra, while the remaining one (ULX-1) is more likely to be an SN remnant (Vázquez et al. 2007[176]). Nevertheless, X-ray flux variation was found from ULX-1 (Fridriksson et al. 2008[47]), leading to the speculation that this source is a ULX associated with the SN remnant.

Previous X-ray studies (Roberts et al. 2002[138]; Fridriksson et al. 2008[47]) presented long-term variations in flux and color in several ULXs and conducted some phenomenological spectral analysis. We present long-term spectral variations of all the bright ULXs absed on more physical models.

4.1.2 Observations

M 51 and NGC 4490/85 were respectively observed five and three times by *Chandra*, seven times and once by *XMM-Newton*. Among them, we selected data sets with an exposure time longer than 10 ks for detailed spectral analysis. The observational information (observation ID, date, and exposure time) of the selected data sets are shown in Table 4.2. All the *Chandra* data sets were taken with the full frame mode with the aim point in the S3 chip. The chip contains the entire system of both M 51 and NGC 4490/85. The instruments of *XMM-Newton* (MOS-1, 2, and pn) also cover the two studied systems entirely (Figures 4.1b and 4.2b). Throughout this thesis, we use X-ray events in the 0.5–8.0 keV energy band.

For M 51, we analyzed three *Chandra* and four *XMM-Newton* archived data sets. We labeled the observations as C1–3 and X1–4, respectively (Table 4.2). In the *XMM-Newton* observations, the thin (X1, X3, and X4) and medium (X2) filters were used. All cameras were operated with the full frame mode. Previously published X-ray studies (Liu et al. 2002[82]; Terashima & Wilson 2004[163]; Dewangan et al. 2005[28]; Terashima et al. 2006[164]) were based on four X-ray data sets (C1, C2, C3, and X1) among seven. We reduce all the available data including three unpublished sets.

For NGC 4490/85, we reduced all the archived data sets of *Chandra* and *XMM-Newton*. The sets are the same with those used in Fridriksson et al. (2008)[47] and Gladstone & Roberts (2009)[55]. We labeled the *Chandra* and the *XMM-Newton* observations as C1′–3′ and X1′, respectively (Table 4.2). In the *XMM-Newton* observation (X1′), the medium filter was used. The two MOS and pn cameras were operated with the full frame mode and the extended full frame mode, respectively.

Table 4.2: Observation log for selected galaxy systems

Data label	Observatory	ObsID	Date	$t_{\rm exp}$ [a] (ks)
M 51				
C1	*Chandra*	354	2000-06-20	14.9
C2		1622	2001-06-23	26.8
C3		3932	2003-08-07	48.0
X1	*XMM-Newton*	0112840201	2003-01-15	20.7/19.0
X2		0212480801	2005-07-01	49.0/47.3
X3		0303420101	2006-05-20	52.5/52.2
X4		0303420201	2006-05-24	36.6/34.9
NGC 4490/85				
C1′	*Chandra*	1579	2000-11-03	19.5
C2′		4725	2004-07-29	38.5
C3′		4726	2004-11-20	39.6
X1′	*XMM-Newton*	0112280201	2002-05-27	17.4/11.9

[a] ACIS exposure for the *Chandra* observations and EPIC MOS (left) and EPIC pn (right) exposure for the *XMM-Newton* observations.

4.1.3 Data Reduction

Chandra

Using the *Chandra* Interactive Analysis of Observations (CIAO) version 4.0 and the ACIS Extract package (Broos et al. 2002[17]) version 2008-06-06, we extracted the source and background events and constructed the energy spectra. We adopted the ULX positions based on Table 4.1: i.e., Dewangan et al. (2005)[28] for M 51, and Fridriksson et al. (2008)[47] for NGC 4490/85. The source events were accumulated from a region around each source encircling 90% of photons of a point-like source. The background events were from an annulus around each source.

We list the number of counts for the ULXs identified in M 51 (Dewangan et al. 2005[28]) and NGC 4490/85 (Fridriksson et al. 2008[47]) in Tables 4.3 and 4.4, respectively. Among all the ULXs, we focus on the sources with a total count of more than 1000 at least in one observation, which are practically bright enough for our spectral analysis. Seven sources are thus selected; sources-69 and 82 for M 51, and ULX-2, 3, 4, 6, and 8 for NGC 4490/85.

XMM-Newton

We used the Science Analysis System (SAS) version 7.1.0 for extracting events and generating response files. Some high background time intervals were seen in all observations. For three observations (M 51 X2, X3, and X4), we excluded intervals with count rates larger than the average by more than 3σ. For the remaining observations, we used all exposures because the effect is negligible with only a few counts in extracted source counts.

We focus on the seven sources selected in the *Chandra* data (Tables 4.3 and 4.4). The source extraction regions are shown in Figures 4.1 (b) and 4.2 (b). We chose the source region with a radius of 9–20″ to avoid contamination from other sources. In M 51, the background regions were extracted from an annulus around each source to offset the global diffuse emission. In contrast, in NGC 4490/85, a common background region devoid of bright sources (Figure 4.2b) was adopted. The background events have ∼100 counts for MOS and ∼300 counts for pn.

Table 4.3: Source and background counts for M 51

Name [a]	Counts [b]					
	Chandra					
	C1	C2	C3			
Source-5	213 (0.1)	163 (0.2)	397 (1.3)			
Source-9	121 (0.1)	195 (0.2)	696 (1.2)			
Source-26	92 (0.8)	229 (1.3)	375 (3.2)			
Source-37	2 (0.2)	497 (0.3)	3 (0.5)			
Source-41	196 (0.3)	352 (0.5)	554 (2.3)			
Source-63	105 (0.2)	245 (0.3)	184 (0.6)			
Source-69	463 (0.9)	42 (1.2)	1698 (3.6)			
Source-82	757 (0.3)	778 (0.5)	1791 (0.9)			
Source-12	191 (1.1)	332 (2.3)	466 (6.0)			
	XMM-Newton					
	X1			X2		
	MOS-1	MOS-2	pn	MOS-1	MOS-2	pn
Source-5	321 (59)	352 (44)	917 (102)	392 (62)	441 (60)	850 (63)
Source-9	182 (71)	172 (79)	227 (143)	281 (75)	328 (102)	862 (246)
Source-26	349 (410)	456 (374)	1148 (1212)	520 (512)	535 (433)	1271 (1151)
Source-37	263 (97)	141 (87)	283 (244)	344 (139)	431 (148)	947 (326)
Source-41	137 (35)	129 (44)	384 (121)	254 (49)	245 (62)	576 (163)
Source-63	187 (81)	222 (78)	448 (217)	227 (123)	262 (138)	411 (234)
Source-69	302 (97)	309 (107)	813 (329)	1137 (152)	1258 (200)	2679 (401)
Source-82	513 (76)	514 (51)	465 (95)	561 (74)	603 (87)	... [c]
Source-12	195 (37)	178 (24)	462 (114)	176 (101)	121 (82)	321 (126)
	XMM-Newton					
	X3			X4		
	MOS-1	MOS-2	pn	MOS-1	MOS-2	pn
Source-5	509 (101)	466 (101)	411 (88)	536 (79)	514 (97)	451 (94)
Source-9	117 (119)	130 (157)	... [c]	187 (81)	205 (89)	617 (236)
Source-26	607 (668)	668 (596)	... [c]	420 (496)	474 (441)	376 (757)
Source-37	277 (162)	265 (160)	... [c]	113 (113)	108 (124)	275 (252)
Source-41	319 (95)	265 (82)	691 (167)	212 (43)	229 (57)	593 (110)
Source-63	233 (141)	217 (138)	476 (193)	162 (88)	170 (101)	366 (207)
Source-69	1114 (164)	1306 (237)	2887 (647)	1067 (173)	1209 (207)	2864 (561)
Source-82	653 (87)	577 (107)	1448 (225)	461 (70)	458 (78)	1236 (194)
Source-12	157 (67)	129 (66)	374 (118)	118 (50)	130 (38)	146 (91)

[a] The two brightest ULXs, focused in this thesis, are shown in the bold font.

[b] Source counts (background counts). The background counts are normalized to the source extraction area.

[c] The data are unavailable, because the source is located in a gap or a dead area of a chip.

Table 4.4: Source and background counts for NGC 4490/85

Name [a]	Counts [b]					
	Chandra			*XMM-Newton*		
	C1′	C2′	C3′	X1′		
				MOS-1	MOS-2	pn
ULX-1	239 (0.2)	424 (1.1)	305 (0.7)	···	···	···
ULX-2	1243 (0.8)	1772 (9.9)	1436 (0.9)	609 (23.5)	499 (21.0)	403 (50.2)
ULX-3	566 (0.3)	1148 (1.2)	1209 (1.0)	339 (4.8)	309 (4.2)	554 (10.2)
ULX-4	455 (0.4)	1291 (1.9)	1375 (1.3)	365 (4.8)	419 (4.2)	775 (10.2)
ULX-5	30 (0.8)	374 (1.7)	561 (1.5)	···	···	···
ULX-6	473 (0.8)	299 (1.9)	1347 (2.3)	444 (8.5)	481 (7.5)	897 (18.1)
ULX-7	0 (0.3)	1 (0.7)	749 (0.9)	···	···	···
ULX-8	780 (0.4)	1333 (1.2)	1762 (1.4)	525 (23.5)	484 (21.0)	811 (50.2)

[a] The five brightest ULXs, focused in this thesis, are shown in the bold font.
[b] Same with Table 4.3.

4.2 Galactic BHBs

4.2.1 BHB Selection

In the Local Group, 40–50 stellar mass BHB candidates have been reported so far; see McClintock & Remillard (2006)[103], Ziółkowski (2003)[195] for a review. In this thesis, we consider that the number of BHB candidates is 44. These sources satisfy either or both of the following two criteria: (i) It is listed as a BHB candidate on either of the above two reviews. (ii) The estimated mass of the compact object is larger than 3.2 $M_{\odot}$, because such a large mass cannot be explained without a BH.

Data for all the BHB candidates are available by *MAXI*, but heavily confused sources need to be removed. Therefore we selected the candidates as follows: a source is selected if a source occupies more than 90% of the flux within 2° radius. Here, we used the X-ray source catalog (Tueller et al. 2010[170]) made by the Burst Alert Telescope (Barthelmy et al. 2005[9]) onboard the *Swift* satellite, which is a wide field coded-mask detector with a sensitivity in the hard X-ray band (14–195 keV). Consequently, 30 BHB candidates were selected. Their basic information (conventional name, coordinate, BH mass, distance from us, and the hydrogen column density) are shown in Table 4.5 in the order of R.A.. Hereafter, we call these BHB candidates "BHBs".

4.2.2 Observations

MAXI was launched on 2009 July 16, and started operation on 2009 August 03. The generated data format changed on 2009 October 30. Due to software compatibility, we only used data after the change. Our data set covers from 2009 October 30 (MJD = 55134) to 2010 August 31 (MJD = 55439), namely 306 days in total, for all the BHBs. Throughout this thesis, we use X-ray events in the 2–20 keV band for *MAXI*/GSC.

The GSC contains 12 proportional counters (see § 3.3.2), but four of them stopped operation on 2009 September 22 due to unexpected discharge events. We thus use only the remaining eight counters in our study.

Table 4.5: Basic information for selected BHBs

Name	Coordinate (J2000.0) [a]		$M_{\rm BH}$ [b]	Distance [c]	$N_{\rm H}$ [c]
	R.A.	Decl.	($M_\odot$)	(kpc)	(10^{21} cm^{-2})
GRO J0422+32	04 21 42.8	+32 54 27	3.7–5.0	2.5±0.3[52]	2.0[149]
LMC X-3	05 38 56.6	−64 05 03	5.9–9.2	52±0.6[29]	0.4±0.1[126]
LMC X-1	05 39 38.8	−69 44 36	4.0–10.0	52±0.6[29]	10[59]
A 0620−00	06 22 44.5	−00 20 45	8.7–12.9	1±0.4[146]	2[50]
GRS 1009−45	10 13 36.3	−45 04 31	3.6–4.7	5.0±1.3[103]	$1.4^{+0.6}_{-0.4}$[74]
XTE J1118+480	11 18 10.8	+48 02 13	6.5–7.2	1.8±0.6[102]	$0.3^{+0.2}_{-0.1}$[32]
GRS 1124−68	11 26 26.6	−68 40 32	6.5–8.2	5.5±1.0[122]	5[35]
GS 1354−64	13 58 09.9	−64 44 05	10.0±2.0	33± 6[20]	32[50]
A 1524−62	15 28 17.2	−61 52 58	—	4.4[175]	3[8]
4U 1543−47	15 47 08.6	−47 40 10	8.4–10.4	9.1±1.1[123]	3.5[123]
XTE J1550−564	15 50 58.7	−56 28 36	8.4–10.8	5.3±2.3[125]	9[166]
4U 1630−47	16 34 00.4	−47 23 39	—	10*[7]	50–120
XTE J1650−500	16 50 01.0	−49 57 45	6±3	2.6±0.7[63]	6.7±0.5[167]
GRO J1655−40	16 54 00.1	−39 50 45	6.0–6.6	3.2±0.2[62]	<1000[172]
GX 339−4	17 02 49.4	−48 47 23	5.8±0.5	8* (≥7)[193]	5* (4.5–5.8[18])
GRO J1719−24	17 19 36.9	−25 01 03	>4.9[96]	2.4±0.4[81]	4[50]
H 1743−322	17 46 15.6	−32 14 01	—	8*[189]	25^{+43}_{-25}[128]
XTE J1752−223	17 52 15.1	−22 20 34	8.6–32[115]	5* (2–8[114])	$7.2^{+0.1}_{-0.4}$[114]
Swift J1753.5−0127	17 53 28.3	−01 27 09	≲12[196]	8*[152]	1.7[61]
4U 1755−33	17 58 40.0	−33 48 27	—	6.5* (4–9[182])	2[69]
SAX J1819.3−2525	18 19 21.6	−25 24 26	6.8–7.4	$9.6^{+2.7}_{-2.2}$[124]	3[103]
XTE J1859+226	18 58 41.6	+22 39 29	7.6–12.0	6.3±1.7[64]	3[50]
SS 433	19 11 49.6	+04 58 58	1.9–4.9[77]	5.5±0.2[14]	>100[44]
GRS 1915+105	19 15 11.6	+10 56 44	10.0–18.0	11[41]	20–60[12]
Cyg X-1	19 58 21.7	+35 12 06	6.8–13.3	2.5±0.4[94]	$6.6^{+0.8}_{-0.3}$[91]
4U 1957+11	19 59 24.2	+11 42 32	—	20* (≥20[141])	0.1[118]
GS 2000+25	20 02 49.6	+25 14 11	7.1–7.8	2.7±0.7[60]	3[161]
XTE J2012+81	20 12 37.8	+38 11 01	—	10*[19]	12.7±0.2[19]
GS 2023+338	20 24 03.8	+33 52 02	10.1–13.4	2.39±0.14[106]	8* (7–9[15])
Cyg X-3	20 32 25.8	+40 57 28	10.1±3.2[150]	9^{+4}_{-2}[129]	110–160[181]

[a] Coordinates recognized by the SIMBAD Astronomical Database (http://simbad.u-strasbg.fr/simbad/), except for XTE J1752−223 (by Markwardt et al. 2009[93]).

[b] BH masses without a reference are referred by McClintock & Remillard (2006)[103], Dunn et al. (2010)[33], and references therein.

[c] Numbers with an asterisk indicate an assumed value.

4.2.3 Data Reduction

We processed many GSC data sets (306 days × 15 orbits/day × eight counters) by using the Maxitool vertion 3.4.2d, the Maxiutil vertion 1.8.2a, and the GSC Software vertion 0.97.1a. The data sets were reduced separately for each GSC counter because the exposure of each counter is different (see Figure 3.23 in § 3.3.2). First, in order to obtain enough photon statistics, we integrated the data sets for each day (the total number of the data sets change to 306 days × eight counters). Next, we extracted the source and background events. We chose the source region with a radius of 1°–1.5° depending on the level of contamination from other sources. The background regions were extracted from an annulus around each source with an inner and outer radius of 1°–1.5° and 4°, respectively. When other sources exist within 5.5°, their regions with a radius of 1.5° were excluded from the background region. The total number of the extracted source event data is 30 BHBs × 306 days × eight counters.

We further screened events by removing low quality data. We executed the following two tests for the extracted source and background event data, and selected only the high quality ones. After these tests, we combined the selected event data for all the counters in each day (the maximum number of the event data would be 30 BHBs × 306 days). (i) We exclude data that include events detected at the counter edges (the slant angle $\phi > |38°|$). This is because such events cannot be distinguished between X-ray events and cosmic-ray events (see § 3.3.2). (ii) Data with a small exposure (cm^2 s in unit) are also excluded. Exposures were considered too small if they were smaller than the average by more than 3σ.

For the final data sets, we listed the number of useful days, the total exposure time, and the background-subtracted source counts of each BHB in Table 4.6. The average number of days is 220.6. We also summarized the light curves of all the BHBs in Figures 4.3 and 4.4.

Table 4.6: Observation log and source counts for BHBs

Name	Number of days	$t_{\rm exp}$ [a] (ks)	Counts [b, c]
GRO J0422+32	188	246	815 (1.4%)
LMC X-3	270	324	41623 (44.2%)
LMC X-1	266	371	42667 (39.1%)
A 0620−00	232	234	677 (1.3%)
GRS 1009−45	214	216	2197 (4.1%)
XTE J1118+480	166	164	993 (2.7%)
GRS 1124−68	269	464	668 (0.7%)
GS 1354−64	261	444	3724 (3.5%)
A 1524−62	248	258	3112 (6.9%)
4U 1543−47	189	121	2064 (9.4%)
XTE J1550−564	235	190	3015 (8.5%)
4U 1630−47	195	131	59428 (71.6%)
XTE J1650−500	211	145	4295 (13.1%)
GRO J1655−40	205	115	2705 (12.9%)
GX 339−4	215	195	156265 (76.2%)
GRO J1719−24	212	144	1531 (6.2%)
H 1743−322	201	178	39128 (44.9%)
XTE J1752−223	206	152	88695 (72.8%)
Swift J1753.5−0127	214	209	52471 (53.5%)
4U 1755−33	204	177	2298 (4.8%)
SAX J1819.3−2525	203	174	−2259 (−5.2%)
XTE J1859+226	205	214	1124 (2.4%)
SS 433	202	173	8367 (19.8%)
GRS 1915+105	199	212	860191 (94.3%)
Cyg X-1	191	238	463590 (89.0%)
4U 1957+11	209	216	27140 (36.8%)
GS 2000+25	193	220	663 (1.3%)
XTE J2012+81	183	204	−2488 (−5.2%)
GS 2023+338	194	230	−198 (−0.4%)
Cyg X-3	190	208	155034 (76.7%)

[a] Total exposure time for *MAXI*/GSC observations.

[b] Total background-subtracted source counts. The parenthetic number indicates the ratio of the background-subtracted source count to the non-background-subtracted source count.

[c] Negative number indicates that the background count is larger than the non-background-subtracted source count.

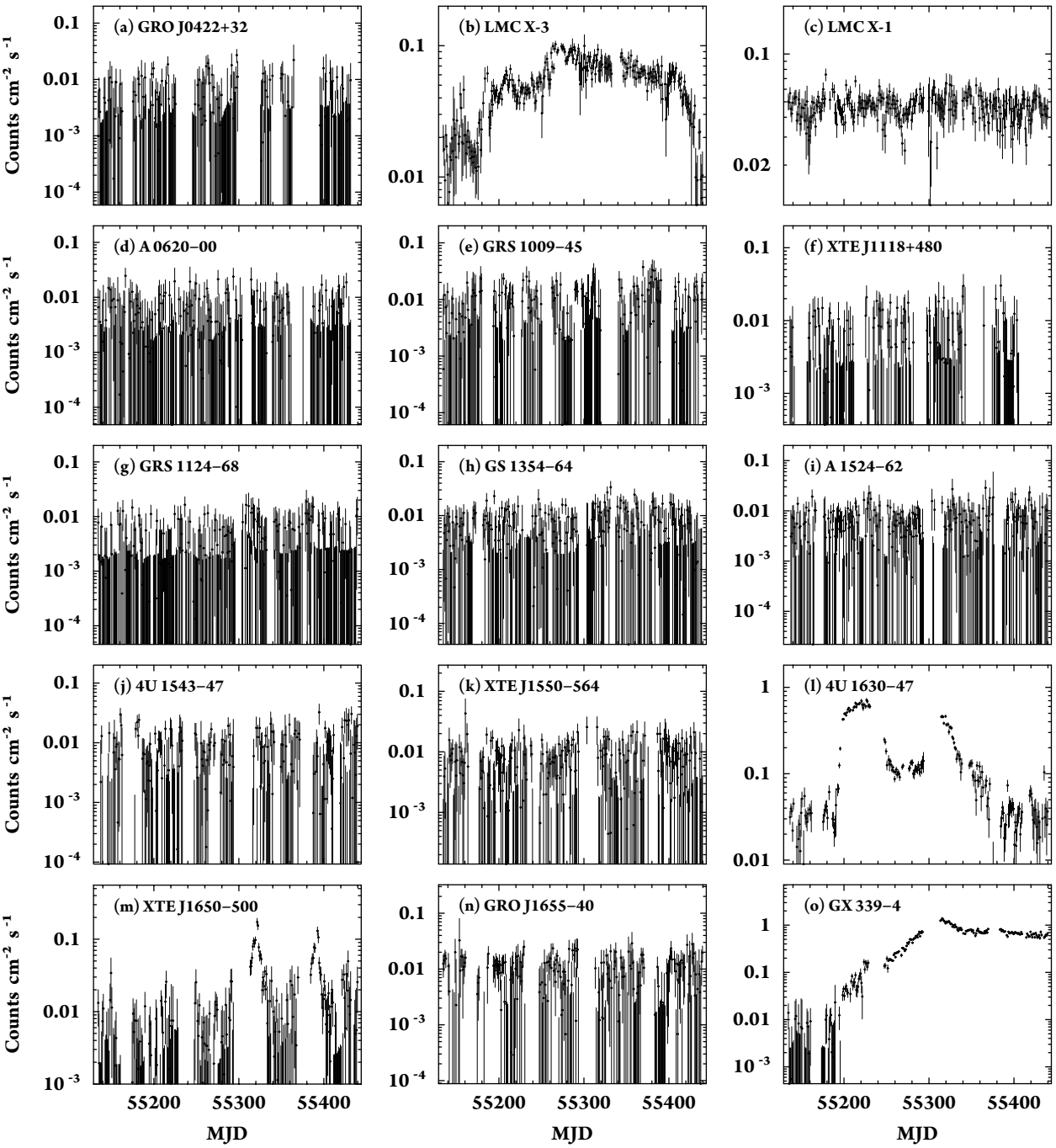

Figure 4.3: *MAXI*/GSC background-subtracted light curves of the BHBs in 2–20 keV. Black pluses indicate one day flux (counts cm^{-2} s^{-1} in unit).

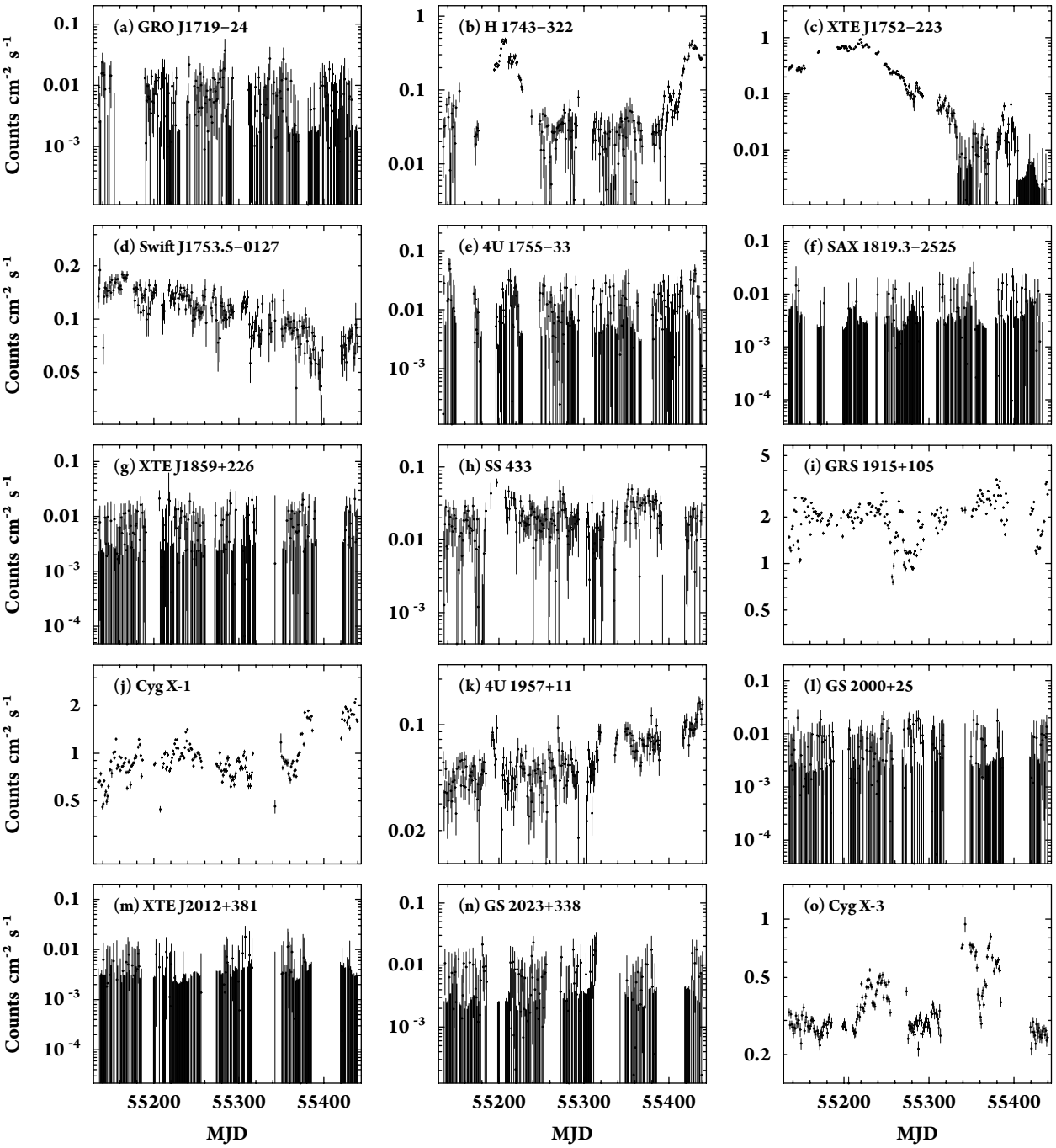

Figure 4.4: Continued from Figure 4.3.

Chapter 5

Data Analysis and Results

In this chapter, we present the timing and spectral analyses and results for the selected ULXs (§ 5.1) and Galactic BHBs (§ 5.2).

Contents

5.1 ULXs

Hereafter, we call each exposure of a source as a "sample" for the ULXs. The total number of the samples is 34, since there are two sources with seven exposures for M 51 and five sources with four exposures for NGC 4490/85.

5.1.1 Light Curves

Using the X-ray timing analysis package XRONOS version 5.2.1, we created the background-subtracted light curves of the seven ULXs. We binned the curves with 1000 s bin^{-1}. In order to examine short-term X-ray variations of each sample, we fitted them with a constant flux model. For the *XMM-Newton* observations, we considered that the flux is variable when neither of the MOS and pn light curves are fitted with a constant model.

The null hypothesis probabilities derived by the fitting are summarized in Table 5.1. We found significant variations (5% significance level) only from one source (M 51 source-69). This source showed a significant short-term variation in most samples (C1, X1, X2, X3, and X4). We confirmed the periodicity of ∼7000 s in the flux in C1 as was reported by Liu et al. (2002)[82].

Swartz et al. (2004)[157] found that 5–15% of 154 ULXs (including candidates) are variable sources by using *Chandra* in the 0.5–8.0 keV band. Our result (one among seven ∼ 14%) is consistent with their statistical study.

5.1.2 Spectra

Figure 5.1 shows the background-subtracted spectra of several samples. All were binned with at least 20 counts bin^{-1}. All spectra are featureless. Some sources show flux variation among different observations.

Fitting Models

We used the X-ray spectral fitting package XSPEC version 11.3.2 for the spectral analysis. For the interstellar extinction, we used the `wabs` model (Morrison & McCammon 1983[113])

Table 5.1: Result of light curve fitting

M 51			NGC 4490/85					
Name	Data label	N.H.P. [a] (%)	Name	Data label	N.H.P. [a] (%)	Name	Data label	N.H.P. [a] (%)
Source-69	C1	<1	ULX-2	C1′	98	ULX-6	C1′	99
	C2	>99		C2′	>99		C2′	>99
	C3	96		C3′	>99		C3′	>99
	X1	18/2		X1′	93/88		X1′	78/33
	X2	64/<1	ULX-3	C1′	>99	ULX-8	C1′	96
	X3	12/<1		C2′	>99		C2′	98
	X4	<1/<1		C3′	93		C3′	93
Source-82	C1	94		X1′	>99/36		X1′	91/18
	C2	99	ULX-4	C1′	>99			
	C3	>99		C2′	92			
	X1	91/88		C3′	96			
	X2	55/94		X1′	99/70			
	X3	75/59						
	X4	41/32						

[a] Null hypothesis probability for ACIS of *Chandra* and EPIC MOS (*left*) and EPIC pn (*right*) of *XMM-Newton*.

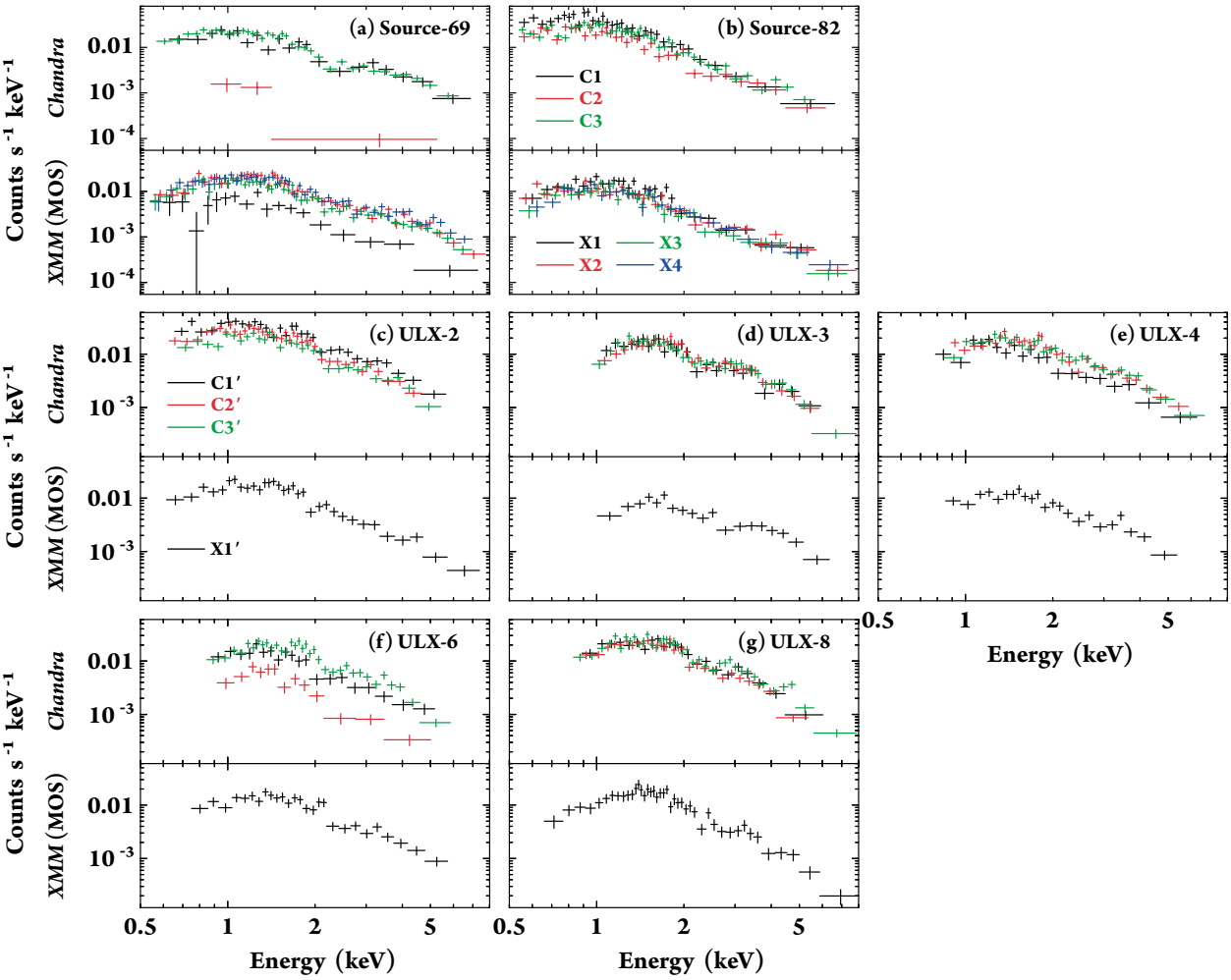

Figure 5.1: Time-averaged spectra of the seven ULXs. The top panels show the *Chandra* ACIS-S3 spectra by the three observations; C1, C1′ (*black*), C2, C2′ (*red*), and C3, C3′ (*green*). The bottom panels show the *XMM-Newton* merged MOS spectra by the four (M 51) or one (NGC 4490/85) observations; X1, X1′ (*black*), X2 (*red*), X3 (*green*), and X4 (*blue*).

with an abundance by Anders & Ebihara (1982)[5]. For the hydrogen column densities, we assumed the fixed Galactic extinction of 1.57×10^{20} cm^{-2} for M 51 or 1.78×10^{20} cm^{-2} for NGC 4490/85 (Dickey & Lockman 1990[30]) and a thawed additional extinction for each source. For the *XMM-Newton* EPIC data, we fitted the merged MOS and pn spectra simultaneously.

We first applied a PL model and an MCD model (`diskbb` in XSPEC; Mitsuda et al. 1984[107]), which are commonly used to fit the continuum emission of Galactic BHBs and ULXs. As described in § 2.4.2, the MCD model has the innermost disk temperature $T_{\rm in}$ as one of the parameters. Using the equation (2.22) — $L_{\rm bol} = 4\pi(R_{\rm in}/\xi)^2\sigma(T_{\rm in}/\kappa)^4$, we can calculate the innermost disk radius $R_{\rm in}$ (Makishima et al. 2000[90]). For non-spinning BHs, the BH mass $M_{\rm BH}$ can be estimated from $R_{\rm in}$ using the relation $R_{\rm in} = 8.86(M_{\rm BH}/M_\odot)$ km (Makishima et al. 2000[90]). For the MCD model with $kT_{\rm in} = 0.7$–2.0 keV, the 0.5–8.0 keV band contains >80% of the entire spectrum, thus we approximate the X-ray luminosity in this band as the bolometric luminosity.

We also fitted all the spectra with a slim disk model by Kawaguchi (2003)[71][1]. The "Kawaguchi model" takes into account the Comptonization and the relativistic effects, and contains the BH mass and mass accretion rate as model parameters. We fixed the viscous parameter α to be 0.1 (Vierdayanti et al. 2006[178]). This model was successfully applied to some bright ULXs, including M 33 X-8 (Foschini et al. 2006[45]), NGC 1313 X-2, NGC 4559 X-7, X-10, NGC 5204 X-1 (Vierdayanti et al. 2006[178]), and M 82 X-1 (Okajima et al. 2006[121]).

Fitting Results

We summarize all the best-fit parameters in Tables 5.2 and 5.3 for samples in M 51 and NGC 4490/85, respectively. $N'_{\rm H}$, Γ, and dM/dt indicate the absorption column density additional to that in our Galaxy, the photon index, and the mass accretion rate, respectively. Using the absorption-corrected flux ($f'_{\rm X,PL}$, $f'_{\rm X,MCD}$, and $f'_{\rm X,Kaw}$ respectively for the PL, MCD, and Kawaguchi models), the luminosity is calculated as $L_{\rm X,PL} = 4\pi D^2 f'_{\rm X,PL}$, $L_{\rm X,MCD} = 2\pi D^2 f'_{\rm X,MCD}(\cos i)^{-1}$, and $L_{\rm X,Kaw} = 2\pi D^2 f'_{\rm X,Kaw}(\cos i)^{-1}$. Here, D is the distance to each galaxy, and i is the inclination of the disk. We assumed isotropic emission for the PL, and a moderate inclination for the MCD and Kawaguchi models ($i = 45°$). Errors of all the parameters are calculated at a 90% confidence level. Figure 5.2 shows examples of the

[1]See http://heasarc.nasa.gov/xanadu/xspec/models/slimdisk.html for detail.

spectra and the best-fit models.

Although short-term flux and spectral hardness variations are found in M 51 source-69 in C1, we averaged each exposure because the paucity of the counts do not allow us to conduct time-sliced spectroscopy. This source was very faint in C2, thus $N'_{\rm H}$ is fixed at 6.0×10^{20} cm^{-1}, which is the median value obtained from the other six observations.

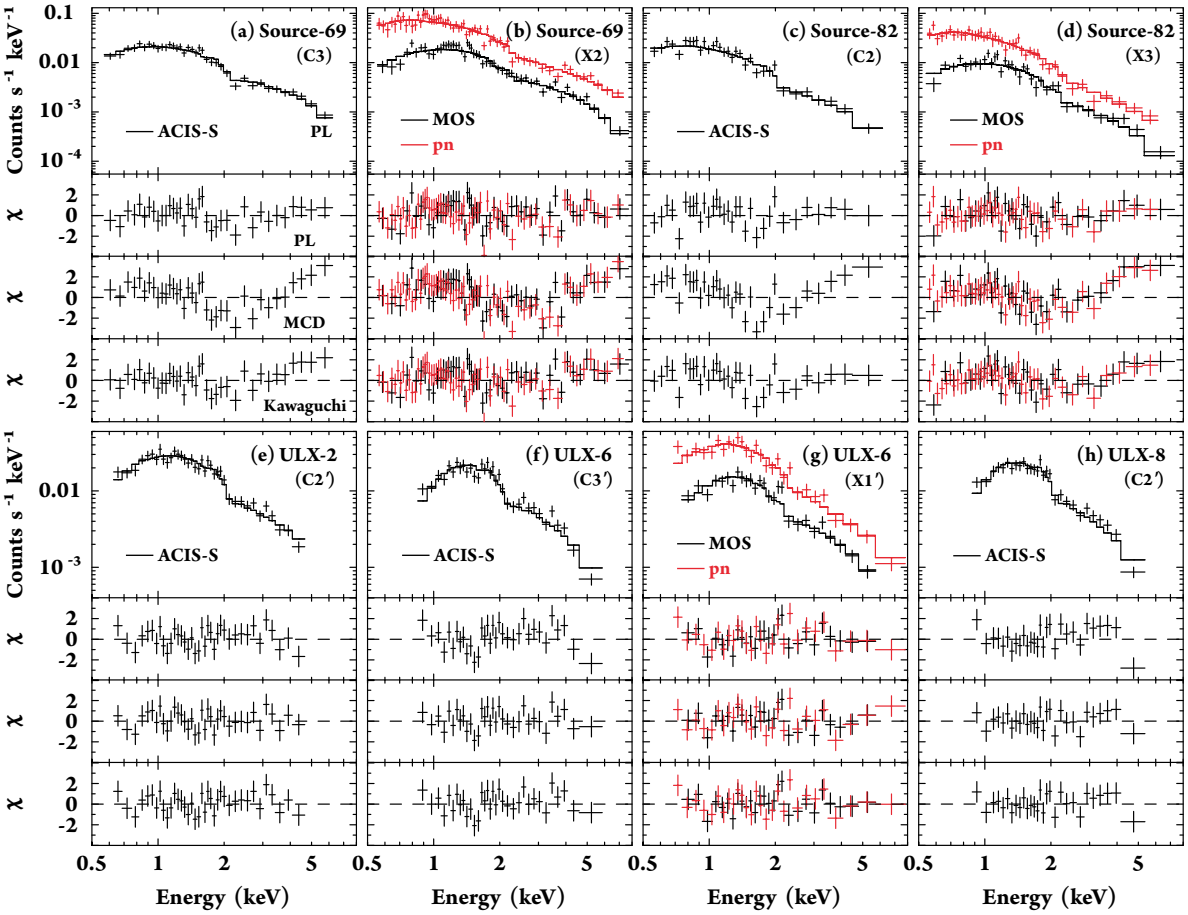

Figure 5.2: Examples of spectral fitting in M 51 (a–d) and NGC 4490/85 (e–h). Spectra are shown for different sources with different instruments as indicated by the labels and colors. The top panels show the spectra (*pluses*) and the best-fit PL model (*solid histogram*), and the other panels show the residuals from the best-fit by a PL, MCD, and Kawaguchi model.

Table 5.2: Best-fit parameters for M 51

Name	Data label	Model [a]	$N'_{\rm H}$ (10^{22} cm^{-2})	Γ	$kT_{\rm in}$ (keV)	$R_{\rm in}$ (km)	$M_{\rm BH}$ ($M_\odot$)	dM/dt ($L_{\rm Edd}\ c^{-2}$)	$L_{\rm X}$ (10^{38} ergs s^{-1})	Red$-\chi^2$ (d.o.f.)
Source-69	C1	P	< 0.08	$1.1^{+0.2}_{-0.1}$	···	···	···	···	27 ± 3	1.12(18)
		M	< 0.03	···	$2.3^{+1.2}_{-0.4}$	$26^{+26}_{-\ 9}$	···	···	$18^{+\ 3}_{-\ 2}$	1.33(18)
		K	$0.15^{+0.07}_{-0.07}$	···	···	···	$5^{+\ 6}_{-\ 3}$	$100^{+513}_{-\ 71}$	$16^{+\ 1}_{-\ 3}$	1.99(18)
	C2	P	0.06(fixed)	$3.1^{+1.1}_{-0.9}$	···	···	···	···	< 0.8	0.63(1)
		M	0.06(fixed)	···	$0.4^{+0.2}_{-0.1}$	123^{+143}_{-80}	···	···	< 0.4	0.14(1)
		K	0.06(fixed)	···	···	···	$10^{+\ 3}_{-\ 6}$	< 2	< 0.6	0.18(1)
	C3	P	$0.05^{+0.04}_{-0.04}$	$1.5^{+0.1}_{-0.1}$	···	···	···	···	29 ± 2	0.80(34)
		M	< 0.01	···	$1.5^{+0.2}_{-0.1}$	60^{+16}_{-10}	···	···	16 ± 1	1.94(34)
		K	$0.07^{+0.03}_{-0.03}$	···	···	···	$7^{+\ 4}_{-\ 3}$	$100^{+335}_{-\ 62}$	19 ± 1	1.13(34)
	X1	P	$0.14^{+0.11}_{-0.06}$	$1.9^{+0.1}_{-0.2}$	···	···	···	···	12 ± 1	0.86(40)
		M	< 0.03	···	$1.2^{+0.2}_{-0.1}$	55^{+21}_{-13}	···	···	6.1 ± 0.6	1.19(40)
		K	$0.05^{+0.06}_{-0.05}$	···	···	···	< 9	> 425	7.5 ± 0.7	0.91(40)
	X2	P	$0.09^{+0.03}_{-0.03}$	$1.7^{+0.0}_{-0.1}$	···	···	···	···	52 ± 2	1.18(110)
		M	0.00	···	$1.5^{+0.1}_{-0.1}$	$81^{+12}_{-\ 9}$	···	···	30 ± 1	2.03(110)
		K	$0.08^{+0.02}_{-0.02}$	···	···	···	$12^{+\ 2}_{-\ 5}$	$100^{+254}_{-\ 41}$	34 ± 1	1.33(110)
	X3	P	$0.09^{+0.03}_{-0.03}$	$1.6^{+0.1}_{-0.1}$	···	···	···	···	41 ± 2	1.58(113)
		M	0.00	···	$1.7^{+0.1}_{-0.1}$	$58^{+\ 8}_{-\ 9}$	···	···	25 ± 1	2.23(113)
		K	$0.10^{+0.02}_{-0.02}$	···	···	···	$10^{+\ 1}_{-\ 4}$	$100^{+154}_{-\ 34}$	$27^{+\ 2}_{-\ 1}$	1.76(113)
	X4	P	$0.10^{+0.03}_{-0.03}$	$1.5^{+0.1}_{-0.1}$	···	···	···	···	58 ± 2	1.41(111)
		M	< 0.01	···	$1.8^{+0.2}_{-0.1}$	$60^{+10}_{-\ 7}$	···	···	35 ± 2	1.80(111)
		K	$0.13^{+0.02}_{-0.02}$	···	···	···	$13^{+\ 2}_{-\ 5}$	$100^{+238}_{-\ 30}$	$38^{+\ 1}_{-\ 2}$	1.71(111)
Source-82	C1	P	$0.11^{+0.06}_{-0.06}$	$2.3^{+0.3}_{-0.2}$	···	···	···	···	28 ± 3	0.84(30)
		M	< 0.01	···	$0.7^{+0.1}_{-0.1}$	222^{+51}_{-47}	···	···	13 ± 1	1.48(30)
		K	$0.01^{+0.05}_{-0.01}$	···	···	···	$34^{+\ 7}_{-\ 9}$	$7^{+\ 3}_{-\ 1}$	$15^{+\ 2}_{-\ 1}$	0.95(30)
	C2	P	$0.02^{+0.03}_{-0.02}$	$1.9^{+0.2}_{-0.2}$	···	···	···	···	16 ± 1	1.13(30)
		M	< 0.01	···	$0.9^{+0.1}_{-0.1}$	121^{+38}_{-36}	···	···	8.5 ± 0.9	2.56(30)
		K	< 0.01	···	···	···	$12^{+\ 3}_{-\ 5}$	$14^{+\ 23}_{-\ 5}$	11 ± 1	1.31(30)
	C3	P	$0.12^{+0.05}_{-0.04}$	$2.1^{+0.1}_{-0.1}$	···	···	···	···	25 ± 2	1.60(34)
		M	< 0.01	···	$0.9^{+0.1}_{-0.1}$	146^{+21}_{-20}	···	···	12 ± 1	2.27(34)
		K	$0.04^{+0.03}_{-0.04}$	···	···	···	$22^{+10}_{-\ 8}$	$9^{+\ 7}_{-\ 2}$	14 ± 1	1.72(34)
	X1	P	$0.21^{+0.07}_{-0.06}$	$2.6^{+0.3}_{-0.2}$	···	···	···	···	$27^{+\ 4}_{-\ 3}$	1.18(47)
		M	< 0.03	···	$0.7^{+0.1}_{-0.1}$	191^{+39}_{-40}	···	···	11 ± 1	1.91(47)
		K	$0.08^{+0.05}_{-0.05}$	···	···	···	$37^{+\ 9}_{-\ 7}$	$5^{+\ 1}_{-\ 1}$	13 ± 1	1.45(47)
	X2	P	< 0.04	$1.8^{+0.2}_{-0.1}$	···	···	···	···	19 ± 2	0.97(31)
		M	< 0.01	···	$1.0^{+0.2}_{-0.1}$	107^{+34}_{-29}	···	···	11 ± 1	2.58(31)
		K	< 0.01	···	···	···	$11^{+\ 2}_{-\ 5}$	$20^{+\ 58}_{-\ 8}$	13 ± 1	1.22(31)
	X3	P	$0.11^{+0.04}_{-0.04}$	$2.2^{+0.2}_{-0.1}$	···	···	···	···	17 ± 1	0.87(75)
		M	< 0.01	···	$0.8^{+0.1}_{-0.1}$	152^{+26}_{-25}	···	···	8.1 ± 0.5	1.80(75)
		K	$0.01^{+0.03}_{-0.01}$	···	···	···	$17^{+\ 5}_{-\ 3}$	$7^{+\ 4}_{-\ 2}$	9.6 ± 0.6	1.13(75)
	X4	P	$0.14^{+0.05}_{-0.04}$	$2.2^{+0.1}_{-0.2}$	···	···	···	···	20 ± 2	0.83(62)
		M	< 0.01	···	$0.9^{+0.1}_{-0.1}$	132^{+26}_{-25}	···	···	9.6 ± 0.6	1.47(62)
		K	$0.04^{+0.04}_{-0.04}$	···	···	···	$19^{+\ 8}_{-\ 7}$	$8^{+\ 7}_{-\ 2}$	11 ± 1	1.03(62)

[a] The abbreviations for the models: "P" for PL, "M" for MCD (the `diskbb` model in XSPEC), and "K" for Kawaguchi model.

Table 5.3: Best-fit parameters for NGC 4490/85

Name	Data label	Model [a]	$N'_{\rm H}$ (10^{22} cm^{-2})	Γ	$kT_{\rm in}$ (keV)	$R_{\rm in}$ (km)	$M_{\rm BH}$ ($M_\odot$)	dM/dt ($L_{\rm Edd}\ c^{-2}$)	$L_{\rm X}$ (10^{38} ergs s^{-1})	Red$-\chi^2$ (d.o.f.)
ULX-2	C1′	P	$0.21^{+0.08}_{-0.07}$	$1.6^{+0.2}_{-0.2}$	···	···	···	···	52 ± 4	1.69(28)
		M	$0.05^{+0.05}_{-0.05}$	···	$1.6^{+0.2}_{-0.2}$	73^{+22}_{-17}	···	···	29 ± 2	1.34(28)
		K	$0.22^{+0.05}_{-0.04}$	···	···	···	$12^{+12}_{-\ 7}$	100^{+506}_{-74}	$35^{+\ 3}_{-\ 1}$	1.68(28)
	C2′	P	$0.21^{+0.06}_{-0.06}$	$1.8^{+0.2}_{-0.2}$	···	···	···	···	40 ± 2	0.94(35)
		M	$0.05^{+0.04}_{-0.04}$	···	$1.3^{+0.2}_{-0.1}$	92^{+22}_{-18}	···	···	20 ± 1	0.77(35)
		K	$0.18^{+0.04}_{-0.05}$	···	···	···	18^{+10}_{-13}	> 13	$25^{+\ 3}_{-\ 2}$	0.87(35)
	C3′	P	$0.28^{+0.08}_{-0.04}$	$1.8^{+0.1}_{-0.1}$	···	···	···	···	34 ± 2	1.63(28)
		M	$0.08^{+0.05}_{-0.05}$	···	$1.4^{+0.2}_{-0.1}$	72^{+18}_{-15}	···	···	18 ± 1	1.28(28)
		K	$0.24^{+0.06}_{-0.07}$	···	···	···	$15^{+\ 7}_{-10}$	> 14	22 ± 2	1.50(28)
	X1′	P	$0.27^{+0.07}_{-0.07}$	$2.1^{+0.1}_{-0.2}$	···	···	···	···	$40^{+\ 4}_{-\ 3}$	1.36(48)
		M	$0.02^{+0.05}_{-0.02}$	···	$1.2^{+0.1}_{-0.1}$	97^{+21}_{-20}	···	···	19 ± 1	1.60(48)
		K	$0.16^{+0.04}_{-0.04}$	···	···	···	$23^{+\ 9}_{-\ 6}$	$16^{+10}_{-\ 4}$	24 ± 2	1.40(48)
ULX-3	C1′	P	$0.82^{+0.35}_{-0.30}$	$2.0^{+0.4}_{-0.3}$	···	···	···	···	$36^{+12}_{-\ 7}$	1.05(22)
		M	$0.37^{+0.24}_{-0.21}$	···	$1.5^{+0.4}_{-0.3}$	65^{+38}_{-25}	···	···	18 ± 2	1.14(22)
		K	$0.65^{+0.21}_{-0.20}$	···	···	···	17^{+16}_{-13}	> 12	22 ± 4	1.06(22)
	C2′	P	$1.39^{+0.25}_{-0.23}$	$2.4^{+0.3}_{-0.3}$	···	···	···	···	58^{+21}_{-14}	0.63(30)
		M	$0.79^{+0.17}_{-0.15}$	···	$1.2^{+0.2}_{-0.1}$	113^{+30}_{-25}	···	···	27 ± 2	0.67(30)
		K	$1.08^{+0.15}_{-0.15}$	···	···	···	$40^{+\ 8}_{-\ 7}$	$14^{+\ 5}_{-\ 2}$	$33^{+\ 5}_{-\ 6}$	0.60(30)
	C3′	P	$1.08^{+0.19}_{-0.17}$	$2.1^{+0.2}_{-0.2}$	···	···	···	···	$51^{+\ 9}_{-\ 7}$	0.90(33)
		M	$0.60^{+0.13}_{-0.12}$	···	$1.4^{+0.2}_{-0.1}$	78^{+19}_{-16}	···	···	23 ± 2	0.84(33)
		K	$0.89^{+0.12}_{-0.11}$	···	···	···	$29^{+\ 6}_{-10}$	$17^{+11}_{-\ 4}$	$29^{+\ 5}_{-\ 2}$	0.82(33)
	X1′	P	$0.85^{+0.22}_{-0.20}$	$1.8^{+0.2}_{-0.1}$	···	···	···	···	$44^{+\ 8}_{-\ 6}$	1.00(33)
		M	$0.39^{+0.14}_{-0.13}$	···	$1.8^{+0.3}_{-0.2}$	50^{+17}_{-13}	···	···	25 ± 2	1.10(33)
		K	$0.74^{+0.15}_{-0.10}$	···	···	···	$12^{+15}_{-\ 7}$	> 23	$29^{+\ 4}_{-\ 3}$	1.00(33)
ULX-4	C1′	P	$0.49^{+0.20}_{-0.16}$	$1.9^{+0.3}_{-0.2}$	···	···	···	···	$25^{+\ 4}_{-\ 3}$	1.08(17)
		M	$0.22^{+0.13}_{-0.12}$	···	$1.5^{+0.4}_{-0.3}$	55^{+29}_{-20}	···	···	$13^{+\ 2}_{-\ 1}$	1.15(17)
		K	$0.41^{+0.13}_{-0.12}$	···	···	···	$12^{+\ 6}_{-\ 9}$	> 12	$16^{+\ 2}_{-\ 3}$	1.08(17)
	C2′	P	$0.63^{+0.17}_{-0.15}$	$1.9^{+0.1}_{-0.2}$	···	···	···	···	$51^{+\ 7}_{-\ 6}$	1.36(29)
		M	$0.29^{+0.11}_{-0.10}$	···	$1.5^{+0.2}_{-0.2}$	81^{+24}_{-19}	···	···	27 ± 2	1.24(29)
		K	$0.54^{+0.11}_{-0.11}$	···	···	···	$26^{+\ 9}_{-20}$	> 16	$33^{+\ 5}_{-\ 2}$	1.29(29)
	C3′	P	$0.64^{+0.13}_{-0.06}$	$1.9^{+0.1}_{-0.1}$	···	···	···	···	42 ± 4	1.63(28)
		M	$0.34^{+0.09}_{-0.08}$	···	$1.5^{+0.2}_{-0.2}$	70^{+17}_{-14}	···	···	22 ± 1	1.42(28)
		K	$0.57^{+0.09}_{-0.11}$	···	···	···	$19^{+\ 9}_{-14}$	> 16	27 ± 2	1.53(28)
	X1′	P	$0.60^{+0.12}_{-0.11}$	$2.0^{+0.2}_{-0.1}$	···	···	···	···	$50^{+\ 7}_{-\ 5}$	1.32(44)
		M	$0.30^{+0.08}_{-0.07}$	···	$1.3^{+0.1}_{-0.1}$	99^{+20}_{-17}	···	···	26 ± 2	0.98(44)
		K	$0.50^{+0.08}_{-0.07}$	···	···	···	$34^{+\ 5}_{-\ 8}$	$17^{+\ 7}_{-\ 3}$	$31^{+\ 3}_{-\ 2}$	1.14(44)
ULX-6	C1′	P	$0.35^{+0.23}_{-0.18}$	$1.8^{+0.2}_{-0.3}$	···	···	···	···	$23^{+\ 4}_{-\ 3}$	0.72(17)
		M	$0.10^{+0.15}_{-0.10}$	···	$1.4^{+0.5}_{-0.3}$	53^{+37}_{-22}	···	···	$12^{+\ 2}_{-\ 1}$	0.79(17)
		K	$0.28^{+0.15}_{-0.12}$	···	···	···	$10^{+\ 7}_{-\ 8}$	> 11	15 ± 2	0.73(17)
	C2′	P	$0.60^{+0.35}_{-0.20}$	$2.6^{+0.6}_{-0.4}$	···	···	···	···	$7^{+\ 7}_{-\ 3}$	1.09(10)
		M	$0.15^{+0.22}_{-0.15}$	···	$0.9^{+0.3}_{-0.2}$	64^{+41}_{-29}	···	···	$3.0^{+0.6}_{-0.5}$	1.45(10)
		K	$0.35^{+0.23}_{-0.21}$	···	···	···	$12^{+\ 7}_{-\ 6}$	$15^{+\ 4}_{-\ 1}$	$3.8^{+1.3}_{-1.0}$	1.24(10)
	C3′	P	$0.88^{+0.16}_{-0.14}$	$2.4^{+0.2}_{-0.2}$	···	···	···	···	$53^{+10}_{-\ 7}$	1.49(31)
		M	$0.45^{+0.10}_{-0.09}$	···	$1.1^{+0.1}_{-0.1}$	124^{+24}_{-21}	···	···	$21^{+\ 2}_{-\ 1}$	0.93(31)
		K	$0.65^{+0.10}_{-0.09}$	···	···	···	$37^{+\ 5}_{-\ 4}$	$11^{+\ 2}_{-\ 2}$	26 ± 2	1.06(31)
	X1′	P	$0.41^{+0.08}_{-0.08}$	$2.1^{+0.1}_{-0.1}$	···	···	···	···	44 ± 4	1.12(52)
		M	$0.11^{+0.05}_{-0.05}$	···	$1.4^{+0.1}_{-0.1}$	86^{+16}_{-14}	···	···	23 ± 1	1.07(52)
		K	$0.30^{+0.05}_{-0.05}$	···	···	···	$27^{+\ 7}_{-\ 7}$	$17^{+\ 8}_{-\ 4}$	$27^{+\ 2}_{-\ 3}$	1.02(52)

ULX-8	C1′	P	$0.86^{+0.24}_{-0.20}$	$2.3^{+0.3}_{-0.3}$	···	···	···	···	$56^{+15}_{-\ 9}$	1.45(20)
		M	$0.46^{+0.15}_{-0.13}$	···	$1.2^{+0.2}_{-0.1}$	116^{+34}_{-28}	···	···	24 ± 2	0.96(20)
		K	$0.68^{+0.15}_{-0.14}$	···	···	···	$37^{+\ 8}_{-\ 8}$	$12^{+\ 5}_{-\ 2}$	30 ± 4	1.13(20)
	C2′	P	$0.90^{+0.16}_{-0.14}$	$2.6^{+0.2}_{-0.2}$	···	···	···	···	$46^{+13}_{-\ 9}$	1.28(26)
		M	$0.43^{+0.10}_{-0.09}$	···	$1.0^{+0.1}_{-0.1}$	147^{+28}_{-25}	···	···	19 ± 2	0.75(26)
		K	$0.60^{+0.12}_{-0.09}$	···	···	···	$40^{+13}_{-\ 5}$	$9^{+\ 1}_{-\ 2}$	$23^{+\ 3}_{-\ 2}$	0.82(26)
	C3′	P	$0.74^{+0.12}_{-0.11}$	$2.0^{+0.2}_{-0.1}$	···	···	···	···	$59^{+\ 7}_{-\ 5}$	1.52(36)
		M	$0.38^{+0.08}_{-0.07}$	···	$1.4^{+0.1}_{-0.1}$	90^{+18}_{-16}	···	···	28 ± 2	1.47(36)
		K	$0.61^{+0.08}_{-0.07}$	···	···	···	$32^{+\ 4}_{-10}$	$20^{+12}_{-\ 4}$	35 ± 4	1.41(36)
	X1′	P	$0.64^{+0.10}_{-0.09}$	$2.5^{+0.2}_{-0.2}$	···	···	···	···	$54^{+\ 9}_{-\ 7}$	0.88(58)
		M	$0.26^{+0.07}_{-0.06}$	···	$1.0^{+0.1}_{-0.1}$	152^{+28}_{-25}	···	···	21 ± 1	0.92(58)
		K	$0.39^{+0.08}_{-0.06}$	···	···	···	$38^{+10}_{-\ 3}$	$10^{+\ 1}_{-\ 3}$	$26^{+\ 2}_{-\ 3}$	0.86(58)

[a] Same with Table 5.2.

5.2 Galactic BHBs

Here, we focus on Galactic BHBs from which large enough photon counts of >10,000 (background-subtracted; see Table 4.6) have been accumulated, since such large counts are necessary to investigate spectral evolutions. The following 11 sources have been selected: LMC X-3, LMC X-1, 4U 1630−47, GX 339−4, H 1743−322, XTE J1752−223, Swift J1753.5−0127, GRS 1915+105, Cyg X-1, 4U 1957+11, and Cyg X-3.

The total photon counts (background-subtracted) from the 11 BHBs and the seven ULXs are about 200,000 (Table 4.6) and 51,000 counts (Tables 4.3 and 4.4), respectively. Thus, the data quality for BHBs by *MAXI* is higher than that of the ULXs by *Chandra* by a factor of ∼40. In this section, we focus on only a simple phenomenological behavior between the photon index and the luminosity derived by the PL model in order to compare with the result of ULXs.

For the spectral fitting, we accumulated spectrum in time-order along the light curve, so that each spectrum has more than 5000 counts for each exposure of a BHB. In order to avoid confusion of different spectral states, we divided light curves by using the "Bayesian blocks method" and created the spectrum within the same block. In this section, we first explain the Bayesian blocks method, and then present the spectral analysis and results of the Galactic BHBs.

5.2.1 Light Curves

We used the Bayesian blocks method (Scargle 1998[144]) to divide the light curves into time-segments. The algorithm approximates light curves with a set of "segments" with constant count rates by iteratively evaluating additional switching points of the counting rates. We consider that the switching points *may* correspond to the spectral change points.

We show the divided light curves (2–20 keV and different three energy bands) of all the BHBs in Figure 5.3. We note two points: First, we applied the algorithm to light curves integrated for four days, because the photon counts of each day are too small. Second, we treat the non-data intervals (due to one of the reasons explained in § 4.2.3) as parts of the segments. This is because a BHB might cause a spectral transition within such non-data intervals.

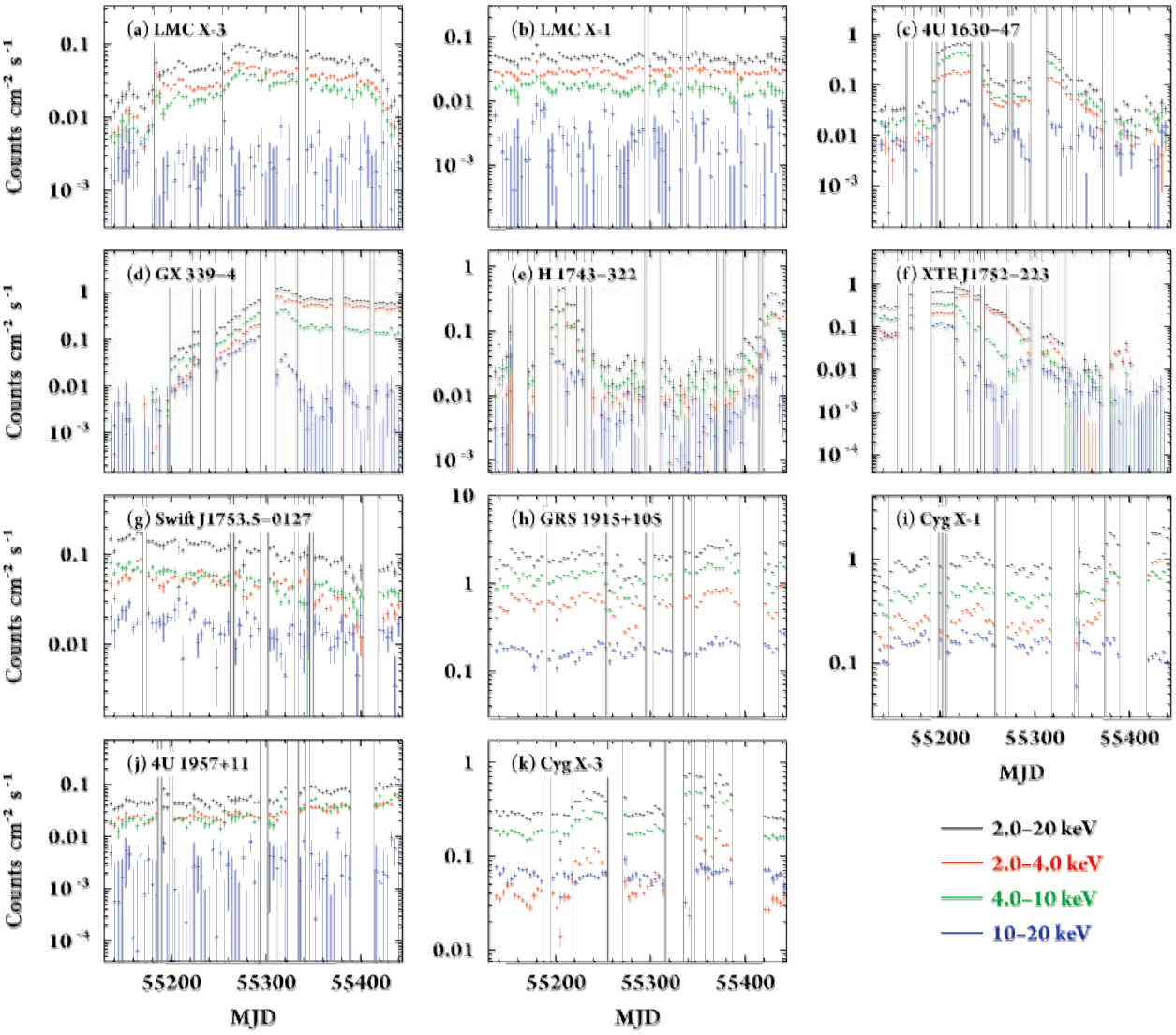

Figure 5.3: Divided light curves of the BHBs in 2–20 keV (*black*), 2–4 keV (*red*), 4–10 keV (*green*), and 10–20 keV (*blue*). Each segment is partitioned by solid lines. Each plus is integrated for four days.

5.2.2 Spectra

For all the BGBs, we created a series of spectra with each about 5000 counts. All the spectral channels were binned with at least 50 counts bin^{-1}. All spectra are featureless except for the spectra of Cyg X-3, which is explained later in detail.

Fitting Models

We used the X-ray spectral fitting package XSPEC version 12.6.0 for the spectral analysis for *MAXI*. We applied the `wabs` model for the interstellar extinction, following the ULX analysis. However, it is difficult to determine the hydrogen column density (N_{H}) less than 5×10^{22} cm^{-2}, because *MAXI*/GSC does not have a sensitivity in the low energy band, <2 keV. Since interstellar hydrogen column densities for these BHBs have already been measured in previous studies (Table 4.5), we adopted these values as long as they are smaller than 5×10^{22} cm^{-2}. When the values are larger than 5×10^{22} cm^{-2}, we treated the hydrogen column density as a free parameter.

In order to obtain the phenomenological relation between the photon index and the luminosity, we applied the PL model for all the BHB spectra. Exceptionally, we applied a PL model plus a Gaussian component for the spectra of Cyg X-3, because almost all spectra have an emission line at about 6.7 keV. In fact, most of the fittings were improved by adding a line component (F-test significance of $\geq$95%). For Cyg X-3, the existence of a strong line at about 6.7 keV has already been known from 1970's (e.g., Sanford et al. 1975[142]; Szostek et al. 2008[158]).

Fitting Results

After the spectral fitting in the 2–20 keV band, we extrapolated the absorption-corrected flux $f'_{\mathrm{X,PL}}$ in the 0.5–8.0 keV band in order to compare with the result of ULXs. We then calculated the luminosity as $L_{\mathrm{X,PL}} = 4\pi D^2 f'_{\mathrm{X,PL}}$ by using $f'_{\mathrm{X,PL}}$, following the method adopted for ULX. Here, D is the distance to each BHB (Table 4.5).

We summarize the plot of $L_{\mathrm{X,PL}}$ against Γ (Figure 5.4). Errors of Γ are calculated at a 90% confidence level. In Figure 5.4, we distinguish between the successful fittings (black) and the others (red). We consider that the fitting with a null hypothesis probability of

>5% is successful. We caution the following three points: (i) The red pluses do not show the precise positions on the $L_{\rm X,PL}$–Γ plot, because they are not the successful fitting parameters. (ii) These plots indicate only the *phenomenological* behavior and not the *physical* behavior, especially $\Gamma \gtrsim 3$ might be unphysical (diverge in lower energies). (iii) Due to the unphysical (too steep) photon index, we tend to overestimate the absorption-corrected flux $f'_{\rm X,PL}$. In fact, two sources (4U 1630−47 and GRS 1915+105) seem to significantly exceed 1×10^{39} ergs s^{-1}, which might be caused by an artificial effect due to the too large photon index.

In the plot, most of the sources (eight among 11) have the positive slope; i.e., its power increases as an increasing luminosity ($\Gamma \propto {L_{\rm X,PL}}^{b}$ where $b > 0$). For the eight sources, we summarize the power b from the black pluses without $\Gamma \gtrsim 3$ and their average luminosities in Table 5.4.

Table 5.4: Average luminosity and the power on the $L_{\rm X,PL}$–Γ plot

Name	Ave. $L_{\rm X,PL}$ [a] (10^{38} ergs s^{-1})	b [a, b]
4U 1630−47	0.21	0.14 ± 0.11
GX 339−4	0.22	0.09 ± 0.04
H 1743−322	0.16	0.11 ± 0.04
XTE J1752−223	0.34	0.32 ± 0.02
Swift J1753.5−0127	0.15	0.29 ± 0.04
GRS 1915+105	18	0.13 ± 0.01
Cyg X-1	0.12	0.26 ± 0.01
Cyg X-3	1.1	0.25 ± 0.02

[a] Parameter calculated from the black pluses without $\Gamma \gtrsim 3$ on Figure 5.4.

[b] The power b of $\Gamma \propto {L_{\rm X,PL}}^{b}$.

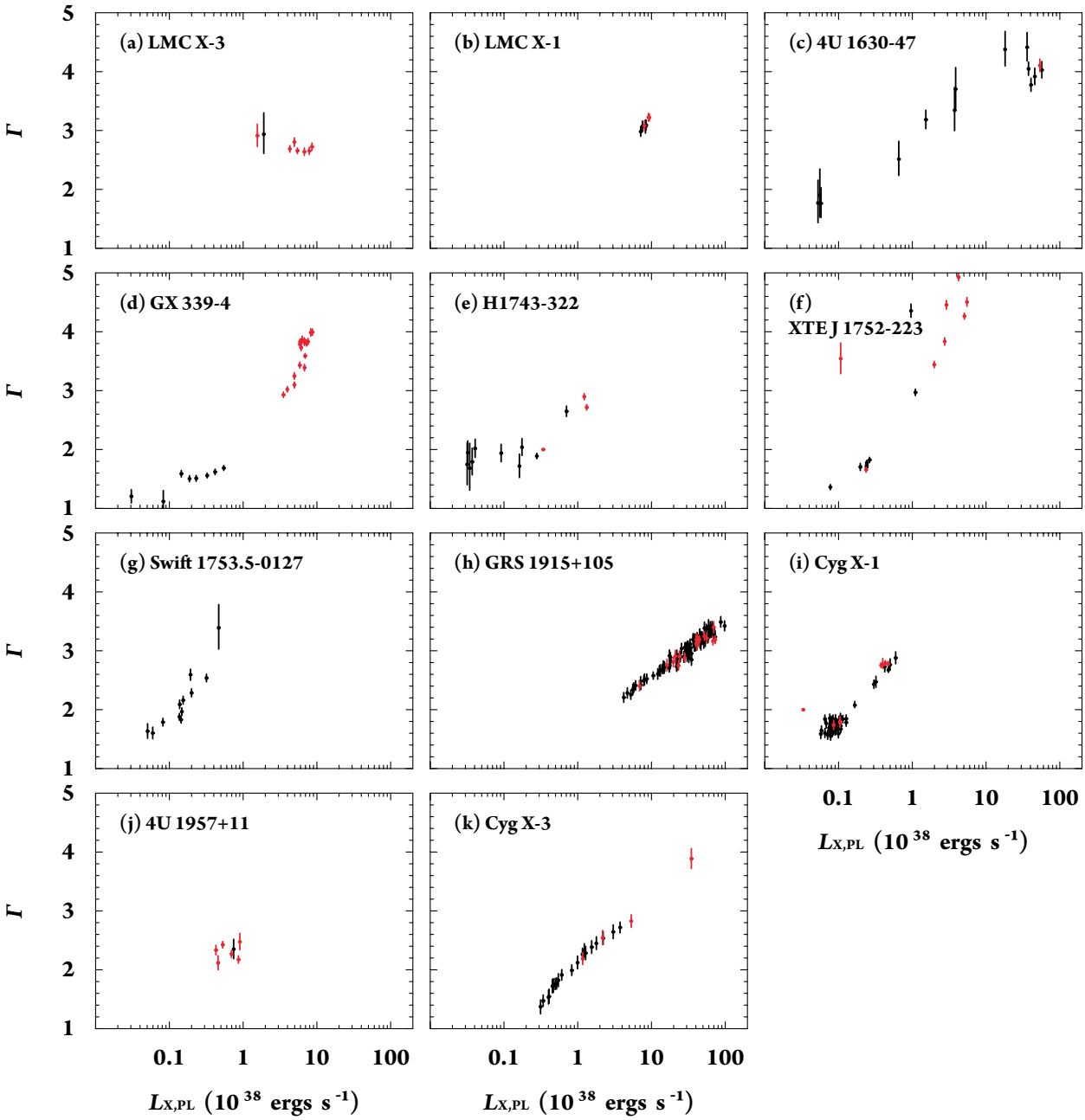

Figure 5.4: Plot of X-ray luminosity $L_{\rm X,PL}$ (0.5–8.0 keV) against the photon index Γ based on the PL fitting results. Black pluses represent the fitting with a null hypothesis probability of >5%, while red pluses are the others.

Chapter 6

Discussion

In this chapter, we first discuss the general trend of ULX spectra (§ 6.1), and then look into the details of individual ULXs for determining the states of each ULX and its mass (§ 6.2). Finally, we compare the states of the ULXs with those of Galactic BHBs, and investigate the relation between each state (§ 6.3).

Contents

6.1 ULX Spectral States and Transitions

Based on the spectral fitting results presented in § 5.1.2, we investigate the spectral states of ULXs and their transitions. It is desirable that the states be defined for individual sources. However, given the low photon counts of each source, starting with individual details may lead to an unclear view. We thus first investigate the overall trend of all samples to constrain states of ULXs as a whole. In this section, we develop a discussion under the working hypothesis that all ULXs have a similar mass and have the same states and follow a similar pattern of state transitions. The working hypothesis is checked with individual sources in § 6.2.

We constructed a histogram of the samples fitted successfully with the PL or the MCD model that represents PL-like and curved spectra, respectively (Figure 6.1). We consider that the fitting with a null hypothesis probability of >5% is successful. The best-fit luminosities derived by the PL fitting are used, because the derived luminosities hardly depend on the fitted models.

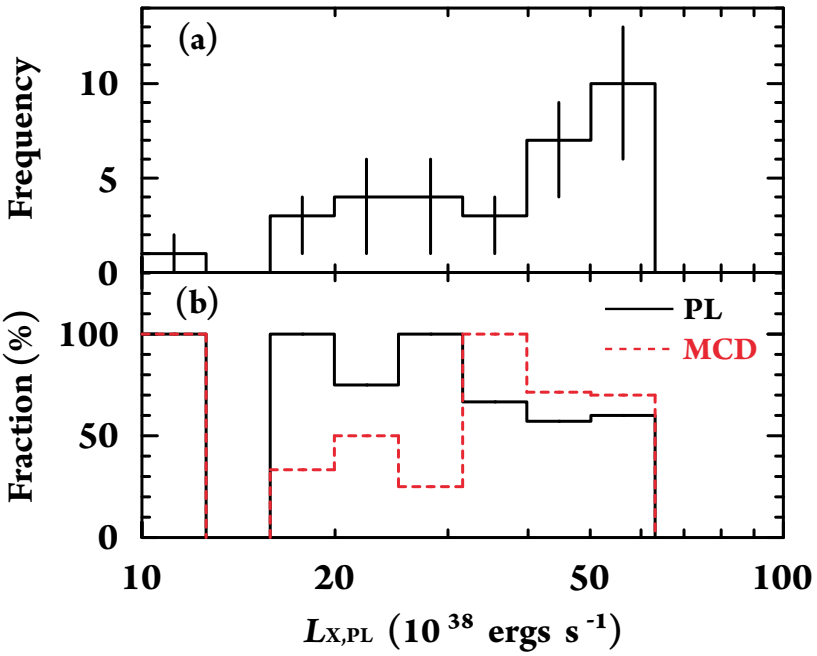

Figure 6.1: Luminosity distribution of (a) the number of samples and (b) the fraction of successful fits by the PL (*black*) and the MCD (*red*) models. The 1σ uncertainty, which is calculated from the Poisson distribution, is given in (a).

In the plot, it is noticeable that the fraction of successful fits by the MCD model is higher within the range of 3–6$\times10^{39}$ ergs s^{-1} for 20 samples and that by the PL model is higher within the range of 1.5–3$\times10^{39}$ ergs s^{-1} for 11 samples (Figure 6.1b). In order to test the claim statistically, we simulated numerous spectra containing the two components (PL and MCD) with randomly chosen parameters with varying contrasts, fitted them with one component model of either the PL or the MCD, and derived the fraction of the successful fits. As a result, we did not find a trend that the MCD model is favored toward brighter luminosity. Indeed, the PL model was favored. Thus, we consider that the higher fraction of successful MCD fits toward the brighter luminosity is not a statistical artifact. This simulation is explained in detail in Appendix A.

The bimodal structure in the luminosity is unlikely to be explained by the bimodal distribution of the BH mass or the inclination of the system. This is because the distribution of the mass or the angle should be continuous, thus such a bimodal distribution is not natural. Rather, we speculate that there are two distinctive states corresponding to each luminosity range. We hereafter call them the "*bright*" state and the "*faint*" state. The two states match the "soft" and the "hard" states of the ULXs in Kubota et al. (2001)[75]. Based on the number of samples in each state, the frequency ratio *bright*:*faint* is about 2:1. The transition between the two occurs at $\sim3\times10^{39}$ ergs s^{-1} (hereafter the "border luminosity"). Gladstone & Roberts (2009)[55] also claimed that the changes in spectral state occur at a similar luminosity of $\sim2\times10^{39}$ ergs s^{-1} using samples in NGC 4490/85.

Some samples do not belong to either of the two states. Three samples (M 51 source-69 in C2, X1, and NGC 4490/85 ULX-6 in C2′) show luminosities fainter than the tail of the *faint* state. These spectra may belong to the third state, which we call the "*dim*" state. We cannot constrain its representative spectral model for the paucity of statistics.

Two types of luminosity variation are recognized. We designate the variations within one state as the "*intra-state*" variations, and those across two or more states as the "*inter-state*" transitions.

6.2 Spectral Variations of Individual Sources

Now, we look into details of individual sources. The following result shows that the BH mass is in a range of 30–40 $M_\odot$ for sources which we can estimate a mass with a representative

model. This supports our assumption to derive the overall trend in § 6.1. All the samples can be considered to be in one of the three states defined in § 6.1. The spectra in the *bright* state are explained better with a curved model and those in the *faint* state with a PL model. For the curved model, we see that the Kawaguchi model better explains the sources with sufficient constraints.

For each individual source, we discuss the states of all samples and the most likely representative model for each state. The result of spectral fitting is employed, which is mainly used to distinguish PL-like or curved spectra. If both the MCD and the Kawaguchi models give an acceptable fit for a curved spectrum, we further use a plot of $L_{\rm X,MCD}$ against $kT_{\rm in}$ (Figure 6.2) to distinguish the two. The plot is commonly used for Galactic BHBs and ULXs. The two parameters are correlated in a different manner in two different physical conditions: standard disk or slim disk. If a system has a standard disk (the MCD model), the relation $L_{\rm X,MCD} \propto {T_{\rm in}}^4$ is obtained, which is interpreted that the innermost disk radius remains constant against varying accretion rates in the state (Shakura & Sunyaev 1973[147]; Ebisawa et al. 1993[34]; Gierliński & Done 2004[54]). If a system has a slim disk (the Kawaguchi model), the relation $L_{\rm X,MCD} \propto {T_{\rm in}}^{\beta}$ is obtained, where $\beta \lesssim 4$ (Watarai et al. 2000[184]). The power β decreases from 4 as an increasing mass accretion rate (Watarai et al. 2001[185]). For samples with a successful fit by the MCD or Kawaguchi model or both, we derived the best-fit $M_{\rm BH}$ value and examined if it is consistent among all samples belonging to a source.

6.2.1 NGC 4490/85 ULX-8

We consider that ULX-8 exhibited an intra-state variation within the *bright* state. This is because the luminosity variation (4.6–6.0$\times10^{39}$ ergs s^{-1}) happens only above the border luminosity.

We speculate that this ULX is in the slim disk state based on the two lines of evidence. The first is that the scatter in the $L_{\rm X,MCD}$–$T_{\rm in}$ plot (Figure 6.2e) follows $L_{\rm X,MCD} \propto {T_{\rm in}}^{\beta}$, where $\beta = 1.0^{+0.7}_{-0.4}$. The value is consistent with the slim disk ($\beta \lesssim 4$) and not with the standard disk ($\beta \sim 4$). We note that the value is not an apparent slope caused by an additional spectral component (e.g., an additional PL component generally found in the HSS), because we obtained an even flatter slope ($\beta = 0.6^{+0.7}_{-0.3}$) when the spectra were fitted by two component models (the PL plus the MCD). Here, we fixed the photon index of the additional PL component to be 2.0 for the lack of statistics to constrain the value.

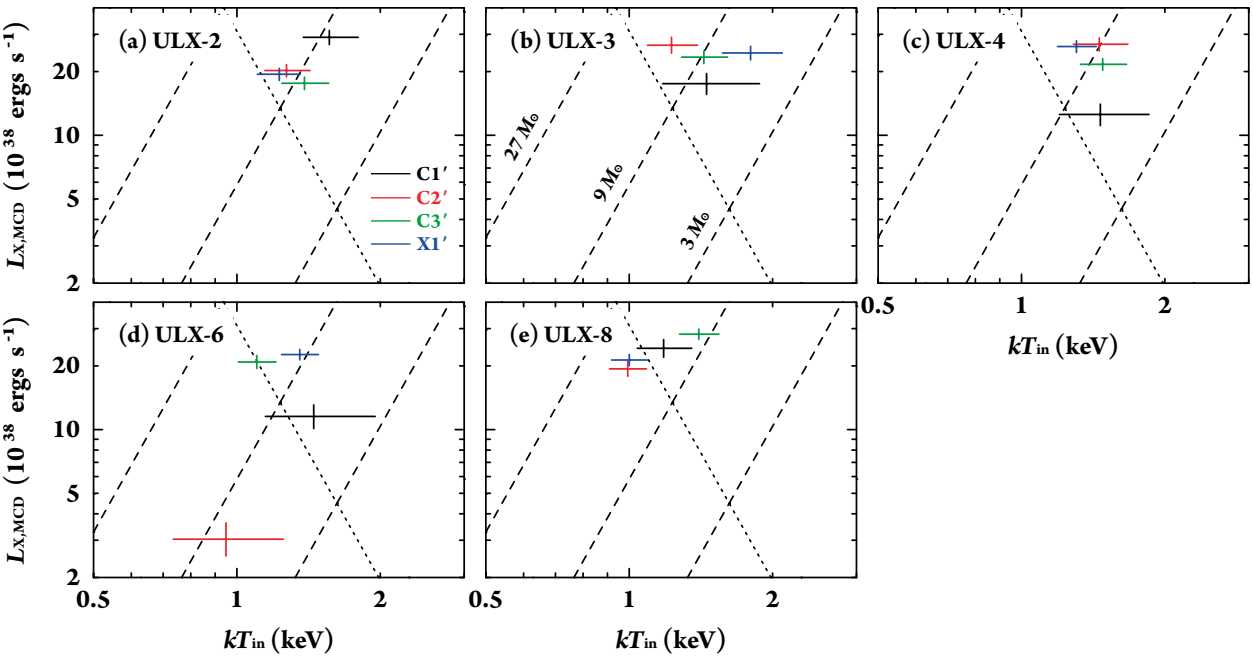

Figure 6.2: Plot of X-ray luminosity $L_{\rm X,MCD}$ against the innermost disk temperature $kT_{\rm in}$ based on the MCD fitting results. The results of different observations are shown in different colors. The dashed lines show the $L_{\rm X,MCD} \propto {T_{\rm in}}^4$ relation with several representative masses, while the dotted line indicates the Eddington luminosity for the standard disk.

The second evidence is that a BH mass consistent among all the samples is found for the Kawaguchi model, but not for the MCD model. Figure 6.3 shows the best-fit parameters using the MCD and Kawaguchi models. In the MCD fitting (Figure 6.3a), a value $(R_{\rm in}/{\rm km})^2/(D/10\ {\rm kpc})^2\ (\cos i)^{-1} \propto {M_{\rm BH}}^2$ consistent among the four samples was not found within 90% statistical uncertainty, which is unphysical. In other words, although spectra of ULXs in the *bright* state are commonly analyzed using the MCD model (e.g., Kubota et al. 2001[75]), it now turns out that the MCD model does not describe the long-term spectral variations of the *bright* state. On the other hand, in the Kawaguchi model fitting (Figure 6.3b), the range $M_{\rm BH} = 35$–$38\ M_\odot$ was found to be consistent within 90% among the four samples. Thus, at least for this source, the Kawaguchi model is a more favorable description for its spectral variation.

Now we found a common BH mass range acceptable for the four samples, we fitted the four spectra by tying the BH mass to obtain a more stringent constraint. The best-fit value of $M_{\rm BH}$ is $37 \pm 2\ M_\odot$ (Table 6.1). Resultantly, the Eddington ratio ($L_{\rm X}/L_{\rm Edd}$) is 0.41–0.63, which is similar to those of other ULX spectra considered to be in the slim disk state (0.36 for NGC 1313 X-2 and 0.52 for NGC 4559 X-7; Vierdayanti et al. 2006[178]).

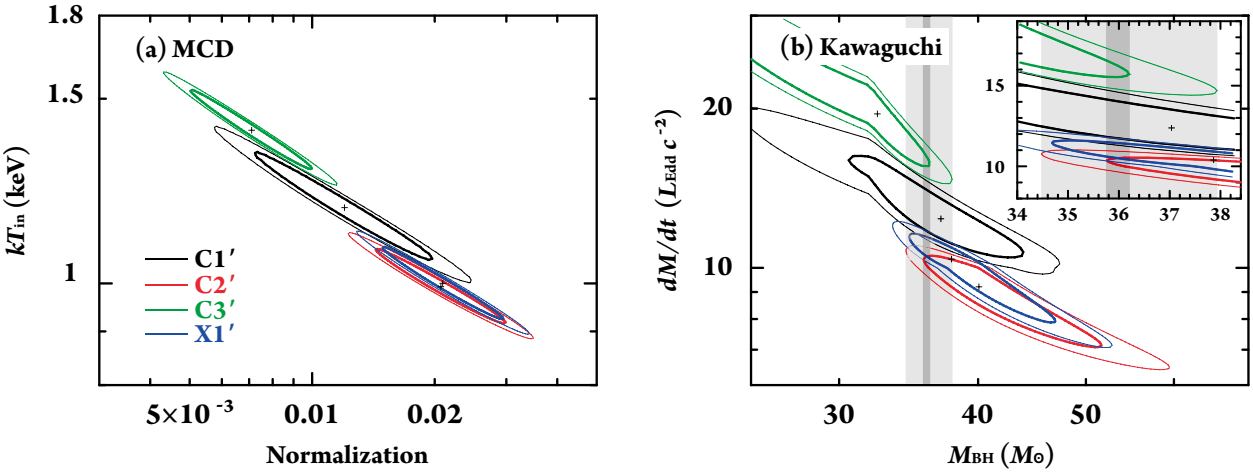

Figure 6.3: Significance contours of the best-fit physical parameters by two different models for NGC 4490/85 ULX-8; (a) $kT_{\rm in}$ versus the normalization ($\propto {M_{\rm BH}}^2$) by the MCD model. (b) dM/dt versus $M_{\rm BH}$ by the Kawaguchi model. The results in different observations are shown with different colors: C1′ (*black*), C2′ (*red*), C3′ (*green*), and X1′ (*blue*). The two confidence levels are shown for 68% (*thick solid*) and 90% (*thin solid*) ranges for the two parameters. The inset at the top right in (b) is a close-up view of the center in the linear scale. The dark and light gray shaded ranges indicate the common $M_{\rm BH}$ ranges among the four samples with a 68% and 90% confidence, respectively.

Table 6.1: Best-fit parameters of the Kawaguchi model for ULX-8

Data label	$N'_{\rm H}$ (10^{22} cm^{-2})	dM/dt ($L_{\rm Edd}\ c^{-2}$)	$L_{\rm X,Kaw}$ (10^{38} ergs s^{-1})
C1′	$0.68^{+0.10}_{-0.09}$	12^{+2}_{-1}	30 ± 3
C2′	$0.55^{+0.07}_{-0.06}$	10^{+1}_{-1}	$22^{+\ 3}_{-\ 2}$
C3′	$0.68^{+0.06}_{-0.06}$	15^{+2}_{-1}	36 ± 2
X1′	$0.38^{+0.05}_{-0.04}$	11^{+1}_{-1}	$26^{+\ 3}_{-\ 2}$
$M_{\rm BH}$[a]$(M_\odot)$			37 ± 2
Red$-\chi^2$ (d.o.f.)			1.04(143)

[a] The BH mass is fixed among the four independent fittings.

6.2.2 M 51 Source-82

Source-82 shows variability among samples, which we consider to be an intra-state origin within the *faint* state. This is because the luminosity variation (1.6–2.9×10^{39} ergs s^{-1}) happens only below the border luminosity.

We consider that the source stayed in the state represented by the PL model in all samples based on the following three reasons: (i) The majority of samples (six out of all seven) are successfully explained by a PL model. (ii) None of the samples is explained by an MCD model. (iii) Although the Kawaguchi model reproduces all the samples, the model is unlikely because we do not find $M_{\rm BH}$ consistent among all the samples (Figure 6.4).

In one sample (X1), source-82 shows a steep photon index of $2.6^{+0.3}_{-0.2}$ (Table 5.2). In contrast, in the other six samples, the derived index ($\Gamma \sim 1.8$–2.2; Table 5.2) is flatter than that in X1.

6.2.3 M 51 Source-69

Source-69 clearly caused an inter-state transition. This ULX exhibits the largest luminosity variation by at least a factor of 70, and shows a transition among the *bright* state (X2, X3, and X4; 4.0–5.8×10^{39} ergs s^{-1}), the *faint* state (C1 and C3; 2.6–2.9×10^{39} ergs s^{-1}), and the *dim* state (C2 and X1; <1.2×10^{39} ergs s^{-1}).

We discuss the representative model for the three states of the ULX. First, in the

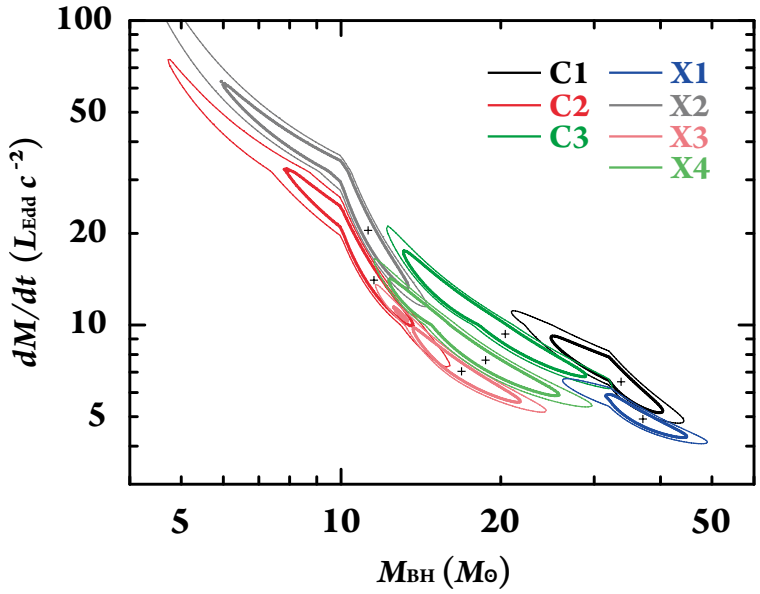

Figure 6.4: Significance contours of the best-fit physical parameters (dM/dt versus $M_{\rm BH}$) by the Kawaguchi model for M 51 source-82; The results in different observations are shown with different colors: C1 (*black*), C2 (*red*), C3 (*green*), X1 (*blue*), X2 (*gray*), X3 (*light red*), and X4 (*light green*). The two confidence levels are shown for 68% (*thick solid*) and 90% (*thin solid*) ranges.

bright state, none of the PL, MCD, and Kawaguchi models explains all the three samples (Table 5.2). In particular, two samples (X3 and X4) were not reproduced by any models. We employed two component models (the PL plus the MCD or the Kawaguchi model), which did not improve the fit. The representative model was not found for this source in this state.

Second, the PL is the representative model for the *faint* state, because it is the only model to reproduce spectra of all samples. The derived index is quite flat of $\Gamma < 1.5$.

Finally, for the *dim* state, any models can reproduce the spectra and the representative model was not constrained. We note, however, that the spectra in this state are softer ($\Gamma \sim 1.9$–3.1) than in the other two states ($\Gamma < 1.7$).

6.2.4 NGC 4490/85 ULX-6

We consider that ULX-6 caused an inter-state transition because the variation spans the three different luminosity ranges as M 51 source-69: the *bright* state (C3′ and X1′; 4.4–5.3×10^{39} ergs s^{-1}), the *faint* state (C1′; $\sim2.3\times10^{39}$ ergs s^{-1}), and the *dim* state (C2′; $\sim7.2\times10^{38}$ ergs s^{-1}).

For the *bright* state, both the MCD and the Kawaguchi models can explain all the spectra, and yielded a BH mass consistent among the two samples. However, the flat slope ($\beta = 0.4^{+1.7}_{-0.6}$) of the $L_{\rm X,MCD}$–$T_{\rm in}$ plot (Figure 6.2d) favors the slim disk interpretation ($\beta \lesssim 4$). Thus, the representative model of the ULX in this state is expected to be the Kawaguchi model. We tried a simultaneous fitting by tying the $M_{\rm BH}$ value using the Kawaguchi model, and obtained the best-fit BH mass of 33^{+2}_{-5} $M_\odot$. The Eddington ratio is 0.53–0.55.

For the *faint* and *dim* states, all the models can explain all the samples, thus the representative model was not constrained. In the *dim* state, the PL fitting yielded the best-fit power of ~ 2.6, which is similar to that found in the *dim* state of M 51 source-69.

6.2.5 NGC 4490/85 the other ULXs

The remaining three sources have no clear features, thus the representative model and the BH mass can hardly be constrained. We briefly describe these sources.

Both ULX-2 and ULX-3 show intra-state variation as their luminosity ($L_{\rm X,PL} \sim 3.3$–5.2 and 3.5–5.8×10^{39} ergs s^{-1}, respectively) stays in the *bright* state. For ULX-2, no model

explains all the samples, thus the representative model was not found for this source. For ULX-3, any models can reproduce all the spectra. The $L_{\rm X,MCD}$–$T_{\rm in}$ plot does not separate the slim disk or the standard disk state, because the data cannot be fitted with a linear relation. A BH mass consistent among all the samples is found both for the MCD and the Kawaguchi models as $8 \pm 1\ M_\odot$ and $28^{+6}_{-7}\ M_\odot$, respectively.

ULX-4, on the other hand, is considered to have exhibited an inter-state transition. The luminosities of the three samples are in the *bright* state (C2′, C3′, and X1′; 4.2–5.1×10^{39} ergs s^{-1}), while that of the other is in the *faint* state (C1′; $\sim2.5\times10^{39}$ ergs s^{-1}). In both states, any models explain most of the samples, and the representative model cannot be constrained for the same reasons as ULX-3. If we estimate the BH mass using a simultaneous fitting of the two samples in the *bright* state, the BH mass is obtained as $9 \pm 1\ M_\odot$ (MCD) and $26^{+\ 6}_{-10}\ M_\odot$ (Kawaguchi).

6.3 Relations with Galactic BHBs

Many previous studies (e.g., Kubota et al. 2001[75]; Dewangan et al. 2005[28]; Winter et al. 2006[187]; Vierdayanti et al. 2006[178]; Gladstone & Roberts 2009[55]; Godet et al. 2009[58]) suggested that the states of ULXs are related to those of Galactic BHBs. In the present study, we uniformly analyzed 34 spectra of seven ULXs in two interacting galaxies. As shown in § 6.2, we found some patterns of luminosity and spectral variations (Table 6.2; summary of § 6.2). We proceed to compare each state of the ULXs with those of Galactic BHBs.

6.3.1 To Compare with Previous Studies

For the *bright* state, especially for NGC 4490/85 ULX-8 and 6, we speculate that this state corresponds to the ApSS based on the following two reasons: (i) The two sources with the slim disk are the most likely interpretation (§ 6.2.1 and 6.2.4). (ii) The Eddington ratios (0.41–0.63 and 0.53–0.55) are similar to those of two Galactic BHBs considered to be in the ApSS: XTE J1550–564 ($\sim$0.4; Kubota & Makishima 2004[76]) and 4U 1630–47 (0.25–0.35; Abe et al. 2005[1]). However, the *bright* state of M 51 source-69 and NGC 4490/85 ULX-2 do not show such features of the ApSS. This fact suggests that the boundary luminosity to separate the *bright* and the *faint* states may be correct overall, but varies source to source.

Table 6.2: Summary of the representative models for all the ULXs

Name	Representative model [a]		
	bright	*faint*	*dim*
Source-69	any more model(s)	**PL** ($\Gamma < 1.5$)	unconstraint
Source-82	—	**PL** ($\Gamma = 1.8$–2.6)	—
ULX-2	any more model(s)	—	—
ULX-3	unconstraint	—	—
ULX-4	unconstraint	unconstraint	—
ULX-6	**Kawaguchi** ($33^{+2}_{-5}\ M_{\odot}$)	unconstraint	unconstraint
ULX-8	**Kawaguchi** ($37 \pm 2\ M_{\odot}$)	—	—

[a] The determinable model is shown in the bold font. The states not observed is expressed as "—".

For the *faint* state, the representative model is PL for sources which we can determine a model (M 51 source-82 and 69). The VHS and the LHS in Galactic BHBs have a PL shaped spectrum with the photon index Γ of $\sim$2.5 and 1.5–1.9, respectively. If the *bright* state of ULXs is the ApSS of Galactic BHBs, the *faint* state should correspond to the VHS, because the *faint* state is represented by the PL-like spectrum and the luminosity is only twice smaller than that of the *bright* state. However, our samples in the *faint* state show a wide PL index range of $\Gamma \sim 1.1$–2.6. In the next subsection, we discuss the *faint* state more in detail by using the *MAXI* results for Galactic BHBs (see § 5.2).

Finally, we briefly mention the *dim* state. We consider the *dim* state seen in some sources is distinctive from the *faint* state. This is because this state has lower luminosity and steeper spectral index, when fitted with PL, than the *faint* state. The photon statistics is too low to constrain the representative model, and their counterpart state in the Galactic BHBs is unknown.

6.3.2 To Compare with the Present *MAXI* Results

In order to search for a counterpart of the *faint* state of ULXs, we compare the present *MAXI* results for Galactic BHBs with two ULXs (M 51 source-82 and 69) in the *faint* state by using the relation between the Eddington ratio ($L_{\rm X,PL}/L_{\rm Edd}$) and the photon index. The masses of the BHBs and the ULXs are required to calculate the Eddington ratio. We adopt the central value of the mass for BHBs (Table 4.5). Exceptionally, we assume a typical

BH mass of 10 $M_\odot$ for three BHBs (4U 1630−47, H 1743−322, and Swift J1753.5−0127), because masses of these BHBs have not been known yet. On the other hand, for the two ULXs (source-82 and 69) in the *faint* state, we assume 40 $M_\odot$, adopting the estimated mass of the two ULXs, ULX-8 and 6, 30–40 $M_\odot$. Figure 6.5 shows the summarized plot of the relation of all the variable BHBs (refer to Figure 5.4 and Table 5.4) and the two *faint* state ULXs. We note that such BHB data are successfully fitted with a PL function with a null hypothesis probability of >5%.

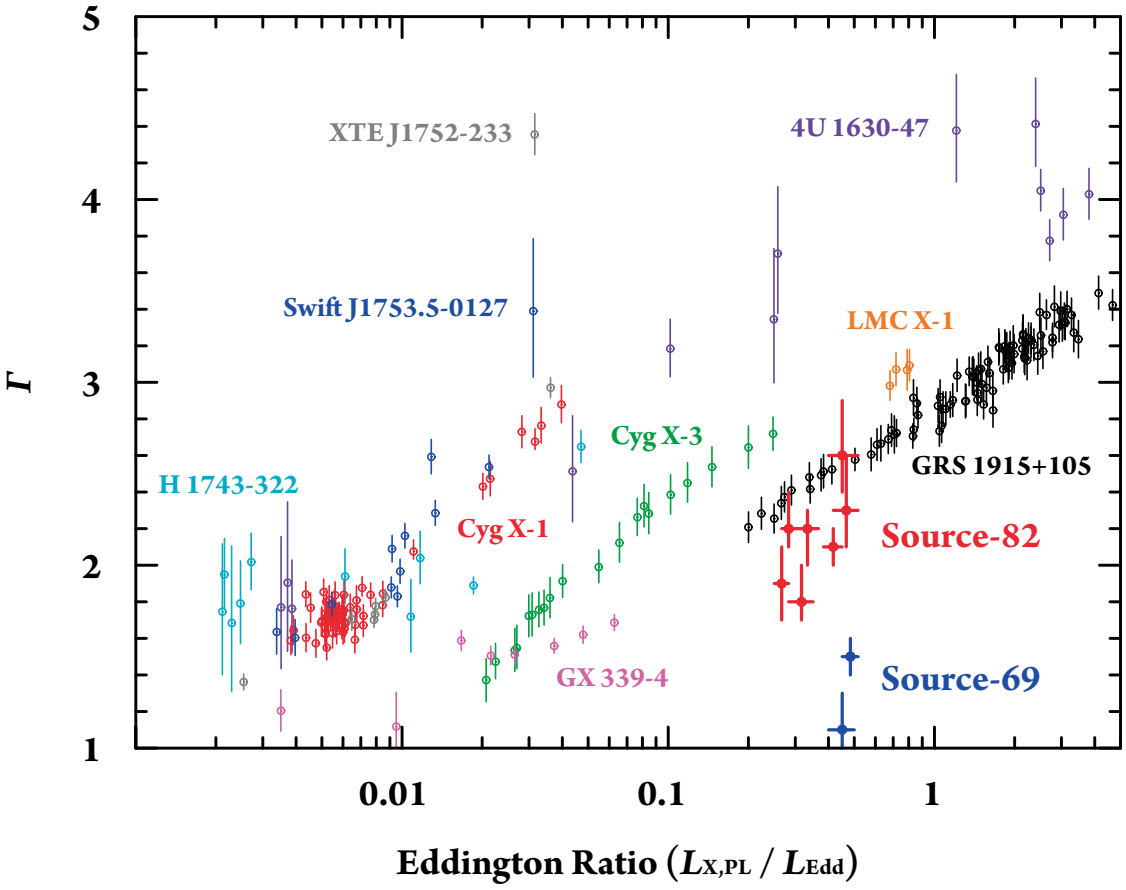

Figure 6.5: Photon index Γ against the Eddington ratio $L_{\rm X,PL}/L_{\rm Edd}$ for several Galactic BHBs (*thin*) and the two ULXs (*thick*).

We noticed that the data points of source-82 and those of the low luminosity part of GRS 1915+105 are located at similar positions. In order to test this similarity, we fitted these data points of each source with the PL ($\Gamma = n[L_{\rm X,PL}/L_{\rm Edd}]^b$), and compared their normalization n and power b. The derived parameters (90% uncertainties) are $n = 2.6^{+0.8}_{-0.6}$

and $b = 0.18 \pm 0.27$ for source-82, and $n = 2.81^{+0.02}_{-0.05}$ and $b = 0.13 \pm 0.01$ for GRS 1915+105, respectively. Since both parameters are consistent within the range of errors, we may consider that both sources are in the same spectral state. If so, at least the *faint* state of source-82 corresponds to the VHS, because GRS 1915+105 shows the photon index of ∼2.5 indicating the VHS. We note that GRS 1915+105 is known as an especially unique object among all the Galactic BHBs (e.g., Belloni et al. 2000[12]; Vierdayanti et al. 2010b[180]), and its BH is most massive in the Galaxy (10.0–18.0 $M_{\odot}$; Table 4.5). Spectral similarities between ULXs and GRS 1915+105 may be related to the massiveness of the central BHs.

Chapter 7

Conclusions

We have analyzed X-ray spectra (34 samples) of seven bright ULXs in the interacting galaxy systems M 51 and NGC 4490/85 using the archived data from multiple *Chandra* and *XMM-Newton* observations. We constructed a histogram of luminosities, in which we found a hint of three distinctive states: (i) The *bright* state with the brighter luminosity range (3–6$\times10^{39}$ ergs s^{-1}) for 20 samples, (ii) the *faint* state with the fainter luminosity range (1.5–3$\times10^{39}$ ergs s^{-1}) for 11 samples, and (iii) the *dim* state with luminosities below the fainter range ($<$1.2$\times10^{39}$ ergs s^{-1}) for three samples. On the whole, the spectra in the *bright* state are represented by the MCD model (standard disk) or the Kawaguchi model (slim disk), while those in the *faint* state are represented by the PL model. We classified the flux changes of all sources into the intra-state variation and the inter-state transition. Four ULXs (M 51 source-82, NGC 4490/85 ULX-2, 3, and 8) exhibited the former, while the remaining three (M 51 source-69, NGC 4490/85 ULX-4, and 6) exhibited the latter.

All the spectra of two ULXs (NGC 4490/85 ULX-8 and 6) in the *bright* state can be reproduced by a slim disk model by Kawaguchi (2003)[71] with a constant BH mass of 37 ± 2 and 33^{+2}_{-5} $M_{\odot}$, respectively. In particular, for ULX-8, a common BH mass was not found with the MCD model fitting. This suggests that the slim disk model is a more appropriate explanation at least in some cases of the "*bright*" state, in which ULXs harbor BHs of a mass of $<$40 $M_{\odot}$.

From the results of spectral fitting, we compared each state of the ULXs with those of Galactic BHBs. We propose that the *bright* state of two ULXs (NGC 4490/85 ULX-8 and 6) corresponds to the ApSS of Galactic BHBs. For the *faint* state, the representative model

is PL. It is different in the range of photon index from the general VHS of Galactic BHBs, which also shows a PL spectrum. However, when we assume that the mass of all the ULXs are similar, the *faint* state of a ULX (M 51 source-82) at least corresponds to the VHS of the Galactic BHB GRS 1915+105 from the present *MAXI* results. The nature of the *dim* state is unconstrained, but has the most steep spectrum.

Appendix A

Simulation for the Fraction of Successful fits

In this appendix, we explain the detailed simulation about Figure 6.1 (b) in § 6.1. We simulated many spectra composed both of the PL and MCD models with different brightness, and fitted them with a single model (the PL or MCD model) to test whether MCD is favored for bright sources. We did not find the evidence that the MCD model is more favored at higher luminosities. In fact, it is the opposite; MCD is disfavored for bright sources. This indicates that our trend to have more successful MCD fits has a physical origin, and not a statistical artifact.

The detailed procedure is as follows. First, we generated an assemble of simulated spectra that contain both the MCD and PL components. For the spectral parameters, we used different combinations for all spectra; the absorption in `wabs` (0.05–0.5$\times 10^{22}$ cm^{-2}), the photon index in PL (1.5–2.5), the innermost disk temperature in MCD (1.0–2.0 keV), the total photon counts (200–2000 counts), and the ratio of PL to the total photon counts (0.0–1.0). The total number of the simulated spectra is about 15,000.

For each one of the simulated spectrum, we fitted either with the PL or MCD model, as we actually did for our observed spectra. The attached Figures A.1, A.2 (a), and A.2 (b) show the fraction of successful (i.e., the null hypothesis probability >5%) fits as a function of counts. Each figure respectively indicates the case of all spectra, the ratio of PL to the total photon counts of 0.2, or 0.8.

Two results were obtained: (i) For small counts, both models can fit the spectra. (ii) For large counts, the PL model explains the spectra of mixed components better than the MCD model (Figure A.1).

These are the trends for the number of counts. We consider that the trend is valid for the luminosity, as the distance to the two systems (M 51 and NGC 4490/85) is almost the same.

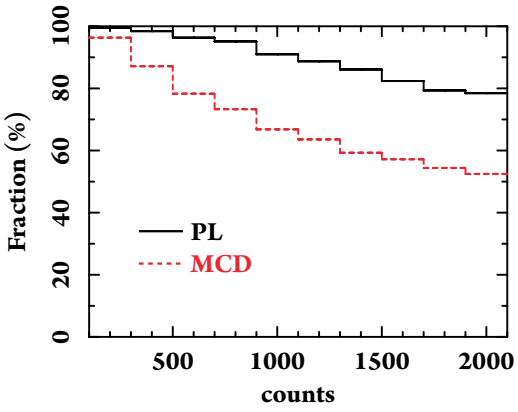

Figure A.1: Fraction of successful fits as a function of counts, indicating the case of all spectra. As well as Figure 6.1 (b), the black solid and red dashed lines indicate the PL and MCD, respectively.

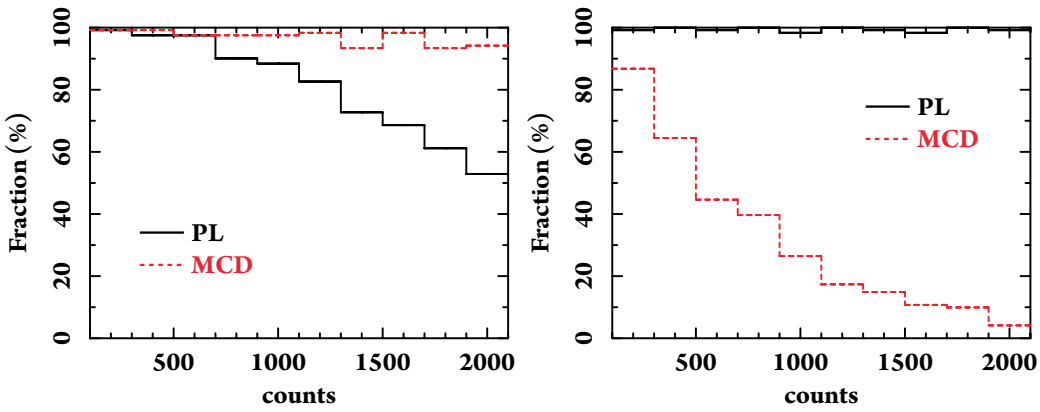

Figure A.2: Same with Figure A.1, but the case of the ratio of PL to the total photon counts of (a) 0.2 and (b) 0.8.

Bibliography

[1] Abe, Y., Fukazawa, Y., Kubota, A., Kasama, D., & Makishima, K. 2005, *Publication of Astronomical Society of Japan*, 57, 629

[2] Abramowicz, M. A., Xu, C., & Lasota, J. P. 1986, Quasars, 119, 371

[3] Abramowicz, M. A., Czerny, B., Lasota, J. P., & Szuszkiewicz, E. 1988, *Astrophysical Journal*, 332, 646

[4] Abramowicz, M. A., Chen, X., Kato, S., Lasota, J.-P., & Regev, O. 1995, *Astrophysical Journal Letter*, 438, L37

[5] Anders, E., & Ebihara, M. 1982, *Geochimica et Cosmochimica Acta*, 46, 2363

[6] Aschenbach, B. 1985, Reports on Progress in Physics, 48, 579

[7] Augusteijn, T., Kuulkers, E., & van Kerkwijk, M. H. 2001, *Astronomy & Astrophysics*, 375, 447

[8] Barret, D., Motch, C., Pietsch, W., & Voges, W. 1995, *Astronomy & Astrophysics*, 296, 459

[9] Barthelmy, S. D., et al. 2005, *Space Science Review*, 120, 143

[10] Begelman, M. C., & Meier, D. L. 1982, *Astrophysical Journal*, 253, 873

[11] Belczynski, K., Bulik, T., Fryer, C. L., Ruiter, A., Valsecchi, F., Vink, J. S., & Hurley, J. R. 2010, *Astrophysical Journal*, 714, 1217

[12] Belloni, T., Klein-Wolt, M., Méndez, M., van der Klis, M., & van Paradijs, J. 2000, *Astronomy & Astrophysics*, 355, 271

[13] Berghea, C. T., Weaver, K. A., Colbert, E. J. M., & Roberts, T. P. 2008, *Astrophysical Journal*, 687, 471

[14] Blundell, K. M., & Bowler, M. G. 2004, *Astrophysical Journal Letter*, 616, L159

[15] Bradley, C. K., Hynes, R. I., Kong, A. K. H., Haswell, C. A., Casares, J., & Gallo, E. 2007, *Astrophysical Journal*, 667, 427

[16] Brassington, N. J., Ponman, T. J., & Read, A. M. 2007, *Monthly Notices of the Royal Astronomical Society*, 377, 1439

[17] Broos, P. S., Townsley, L. K., Getman, K., & Bauer, F. E. 2002, ACIS Extract, An ACIS Point Source Extraction Package (University Park: Pennsylvania State Univ.)

[18] Caballero-García, M. D., Miller, J. M., Trigo, M. D., Kuulkers, E., Fabian, A. C., Mas-Hesse, J. M., Steeghs, D., & van der Klis, M. 2009, *Astrophysical Journal*, 692, 1339

[19] Campana, S., Stella, L., Belloni, T., Israel, G. L., Santangelo, A., Frontera, F., Orlandini, M., & Dal Fiume, D. 2002, *Astronomy & Astrophysics*, 384, 163

[20] Casares, J., Zurita, C., Shahbaz, T., Charles, P. A., & Fender, R. P. 2004, *Astrophysical Journal Letter*, 613, L133

[21] *Chandra* IPI Teams 2009, The *Chandra* Proposers' Observatory Guide, ver. 12.0, MSFC, NASA

[22] Clemens, M. S., Alexander, P., & Green, D. A. 1998, *Monthly Notices of the Royal Astronomical Society*, 297, 1015

[23] Clemens, M. S., Alexander, P., & Green, D. A. 1999, *Monthly Notices of the Royal Astronomical Society*, 307, 481

[24] Clemens, M. S., & Alexander, P. 2002, *Monthly Notices of the Royal Astronomical Society*, 333, 39

[25] Davis, S. W., Done, C., & Blaes, O. M. 2006, *Astrophysical Journal*, 647, 525

[26] de Vaucouleurs, G., de Vaucouleurs, A., & Corwin, J. R. 1976, Second Reference Catalogue of Bright Galaxies (Austin: Univ. Texas Press)

[27] de Vaucouleurs, G., de Vaucouleurs, A., Corwin, H. G., Jr., Buta, R. J., Paturel, G., & Fouque, P. 1991, Third Reference Catalogue of Bright Galaxies (New York: Springer)

[28] Dewangan, G. C., Griffiths, R. E., Choudhury, M., Miyaji, T., & Schurch, N. J. 2005, *Astrophysical Journal*, 635, 198

[29] di Benedetto, G. P. 1997, *Astrophysical Journal*, 486, 60

[30] Dickey, J. M., & Lockman, F. J. 1990, *Annual Review of Astronomy & Astrophysics*, 28, 215

[31] Done, C., Gierliński, M., & Kubota, A. 2007, *Astronomy & Astrophysics Review*, 15, 1

[32] Dubus, G., Kim, R. S. J., Menou, K., Szkody, P., & Bowen, D. V. 2001, *Astrophysical Journal*, 553, 307

[33] Dunn, R. J. H., Fender, R. P., Körding, E. G., Belloni, T., & Cabanac, C. 2010, *Monthly Notices of the Royal Astronomical Society*, 403, 61

[34] Ebisawa, K., Makino, F., Mitsuda, K., Belloni, T., Cowley, A. P., Schmidtke, P. C., & Treves, A. 1993, *Astrophysical Journal*, 403, 684

[35] Ebisawa, K., et al. 1994, *Publication of Astronomical Society of Japan*, 46, 375

[36] Ebisawa, K., Życki, P., Kubota, A., Mizuno, T., & Watarai, K. 2003, *Astrophysical Journal*, 597, 780

[37] Ehle, M., Pietsch, W., & Beck, R. 1995, *Astronomy & Astrophysics*, 295, 289

[38] Esin, A. A., McClintock, J. E., & Narayan, R. 1997, *Astrophysical Journal*, 489, 865

[39] Fabbiano, G. 2006, *Annual Review of Astronomy & Astrophysics*, 44, 323

[40] Feldmeier, J. J., Ciardullo, R., & Jacoby, G. H. 1997, *Astrophysical Journal*, 479, 231

[41] Fender, R. P., Garrington, S. T., McKay, D. J., Muxlow, T. W. B., Pooley, G. G., Spencer, R. E., Stirling, A. M., & Waltman, E. B. 1999, *Monthly Notices of the Royal Astronomical Society*, 304, 865

[42] Feng, H., & Kaaret, P. 2006, *Astrophysical Journal Letter*, 650, L75

[43] Feng, H., & Kaaret, P. 2010, *Astrophysical Journal Letter*, 712, L169

[44] Filippova, E., Revnivtsev, M., Fabrika, S., Postnov, K., & Seifina, E. 2006, *Astronomy & Astrophysics*, 460, 125

[45] Foschini, L., et al. 2006, Advances in Space Research, 38, 1378

[46] Frank, J., King, A., & Raine, D. J. 2002, Accretion Power in Astrophysics: Third Edition (Cambridge: Cambridge Univ. Press)

[47] Fridriksson, J. K., Homan, J., Lewin, W. H. G., Kong, A. K. H., & Pooley, D. 2008, *Astrophysical Journal Supplement*, 177, 465

[48] Fukazawa, Y., Iyomoto, N., Kubota, A., Matsumoto, Y., & Makishima, K. 2001, *Astronomy & Astrophysics*, 374, 73

[49] Fukue, J., Mineshige, S., & Kato, S. 2008, Black-Hole Accretion Disks (Kyoto: Kyoto Univ. Press)

[50] Gallo, E., Fender, R. P., & Pooley, G. G. 2003, *Monthly Notices of the Royal Astronomical Society*, 344, 60

[51] Garmire, G. P., Bautz, M. W., Ford, P. G., Nousek, J. A., & Ricker, G. R., Jr. 2003, Proceeding of SPIE, 4851, 28

[52] Gelino, D. M., & Harrison, T. E. 2003, *Astrophysical Journal*, 599, 1254

[53] Gierliński, M., Zdziarski, A. A., Poutanen, J., Coppi, P. S., Ebisawa, K., & Johnson, W. N. 1999, *Monthly Notices of the Royal Astronomical Society*, 309, 496

[54] Gierliński, M., & Done, C. 2004, *Monthly Notices of the Royal Astronomical Society*, 347, 885

[55] Gladstone, J. C., & Roberts, T. P. 2009, *Monthly Notices of the Royal Astronomical Society*, 397, 124

[56] Gladstone, J. C., Roberts, T. P., & Done, C. 2009, *Monthly Notices of the Royal Astronomical Society*, 397, 1836

[57] Goad, M. R., Roberts, T. P., Reeves, J. N., & Uttley, P. 2006, *Monthly Notices of the Royal Astronomical Society*, 365, 191

[58] Godet, O., Barret, D., Webb, N. A., Farrell, S. A., & Gehrels, N. 2009, *Astrophysical Journal Letter*, 705, L109

[59] Hanke, M., Wilms, J., Nowak, M. A., Barragán, L., & Schulz, N. S. 2010, *Astronomy & Astrophysics*, 509, L8

[60] Harlaftis, E. T., Horne, K., & Filippenko, A. V. 1996, *Publication of Astronomical Society of Pacific*, 108, 762

[61] Hiemstra, B., Soleri, P., Méndez, M., Belloni, T., Mostafa, R., & Wijnands, R. 2009, *Monthly Notices of the Royal Astronomical Society*, 394, 2080

[62] Hjellming, R. M., & Rupen, M. P. 1995, *Nature*, 375, 464

[63] Homan, J., Wijnands, R., Kong, A., Miller, J. M., Rossi, S., Belloni, T., & Lewin, W. H. G. 2006, *Monthly Notices of the Royal Astronomical Society*, 366, 235

[64] Hynes, R. I., Haswell, C. A., Chaty, S., Shrader, C. R., & Cui, W. 2002, *Monthly Notices of the Royal Astronomical Society*, 331, 169

[65] Ichimaru, S. 1977, *Astrophysical Journal*, 214, 840

[66] Isobe, N., et al. 2009, *Publication of Astronomical Society of Japan*, 61, 279

[67] Kaaret, P., Prestwich, A. H., Zezas, A., Murray, S. S., Kim, D.-W., Kilgard, R. E., Schlegel, E. M., & Ward, M. J. 2001, *Monthly Notices of the Royal Astronomical Society*, 321, L29

[68] Kaaret, P., Ward, M. J., & Zezas, A. 2004, *Monthly Notices of the Royal Astronomical Society*, 351, L83

[69] Kaaret, P., Corbel, S., Tomsick, J. A., Lazendic, J., Tzioumis, A. K., Butt, Y., & Wijnands, R. 2006, *Astrophysical Journal*, 641, 410

[70] Katz, J. I. 1977, *Astrophysical Journal*, 215, 265

[71] Kawaguchi, T. 2003, *Astrophysical Journal*, 593, 6

[72] Kawashima, T., Ohsuga, K., Mineshige, S., Heinzeller, D., Takabe, H., & Matsumoto, R. 2009, *Publication of Astronomical Society of Japan*, 61, 769

[73] King, A. R., Davies, M. B., Ward, M. J., Fabbiano, G., & Elvis, M. 2001, *Astrophysical Journal Letter*, 552, L109

[74] Kubota, A., Tanaka, Y., Makishima, K., Ueda, Y., Dotani, T., Inoue, H., & Yamaoka, K. 1998, *Publication of Astronomical Society of Japan*, 50, 667

[75] Kubota, A., Mizuno, T., Makishima, K., Fukazawa, Y., Kotoku, J., Ohnishi, T., & Tashiro, M. 2001, *Astrophysical Journal Letter*, 547, L119

[76] Kubota, A., & Makishima, K. 2004, *Astrophysical Journal*, 601, 428

[77] Kubota, K., Ueda, Y., Fabrika, S., Medvedev, A., Barsukova, E. A., Sholukhova, O., & Goranskij, V. P. 2010, *Astrophysical Journal*, 709, 1374

[78] Kuno, N., & Nakai, N. 1997, *Publication of Astronomical Society of Japan*, 49, 279

[79] Jansen, F., et al. 2001, *Astronomy & Astrophysics*, 365, L1

[80] La Parola, V., Peres, G., Fabbiano, G., Kim, D. W., & Bocchino, F. 2001, *Astrophysical Journal*, 556, 47

[81] Ling, J. C., & Wheaton, W. A. 2005, *Astrophysical Journal*, 622, 492

[82] Liu, J.-F., Bregman, J. N., Irwin, J., & Seitzer, P. 2002, *Astrophysical Journal Letter*, 581, L93

[83] Liu, J.-F., & Bregman, J. N. 2005, *Astrophysical Journal Supplement*, 157, 59

[84] Liu, J. 2008, arXiv:0811.0804

[85] Long, K. S. & van Speybroeck, L. P. 1983, Accretion-Driven Stellar X-ray Sources (Cambridge: Cambridge Univ. Press)

[86] Lynden-Bell, D. 1969, *Nature*, 223, 690

[87] Lynden-Bell, D., & Pringle, J. E. 1974, *Monthly Notices of the Royal Astronomical Society*, 168, 603

[88] Maccarone, T. J. 2003, *Astronomy & Astrophysics*, 409, 697

[89] Makishima, K., Maejima, Y., Mitsuda, K., Bradt, H. V., Remillard, R. A., Tuohy, I. R., Hoshi, R., & Nakagawa, M. 1986, *Astrophysical Journal*, 308, 635

[90] Makishima, K., et al. 2000, *Astrophysical Journal*, 535, 632

[91] Makishima, K., et al. 2008, *Publication of Astronomical Society of Japan*, 60, 585

[92] Markert, T. H., Canizares, C. R., Clark, G. W., Lewin, W. H. G., Schnopper, H. W., & Sprott, G. F. 1973, *Astrophysical Journal Letter*, 184, L67

[93] Markwardt, C. B., Barthelmy, S. D., Evans, P. A., Swank, J. H. 2009, ATel, 2261

[94] Margon, B., Bowyer, S., & Stone, R. P. S. 1973, *Astrophysical Journal Letter*, 185, L113

[95] Marston, A. P., Elmegreen, D., Elmegreen, B., Forman, W., Jones, C., & Flanagan, K. 1995, *Astrophysical Journal*, 438, 663

[96] Masetti, N., Bianchini, A., Bonibaker, J., della Valle, M., & Vio, R. 1996, *Astronomy & Astrophysics*, 314, 123

[97] Matsumoto, H., Tsuru, T. G., Koyama, K., Awaki, H., Canizares, C. R., Kawai, N., Matsushita, S., & Kawabe, R. 2001, *Astrophysical Journal Letter*, 547, L25

[98] Matsuoka, M., et al. 1999, *Astronomische Nachrichten*, 320, 275

[99] Matsuoka, M., et al. 2009, *Publication of Astronomical Society of Japan*, 61, 999

[100] Matsuoka, M., et al. 2010, American Institute of Physics Conference Series, 1248, 531

[101] Mazzali, P. A., Röpke, F. K., Benetti, S., & Hillebrandt, W. 2007, *Science*, 315, 825

[102] McClintock, J. E., Garcia, M. R., Caldwell, N., Falco, E. E., Garnavich, P. M., & Zhao, P. 2001, *Astrophysical Journal Letter*, 551, L147

[103] McClintock, J. E., & Remillard, R. A. 2006, Compact Stellar X-ray Sources (Cambridge: Cambridge Univ. Press)

[104] McClintock, J. E., Narayan, R., & Shafee, R. 2007, Black Holes (Cambridge: Cambridge Univ. Press), arXiv:0707.4492

[105] Miller, M. C., & Colbert, E. J. M. 2004, International Journal of Modern Physics D, 13, 1

[106] Miller-Jones, J. C. A., Jonker, P. G., Dhawan, V., Brisken, W., Rupen, M. P., Nelemans, G., & Gallo, E. 2009, *Astrophysical Journal Letter*, 706, L230

[107] Mitsuda, K., et al. 1984, *Publication of Astronomical Society of Japan*, 36, 741

[108] Miyamoto, S., Kimura, K., Kitamoto, S., Dotani, T., & Ebisawa, K. 1991, *Astrophysical Journal*, 383, 784

[109] Miyamoto, S., Iga, S., Kitamoto, S., & Kamado, Y. 1993, *Astrophysical Journal Letter*, 403, L39

[110] Miyawaki, R., Makishima, K., Yamada, S., Gandhi, P., Mizuno, T., Kubota, A., Tsuru, T. G., & Matsumoto, H. 2009, *Publication of Astronomical Society of Japan*, 61, 263

[111] Mizuno, T., Kubota, A., & Makishima, K. 2001, *Astrophysical Journal*, 554, 1282

[112] Mizuno, T., et al. 2007, *Publication of Astronomical Society of Japan*, 59, 257

[113] Morrison, R., & McCammon, D. 1983, *Astrophysical Journal*, 270, 119

[114] Muñoz-Darias, T., Motta, S., Pawar, D., Belloni, T. M., Campana, S., & Bhattacharya, D. 2010, *Monthly Notices of the Royal Astronomical Society*, 404, L94

[115] Nakahira, S., et al. 2010, arXiv:1007.0801

[116] Narayan, R., & Yi, I. 1994, *Astrophysical Journal Letter*, 428, L13

[117] Mineshige, S., Kawaguchi, T., Takeuchi, M., & Hayashida, K. 2000, *Publication of Astronomical Society of Japan*, 52, 499

[118] Nowak, M. A., Juett, A., Homan, J., Yao, Y., Wilms, J., Schulz, N. S., & Canizares, C. R. 2008, *Astrophysical Journal*, 689, 1199

[119] Oda, M., Gorenstein, P., Gursky, H., Kellogg, E., Schreier, E., Tananbaum, H., & Giacconi, R. 1971, *Astrophysical Journal Letter*, 166, L1

[120] Ohsuga, K., Mori, M., Nakamoto, T., & Mineshige, S. 2005, *Astrophysical Journal*, 628, 368

[121] Okajima, T., Ebisawa, K., & Kawaguchi, T. 2006, *Astrophysical Journal Letter*, 652, L105

[122] Orosz, J. A., Bailyn, C. D., McClintock, J. E., & Remillard, R. A. 1996, *Astrophysical Journal*, 468, 380

[123] Orosz, J. A., Jain, R. K., Bailyn, C. D., McClintock, J. E., & Remillard, R. A. 1998, *Astrophysical Journal*, 499, 375

[124] Orosz, J. A., et al. 2001, *Astrophysical Journal*, 555, 489

[125] Orosz, J. A., et al. 2002, *Astrophysical Journal*, 568, 845

[126] Page, M. J., Soria, R., Wu, K., Mason, K. O., Cordova, F. A., & Priedhorsky, W. C. 2003, *Monthly Notices of the Royal Astronomical Society*, 345, 639

[127] Palumbo, G. G. C., Fabbiano, G., Trinchieri, G., & Fransson, C. 1985, *Astrophysical Journal*, 298, 259

[128] Parmar, A. N., Kuulkers, E., Oosterbroek, T., Barr, P., Much, R., Orr, A., Williams, O. R., & Winkler, C. 2003, *Astronomy & Astrophysics*, 411, L421

[129] Predehl, P., Burwitz, V., Paerels, F., & Trümper, J. 2000, *Astronomy & Astrophysics*, 357, L25

[130] Prestwich, A. H., et al. 2007, *Astrophysical Journal Letter*, 669, L21

[131] Pringle, J. E. 1981, *Annual Review of Astronomy & Astrophysics*, 19, 137

[132] Ptak, A., Serlemitsos, P., Yaqoob, T., & Mushotzky, R. 1999, *Astrophysical Journal Supplement*, 120, 179

[133] Ptak, A., & Griffiths, R. 1999, *Astrophysical Journal Letter*, 517, L85

[134] Read, A. M., Ponman, T. J., & Strickland, D. K. 1997, *Monthly Notices of the Royal Astronomical Society*, 286, 626

[135] Remillard, R. A., & McClintock, J. E. 2006, *Annual Review of Astronomy & Astrophysics*, 44, 49

[136] Rhoades, C. E., & Ruffini, R. 1974, *Physical Review Letters*, 32, 324

[137] Roberts, T. P., & Warwick, R. S. 2000, *Monthly Notices of the Royal Astronomical Society*, 315, 98

[138] Roberts, T. P., Warwick, R. S., Ward, M. J., & Murray, S. S. 2002, *Monthly Notices of the Royal Astronomical Society*, 337, 677

[139] Roberts, T. P., Kilgard, R. E., Warwick, R. S., Goad, M. R., & Ward, M. J. 2006, *Monthly Notices of the Royal Astronomical Society*, 371, 1877

[140] Roberts, T. P. 2007, *Astrophysics & Space Science*, 311, 203

[141] Russell, D. M., Lewis, F., Roche, P., Clark, J. S., Breedt, E., & Fender, R. P. 2010, *Monthly Notices of the Royal Astronomical Society*, 402, 2671

[142] Sanford, P., Mason, K. O., & Ives, J. 1975, *Monthly Notices of the Royal Astronomical Society*, 173, 9P

[143] Schweizer, F. 1977, *Astrophysical Journal*, 211, 324

[144] Scargle, J. D. 1998, *Astrophysical Journal*, 504, 405

[145] Scoville, N. Z., Polletta, M., Ewald, S., Stolovy, S. R., Thompson, R., & Rieke, M. 2001, *Astronomical Journal*, 122, 3017

[146] Shahbaz, T., Naylor, T., & Charles, P. A. 1994, *Monthly Notices of the Royal Astronomical Society*, 268, 756

[147] Shakura, N. I., & Sunyaev, R. A. 1973, *Astronomy & Astrophysics*, 24, 337

[148] Shimura, T., & Takahara, F. 1995, *Astrophysical Journal*, 445, 780

[149] Shrader, C. R., Wagner, R. M., Charles, P. A., Harlaftis, E. T., & Naylor, T. 1997, *Astrophysical Journal*, 487, 858

[150] Shrader, C. R., Titarchuk, L., & Shaposhnikov, N. 2010, *Astrophysical Journal*, 718, 488

[151] Silverman, J. M., & Filippenko, A. V. 2008, *Astrophysical Journal Letter*, 678, L17

[152] Soleri, P., et al. 2010, *Monthly Notices of the Royal Astronomical Society*, 406, 1471

[153] Soria, R., Motch, C., Read, A. M., & Stevens, I. R. 2004, *Astronomy & Astrophysics*, 423, 955

[154] Soria, R., Risaliti, G., Elvis, M., Fabbiano, G., Bianchi, S., & Kuncic, Z. 2009, *Astrophysical Journal*, 695, 1614

[155] Stauberts, R. 2008, The Universe in X-rays (New York: Springer)

[156] Strüder, L., et al. 2001, *Astronomy & Astrophysics*, 365, L18

[157] Swartz, D. A., Ghosh, K. K., Tennant, A. F., & Wu, K. 2004, *Astrophysical Journal Supplement*, 154, 519

[158] Szostek, A., Zdziarski, A. A., & McCollough, M. L. 2008, *Monthly Notices of the Royal Astronomical Society*, 388, 1001

[159] Tanaka, Y., & Shibazaki, N. 1996, *Annual Review of Astronomy & Astrophysics*, 34, 607

[160] Tananbaum, H., Gursky, H., Kellogg, E., Giacconi, R., & Jones, C. 1972, *Astrophysical Journal Letter*, 177, L5

[161] Terada, K., Kitamoto, S., Negoro, H., & Iga, S. 2002, *Publication of Astronomical Society of Japan*, 54, 609

[162] Terashima, Y., Ptak, A., Fujimoto, R., Itoh, M., Kunieda, H., Makishima, K., & Serlemitsos, P. J. 1998, *Astrophysical Journal*, 496, 210

[163] Terashima, Y., & Wilson, A. S. 2004, *Astrophysical Journal*, 601, 735

[164] Terashima, Y., Inoue, H., & Wilson, A. S. 2006, *Astrophysical Journal*, 645, 264

[165] The MIT/GSFC ASM Team, Bradt, H., Morgan, E. H., & Remillard, R. 2006, Advances in Space Research, 38, 2970

[166] Tomsick, J. A., Corbel, S., & Kaaret, P. 2001, *Astrophysical Journal*, 563, 229

[167] Tomsick, J. A., Kalemci, E., & Kaaret, P. 2004, *Astrophysical Journal*, 601, 439

[168] Tsuchiya , Y., et al. 2005, procspie, 5898, 403

[169] Tsunoda, N., Kubota, A., Namiki, M., Sugiho, M., Kawabata, K., & Makishima, K. 2006, *Publication of Astronomical Society of Japan*, 58, 1081

[170] Tueller, J., et al. 2010, *Astrophysical Journal Supplement*, 186, 378

[171] Turner, M. J. L., et al. 2001, *Astronomy & Astrophysics*, 365, L27

[172] Ueda, Y., Inoue, H., Tanaka, Y., Ebisawa, K., Nagase, F., Kotani, T., & Gehrels, N. 1998, *Astrophysical Journal*, 500, 1069

[173] Ueno, S., et al. 2009, Proceedings of Science, 011, The Extreme Sky: Sampling the Universe above 10 keV

[174] van der Hulst, J. M., Kennicutt, R. C., Crane, P. C., & Rots, A. H. 1988, *Astronomy & Astrophysics*, 195, 38

[175] Van Paradijs, J. & Verbunt, F. 1984, in AIP Conf. Proc. 115, High Energy Transient Astrophysics, ed S Woosley (New York: AIP)

[176] Vázquez, G. A., Hornschemeier, A. E., Colbert, E., Roberts, T. P., Ward, M. J., & Malhotra, S. 2007, *Astrophysical Journal Letter*, 658, L21

[177] Viallefond, F., Allen, R. J., & de Boer, J. A. 1980, *Astronomy & Astrophysics*, 82, 207

[178] Vierdayanti, K., Mineshige, S., Ebisawa, K., & Kawaguchi, T. 2006, *Publication of Astronomical Society of Japan*, 58, 915

[179] Vierdayanti, K.,Done, C., Roberts, T. P., & Mineshige, S. 2010, *Monthly Notices of the Royal Astronomical Society*, 403, 1206

[180] Vierdayanti, K., Mineshige, S., & Ueda, Y. 2010, *Publication of Astronomical Society of Japan*, 62, 239

[181] Vilhu, O., et al. 2003, *Astronomy & Astrophysics*, 411, L405

[182] Wachter, S., & Smale, A. P. 1998, *Astrophysical Journal Letter*, 496, L21

[183] Watarai, K.-y., & Fukue, J. 1999, *Publication of Astronomical Society of Japan*, 51, 725

[184] Watarai, K., Fukue, J., Takeuchi, M., & Mineshige, S. 2000, *Publication of Astronomical Society of Japan*, 52, 133

[185] Watarai, K., Mizuno, T., & Mineshige, S. 2001, *Astrophysical Journal Letter*, 549, L77

[186] Weisskopf, M. C., Brinkman, B., Canizares, C., Garmire, G., Murray, S., & Van Speybroeck, L. P. 2002, *Publication of Astronomical Society of Pacific*, 114, 1

[187] Winter, L. M., Mushotzky, R. F., & Reynolds, C. S. 2006, *Astrophysical Journal*, 649, 730

[188] *XMM-Newton* Community Support Team 2010, *XMM-Newton* Users Handbook, Issue 2.8, SOC, ESA

[189] Xue, Y., Wu, X.-B., & Cui, W. 2008, *Monthly Notices of the Royal Astronomical Society*, 384, 440

[190] Yoshida, T., Ebisawa, K., Matsushita, K., Tsujimoto, M., & Kawaguchi, T. 2010, *Astrophysical Journal*, 722, 760

[191] Yuan, F., Quataert, E., & Narayan, R. 2003, *Astrophysical Journal*, 598, 301

[192] Zdziarski, A. A., & Gierliński, M. 2004, Progress of Theoretical Physics Supplement, 155, 99

[193] Zdziarski, A. A., Gierliński, M., Mikołajewska, J., Wardziński, G., Smith, D. M., Harmon, B. A., & Kitamoto, S. 2004, *Monthly Notices of the Royal Astronomical Society*, 351, 791

[194] Zezas, A., Fabbiano, G., Baldi, A., Schweizer, F., King, A. R., Ponman, T. J., & Rots, A. H. 2006, *Astrophysical Journal Supplement*, 166, 211

[195] Ziółkowski, J. 2003, *Chinese Journal of Astronomy and Astrophysics Supplement*, 3, 245

[196] Zurita, C., Durant, M., Torres, M. A. P., Shahbaz, T., Casares, J., & Steeghs, D. 2008, *Astrophysical Journal*, 681, 1458

Acknowledgments

This Ph.D thesis was completed by supports from many people. First of all, I am deeply thankful to Associate Professor Kyoko Matsushita, who guided and taught me the basic astrophysics throughout the five years of my graduate life. I am also grateful to Professor Ken Ebisawa, who hosted me at ISAS and gave many advice about Galactic BHBs and ULXs. I am very fortunate to have opportunities to work in their laboratories.

I especially wish to express gratitude and respect to Masahiro Tsujimoto. He gave me many knowledge including the basic astronomy and astrophysics, space-based and ground-based observatories, how to think logically, how to write science articles and proposals, how to analyze science data, how to talk in conferences, how to clean my personal space, how to make Japanese and Chinese tea, etc. Moreover, he always gave valuable advice and discussions, and helped me to improve the manuscript. Without a lot of supports of him, I could not have completed this thesis.

I am obliged to Toshihiro Kawaguchi for giving theoretical advice and encouragement in writing this thesis. The theme of this thesis was motivated by the Kawaguchi model that he proposed for ULX X-ray spectral modeling.

I appreciate all the members, past and present, of the Matsushita laboratory and the ISAS X-ray group. I particularly thank R. Nagino, Y. Morikawa, R. Baba, T. Miyakawa, K. Morihana, K. Saitou, T. Fujinaga, K. Shimizu, and N. Iso for happy research days.

Kensuke Suzuki, who is one of my friends in the undergraduate era, taught me attractive points of ISAS and introduced to Professor Ken Ebisawa been registered at ISAS. I do not know the right words to properly thank him. I shall never forget his kindness.

Finally, I would like to express my special acknowledgment to my parents and brother for their support and understanding of my dream. I owe my life to them.

The public data and softwares of *Chandra* and *XMM-Newton* were obtained from the High Energy Astrophysics Science Archive Research Center (HEASARC) provided by NASA's Goddard Space Flight Center. Regarding *MAXI*, the *MAXI* team allowed me to use non-public data and software. I am grateful to the *MAXI* team for their kindness and work in the operation and monitoring the satellite.

Funding for the SDSS and SDSS-II has been provided by the Alfred P. Sloan Foundation, the Participating Institutions, the National Science Foundation, the U.S. Department of Energy, the National Aeronautics and Space Administration, the Ministry of Education, Culture, Sports, Science, and Technology of Japan, the Max Planck Society, and the Higher Education Funding Council for England. The SDSS Web Site is http://www.sdss.org/. SDSS images used in this thesis was produced with Montage, an image mosaic service supported by the NASA Earth Sciences Technology Office Computing Technologies program.

I am supported by the Japan Society for the Promotion of Science Research Fellowship for Young Scientists.